Sacral Anchoring of the LUMiC Prosthesis

Development of a protocol to in vitro evaluate newly designed 3D printed patient specific prosthesis for the sacrum after tumour resection

L. van Rijn

Master thesis

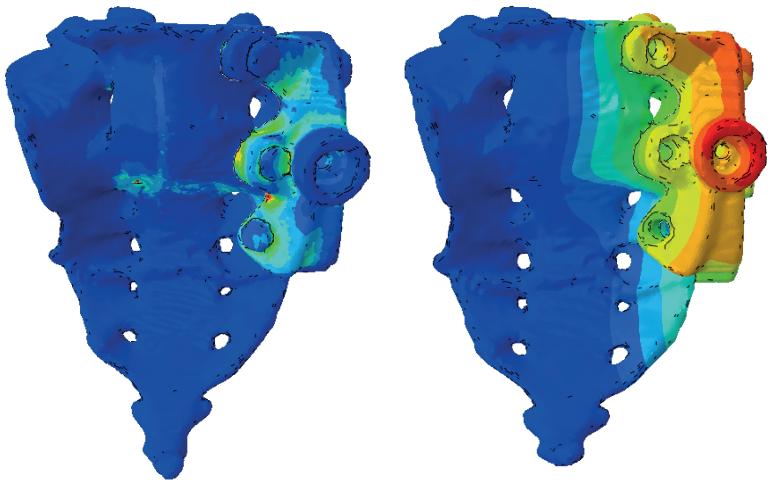

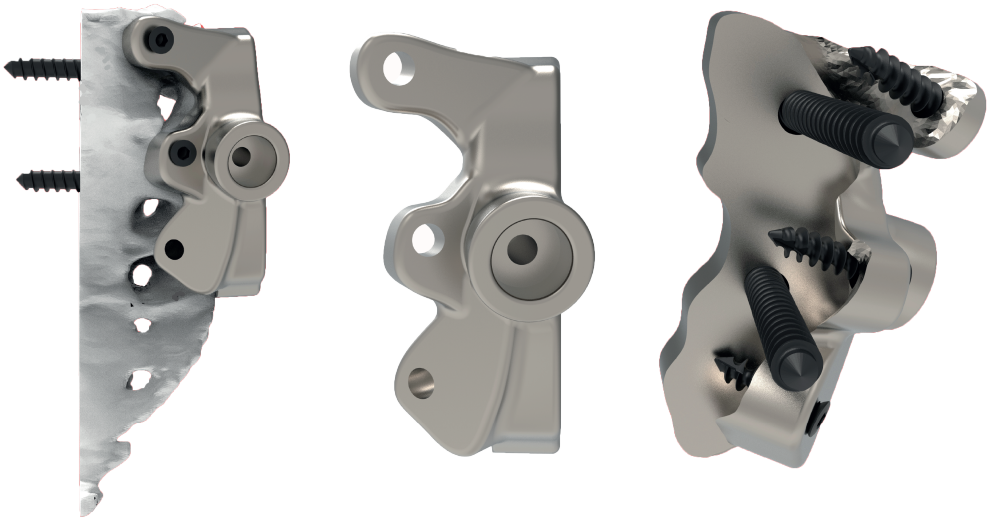

TU Delft Delft University of Technology

Department of Orthopaedic Surgery
Leiden University Medical Center

Sacral Anchoring of the LUMiC Prosthesis

Development of a protocol to in vitro evaluate newly designed 3D printed patient specific prosthesis for the sacrum after tumour resection.

by

L. van Rijn

to obtain the degree of Master of Science
at the Delft University of Technology,
to be defended publicly on Thursday September 23, 2020 at 15:00.

Student number:	4525531	
Thesis committee:	Prof. dr. A. Zadpoor,	TU Delft, supervisor
	S. Janbaz,	TU Delft
	Prof. Dr. S. Dijkstra,	LUMC
	Dr. ir. B.L. Kaptein,	LUMC

TU Delft

Contents

Abstract

After en bloc resection of primary pelvic bone tumours, orthopaedic oncologists usually try to perform reconstruction in order to achieve limb salvage. Reconstruction after these types of resections is challenging. Especially when the total ilium and parts of the sacrum needs to be removed. One of the reconstructive options is endoprosthetic fixation to sacral bone with the LUMiC prosthesis, but using the LUMiC prosthesis in the sacrum resulted in poor clinical results. Emerging new production techniques such as 3D printing provide for customised prostheses that could be an adequate reconstructive option in these cases and could complement the LUMiC prosthesis to enable sacral anchoring of the LUMiC prosthesis. One of the challenges of customised prostheses is that they are not 'off the shelf' and therefore are all different in terms of geometry and, thus, performance. Therefore, these implants cannot be subjected to stringent regulations and registrations used in conventional arthroplasty. In order to ensure maximal safety of these implants we must perform biomechanical testing before implantation. Unfortunately, the bone models for biomechanical testing currently available are not validated on implant fixation and thus unreliable for prosthesis testing. Therefore, in this thesis a new prosthesis that enables sacral anchoring of the cup of the LUMiC prosthesis is designed and two strategies are developed in order to mechanically evaluate this newly designed prosthesis for the sacral anchoring of the LUMiC cup. First strategy is using Finite element modelling to develop a model of the sacrum with implanted prosthesis. Second strategy is the development of 3D bone models of the sacrum using 3D printing together with performing experiments to mechanically evaluate the newly designed prosthesis. Four different mechanical bone models with different shell thickness and infill density were developed and compared to the FE model. Results showed that the new prosthesis design performed better in terms of micromotions between implant and bone compared to the use of the old LUMiC stem in the FE model. Furthermore, a 3D printed mechanical bone model with shell thickness of 1mm and infill structure of 20% showed most comparable results in terms of micromotions between implant and bone compared to the developed FE model. There could be concluded that the FE model and the development of 3D printed mechanical bone models together with the experiments are good starting points in the development of a protocol to *in vitro* evaluate newly designed 3D printed patient specific prosthesis for the sacrum after tumour resection. The mechanical bone model with shell thickness 1mm and infill structure 20% is the best option in terms of mimicking real bone. Furthermore, the newly designed prosthesis for sacral anchoring of the LUMiC cup showed promising results and could be considered as a improved alternative for the old LUMiC prosthesis stem. In future research cadaver tests should be performed to further validate the found results.

L. van Rijn
Delft, September 2020

1

Introduction

Implants are often used in joint arthroplasties, spine fixation, tissue reconstructions and fracture fixation. In the coming years the clinical need for orthopaedic implants will increase. Research has shown that the demand for total knee arthroplasties (TKAs) in the USA will grow from 719,000 annual TKAs in 2015 to 3,48 billion in 2030. This represents a grow of 484%. On the other hand, the demand in total hip arthroplasties (THAs) will grow 172% from 332,000 in 2015 to 572,000 in 2030 [22],[34]. In particular for younger patients under 65, joint arthroplasties will increase substantial [35]. In total joint replacements the bone is uniformly prepared to fit the implant. This could lead to an uneven weight distribution on the implant risking decreased bone remodeling and eventually failure of the implant [22]. For this reason the interest in patient specific implants (PSIs) increases and is more and more used in orthopaedic surgery. In PSIs magnetic resonance imaging (MRI) or computed tomography (CT) is used to create an implant specific for a patient its unique anatomy [47]. Although research shows promising applications for PSIs [22] orthopaedic health professionals still show low confidence in PSIs. In a survey filled in by 15,000 AAOS (American Academy of Orthopaedic Surgeons) only 47% saw benefits in using PSIs over traditional implants [7]. The promising applications for PSIs, but the low confidence shown by health professionals indicates more research is required in the field of PSIs. The rise of new additive manufacturing techniques as 3D metal printing leads to new possibilities in PSIs. This 3D metal printing technique is most often used for reconstruction of bone structures after *en bloc* resection of a bone tumour in the hip or knee [27].

This thesis project is focused on 3D printing of custom-made implants. The project is in cooperation with the Leiden University Medical Centre (LUMC). There are four categories of custom made 3D printed implants that are already used in a clinical setting at the LUMC (see figure 1.1). These categories are:

1. 3D-planning of a special implant
2. Custom made implants complete
3. Custom made implants partial
4. Instruments

This project is focused on implants in the custom made implants partial category and especially on special made partial implants for the hip region. 3D printed implants are mostly made out of titanium. As a short introduction of 3D printed titanium implants, the process chain of 3D printed titanium implants is shown in figure 1.2. First step in this process is to make a CT or MRI scan of the patient in order to get access to the patient specific anatomy. The CT or MRI scans are then used to produce a 3D model of the patients anatomy. This 3D model is used to make a CAD design of a custom made complete or partial implant. The design is then printed out of a powder titanium material with additive manufacturing techniques. After printing the design is finished, cleaned and sterilized to prepare it for implantation into the patient. In the end, the design is implanted into the patient during surgery.

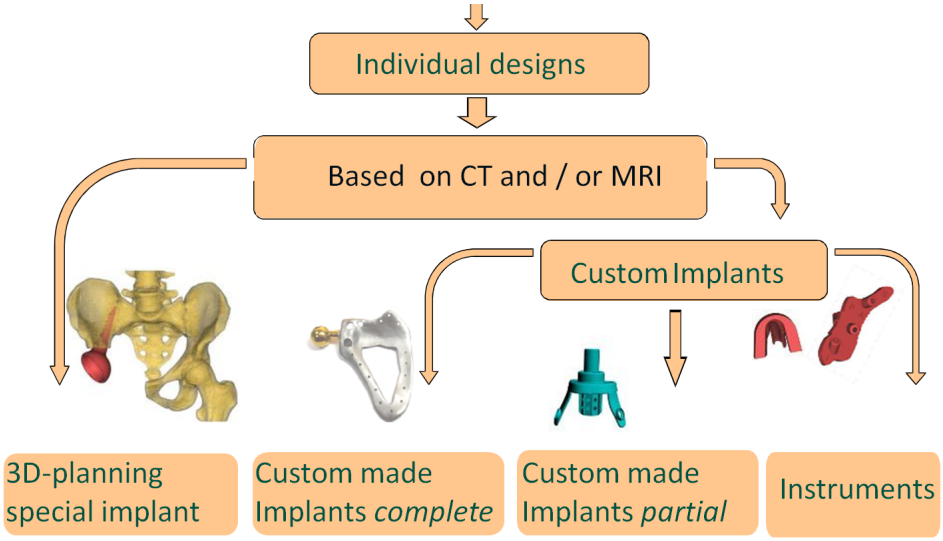

Figure 1.1: Categories of custom made 3D printed implants used at the LUMC. This thesis will focus on category 2L: Custom made implants partial

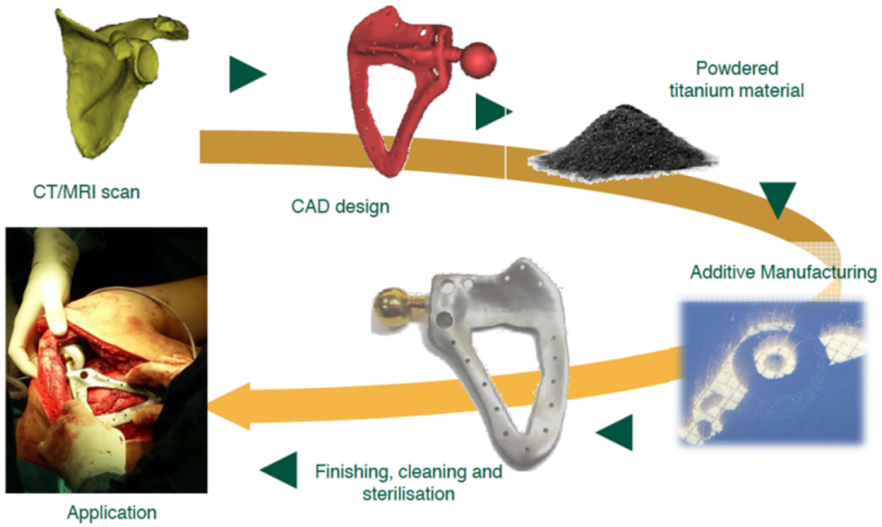

Figure 1.2: The process chain of 3D printed titanium implants. First a CT or MRI scan of the patient specific anatomy is made. The CT or MRI scans are then used to produce a 3D model. This 3D model is used to make a CAD design of a custom made complete or partial implant. The design is then printed out of a powder titanium material with additive manufacturing techniques. After printing the design is finished, cleaned and sterilized to prepare is for implantation into the patient. Lastly, the design is implanted into the patient during surgery.

As mentioned above custom-made patient specific implants can be used for all different kind of purposes and in all parts of the body. The motivation for this project are patients with bone cancer expressed as an osteosarcoma, chondrosarcoma or Ewing sarcoma (see figure 1.3). Osteosarcoma is a malignant form of cancer that starts in the bones leading to tumours.The cancer cells in osteosarcoma tumours show resemblance with osteoblasts, that normally form new bone. However in an osteosarcoma the formed bone tissue is not as strong as for normal bone tissue [1]. Although, in the past the survival rate for patients with osteosarcoma was around 10-15 % nowadays a multidisciplinary approach to treat osteosarcomas has led to an increase in survival rate to 60 %. The multidisciplinary treatment consists of neoadjuvant chemotherapy, meaning chemotherapy prior to surgery, and wide excision of the primary tumour. The gold standard in treatment of osteosarcoma nowadays is limb-salvage surgery [51]. A characteristic for chondrosarcoma is that the cells of the tumour produce cartilage instead of

bone as is the case in osteosarcomas. Again wide excision of the primary tumour is the preferred surgical treatment. Chemotherapy is only in few cases effective [33]. The cells responsible for the Ewing sarcoma are still unknown. The tumour can originate from the bone or the soft tissue around the bone. The Ewing sarcoma occurs mostly in patients between the 5 and 30 years old and strikes 30-35 people each year in the Netherlands, which makes it a very rare form of cancer. Treatment consists of removal of the tumour, chemotherapy and radiotherapy [18]. An overview of this three forms of bone cancer tumours are shown in figure 1.3.

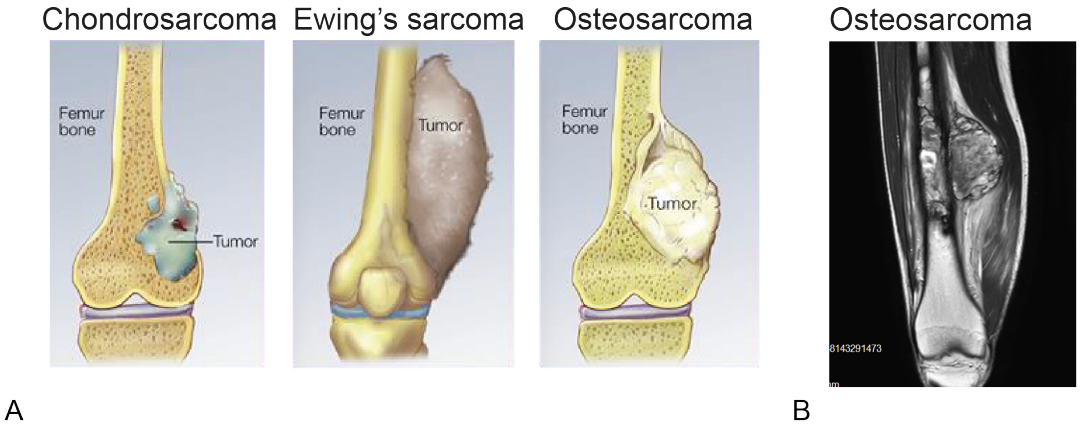

Figure 1.3: A: Representation of Chondrosarcoma, Ewing's sarcoma and Osteosarcoma in the knee. B: CT scan of patient with tumour caused by osteosarcoma [4].

A tumour can be excessively large in bone cancer, leading to sacrificing large parts of the bone. An example of a bone tumour in the hip is shown in figure 1.4. The tumour of figure 1.4.B is infiltrated in the whole hip region, leading to removal of the ilium and part of the sacrum (show in figure 1.4.A). This project is focused on resection of the hip joint with often a resection of the ilium, pubis and ischium. Leaving the patient with place for implant fixation only at the sacrum. For a few of these patients the LUMiC implant as shown in figure 1.5 is inserted in the sacrum at the LUMC. The LUMiC prosthesis consists of a separate stem (hydroxyapatite-coated), which can be fixed uncemented or cemented. Second part of the LUMiC is the acetabular cup. The LUMiC prosthesis is shown in figure 1.5.A. The stem and cup are on the market in different sizes and the cup is also available with a silver coating for infection prevention. The LUMiC is equipped with sawteeth so rotational adjustment of the position of the cup is possible after implantation of the stem [4]. Anchoring of the LUMiC stem to the sacrum is shown in figure 1.5.B and figure 1.5.C. In research prior to this project the anchoring of the LUMiC in the sacrum is retrospectively reviewed in 10 patients. Results were a dislocation in four patients and loosing of the prosthesis in three patients after 28 months. There is concluded that there is a poor clinical result for the LUMiC as sacral fixation [12]. Therefore, there is a need for a new designed implant part enabling fixation of the LUMiC cup to the sacrum.

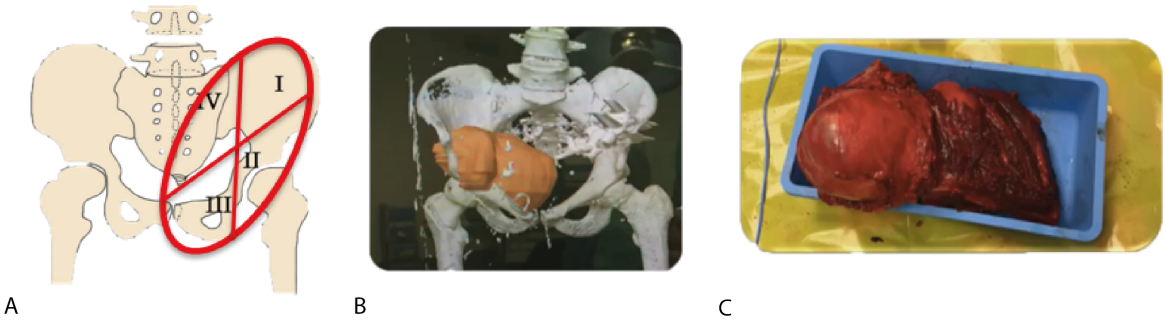

Figure 1.4: A: Tumour resection of tumour shown in B leads to sacrificing large parts of the ilium and sacrum. B: Overview bone tumour in the hip of a patient. C: Tumour after resection from the patient.

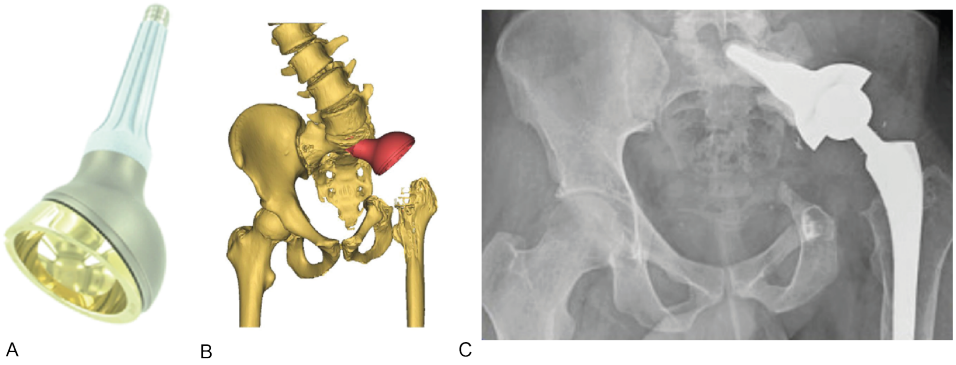

Figure 1.5: A: overview of LUMiC prosthesis used at the LUMC. B:Anchoring of the LUMiC prosthesis in the sacrum. C: CT scan of anchoring of the LUMiC prosthesis in the sacrum.

Besides the LUMiC prosthesis of the LUMC other limb salvage surgery techniques using 3D metal printing for the sacrum are discussed in literature. Prior research on 3D printed patient specific prosthesis used in the hip is done by Wuisman et al. (2001) [62], Wei et al. (2017) [60], Zhao et al. (2018) [65] and Kim et al. (2017). All research will be discussed shortly below.

In a report of Wuisman et al. (2001) [62] a 42-year old woman received an patient specific implant as shown in figure 1.6. The woman suffered from an aggressive tumour and a highly malignant, primary osteosarcoma. En bloc resection of the sacrum with parts of both iliac wings was planned (see figure 1.6). First a 3D model based on CT data was constructed, resection was planned on the 3D model and a prosthesis was designed. The prosthesis consisted of five titanium parts. Wax models of the implant were made. Special instruments for precise osteotomies, insertion and fixation of the parts were constructed. Finally a real size model was used to check the exact fit of the prosthesis. After surgery no infection was found. After five weeks the patient was mobilized in a wheelchair, regained standing capabilities and could walk short distances with crutches. After 3 years, the patient was still disease free, could walk in the house and short distances outside with a cane and experienced no pain or pelvic instability. Furthermore, no loosening of the device or screws was observed. Wuisman et al. (2001) [62] mentioned the following advantages for using an 3D real size model; the 3D real size model offered surgeon the advantage of wide bony resection marges can be drawn on the model and the individual custom-made prosthesis can be designed and tested before intervention. Biomechanical studies to assess loads and stability after total sacrectomy and of the custom made prosthesis could not be assessed prior to surgery.

In a second case study of Wei, Guo, Ji, Zhang, and Liang (2017) [60] a 62-year old man with a total en bloc sacrectomy of a sacral chordoma received A 3D printed custom made prosthesis with 3 bone-contacting surfaces. The prosthesis is shown in figures 1.7. There were no peri-operative complications and at three months follow up no loosening or fracture of the prosthesis was detected on CT data. After 8 months CT data showed two fractured screws in bilateral ilia. At 1 year follow up patient was disease and pain free and experiences no spinopelvic instability. The patient could walk in- and outdoor short distances with crutches.

In the case described in Zhao et al. (2018) [65] a 51 year-old male which had previously undergone semi-pelvic resection of a chondrosarcoma and semi pelvic prosthesis implantation is described. Unfortunately, loosening of the prosthesis occurred and a new custom made 3D printed was developed. The prosthesis consisted of two parts and is shown in figure 1.8. At 6 months follow-up the patient had good hip joint function and CT scanning revealed good prosthesis positioning. A FEM model showed peak stresses of the design of 164,53 MPa and micromotions of 26,5 micrometer. Both under the boundary value for patient failure [44].

In the case study of Kim et al. (2017) [32] a 16-year old girl with sacral osteosarcoma is treated with hemisacrectomy and sacral reconstruction using a 3D printed implant. After implantation post-operative pain was very limited and the patient could walk after two weeks. At 1 year follow-up no complications were found, instrumentation remained well and bone ingrowth was sufficient. The design of the implant and the 3D implant design process is shown in figure 1.9.

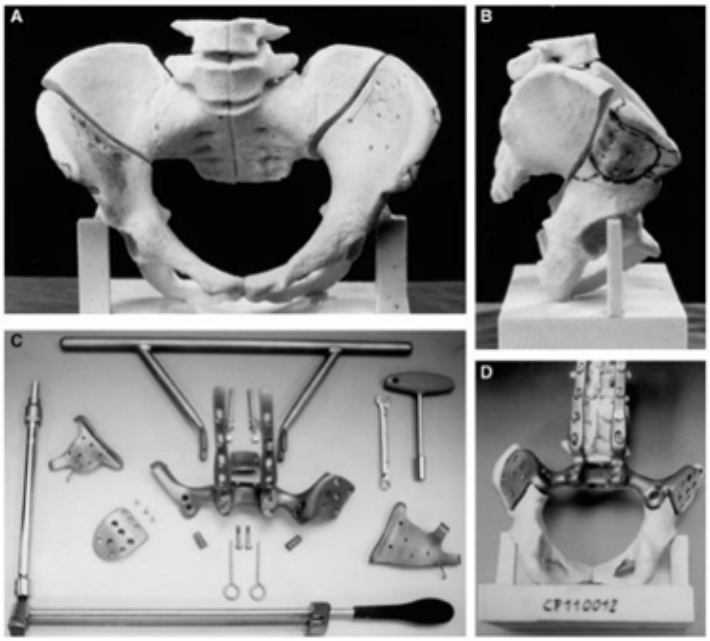

Figure 1.6: Patient specific implant for 42-old woman after en bloc resection of osteosarcoma of the sacrum and parts of both iliac wings [62].

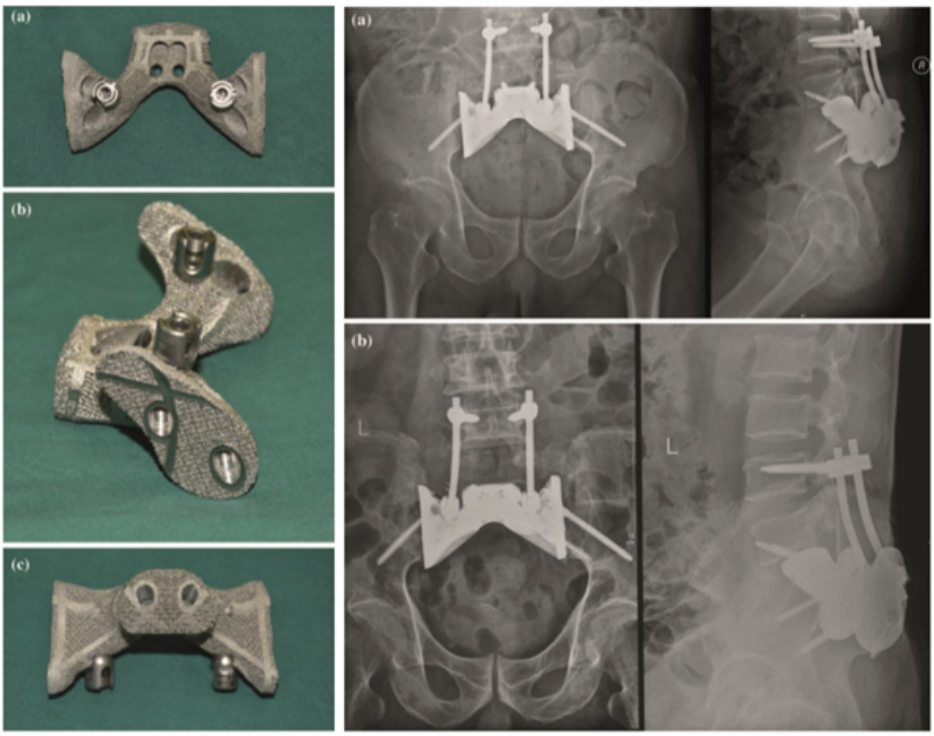

Figure 1.7: A 3D printed custom made prosthesis of Wei et al. (2017) [60]

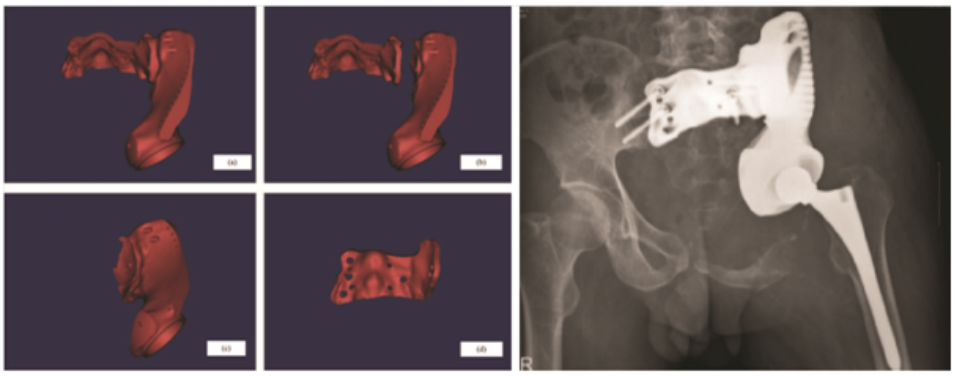

Figure 1.8: The prosthesis of Zhao et al. (2018) [65]

Figure 1.9: The prosthesis of the research of Kim et al. (2018) [32]

All case studies described above, used 3D printing techniques to produce a patient specific implant for patients with a resected bone tumour that infiltrates the sacrum. Results of these case studies are promising, because almost no complications occurred. The low complication rates in the described case studies show that using the 3D printing technique performs better than using the LUMiC prosthesis stem for anchoring in the sacrum bone at the LUMC till now. Therefore, this project is focused on improving the anchoring of the LUMiC prosthesis by designing a 3D printed part that allows the LUMiC prosthesis to be firmly and safely attached to the sacrum bone. From now on called simply prosthesis design. Although, the case studies showed promising results no standard protocol is used to design this kind of patient specific prosthesis for the sacrum. Furthermore in all case studies no biomechanical evaluation of the designs was performed before implantation. It is important to biomechanically test the designed implant prior to surgery. This can be done by inserting the implant in cadaver bone or in composite bone models as saw bones. For biomechanical testing, a prosthesis is inserted in cadaver bone and loaded using a force-tensile machine. These tests are very expensive and in the case of 3D printed implants, the implant is patient specific making the generic testing with cadaver bones less realistic. For these reasons, in-silico testing using a patient specific finite element model would be a more realistic option. Another option would be to print a patient specific bone model that can be used for testing in a force tensile machine. but currently, these patient specific 3D printed bone models do not have the mechanical properties of real bone.

Goal of the project is to design a prosthesis which enables anchoring of the LUMiC cup to the sacrum bone using new 3D printing techniques while at the same time develop a standard protocol that enables biomechanical evaluation of 3D printed sacral implants using bone models. The structure of the project and the details about how to achieve this goal will be discussed in chapter 1.1.

1.1. Project overview

The aim om the project is to develop a protocol to *in vitro* evaluate newly designed 3D printed patient specific prosthesis for the sacrum after tumour resection. An overview of the project is shown in figure 1.10.

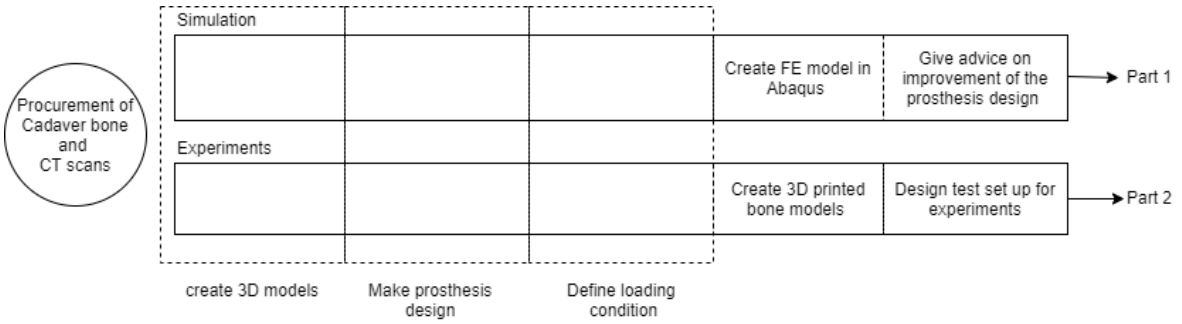

Figure 1.10: An overview of part 1 and 2 of the thesis.

Two strategies to achieve the main goal are used in this thesis. First strategy is to do a simulation study by developing a FE model of the sacrum in which newly designed 3D printed patient specific prosthesis are implanted, loaded and micromotions between implant and bone are evaluated. Cadaver bones will be used as a template for the FE model.

Second strategy is to develop mechanical bone models of the sacrum that can be used during mechanical tests. Cadaver bones will be used as a template for the mechanical bone model of the sacrum. The implant is implanted into the mechanical bone model and loaded in a force-tensile machine. The micromotions between implant and bone during loading are measured. In this way it is possible to ensure a good biomechanical performance of the newly designed prosthesis before implantation. Until now mechanical tests are mostly done on cadaver bones or composite bone models (chapter 1.3). Cadaver bones cannot be used for testing 3D printed patient specific prosthesis because is is not possible to have access to the cadaver bone of the specific patient in need of the implant. Furthermore, the procurement of cadaver bones is challenging and the costs are high. Composite bone models of the sacrum cannot be used in mechanical tests for this type of implants either, because there is no composite bone model on the market that mimics the mechanical properties of real bone sufficiently. Furthermore, it is very hard to mimic the patient specific anatomical structure of the bone with composite bone models due to the available production options for composite. In order to perform mechanical tests on 3D printed patient specific implants a new mechanical bone model needs to be developed. The goal for the second strategy is the development of a new mechanical bone model of the sacrum that can be used for mechanical tests. This will be done using 3D printers and the material plastic polylactic acid (PLA). Several bone models with a variety of print parameters will be produced. The newly designed prosthesis part will be implanted in all different bone models and loaded in the force-tensile machine with earlier defined loading scheme. The micromotions between implant and bone model will be evaluated and compared to micromotions measured in the FE model. Eventually, a recommendation on which mechanical bone model mimics real bone best will be done.

To elaborate on both strategies this thesis report is composed out of two pars. First part is the creation of a FE model of the sacrum with implanted prosthesis. Second part is to develop a mechanical bone model of the sacrum that can be used to do biomechanical tests. An overview is shown in figure 1.10.

As shown in figure 1.10 first step is to procure the sacral cadaver bones that will act as a template for the FE model and the mechanical bone model. The procured cadaver sacra will be scanned with a CT scanner to get access to the geometry of the sacra. This part will be elucidated in chapter 2.1. To continue three steps were taken that are required for both strategy 1 and strategy 2. First, the CT scans of the cadaver sacra are transformed into 3D models. One sacra is chosen as the template for the FE model and the mechanical bone model. This part will be elucidated in chapter 2.1. After selection

of one sacra a prosthesis design is made to perfectly fit this chosen sacra. This prosthesis design is then used in the simulation of strategy 1 and in the biomechanical tests of strategy 2. More about the prosthesis design can be found in chapter 2.2. Furthermore a loading scheme had to be defined. The same loading condition is used in the FE model and in the experiments. The definition of the loading scheme is explained in chapter 2.3. After finishing these 3 steps the FE model could be developed for strategy 1 of the thesis and the development of the mechanical bone models for strategy 2 could be executed. These steps are explained in respectively chapter 2.4 and chapter 2.5. For strategy 2 the final step was to design a test set up in which the mechanical bone models with the implanted prosthesis of chapter 2.2 can be loaded with the loading scheme of chapter 2.3. Furthermore the FE model is used to test the prosthesis design of chapter 2.2 and an advise for improvement of the design is given at the end of chapter 4.1. Above can be summarized as follows (see also figure 1.11):

- Main goal: Development of a protocol to *in vitro* evaluate newly designed 3D printed patient specific prosthesis for the sacrum after tumour resection.
    - ◊ Sub-goal 1: Prosthesis Design allowing anchoring into the sacrum bone.
        - · Give advice on improvement of prosthesis design.
    - ◊ Sub-goal 2: Development of FE model of the sacrum.
    - ◊ Sub-goal 3: Development of mechanical bone models of the sacrum.
        - · Give recommendation on best mechanical bone model.

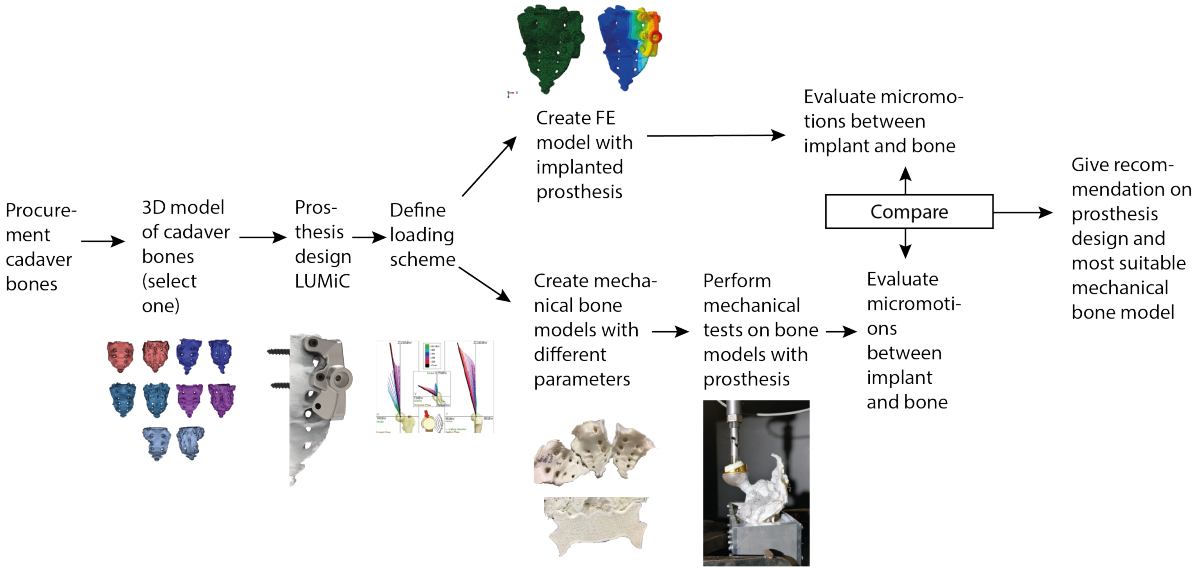

Figure 1.11: Overview of thesis project. First step is to procure cadaver bones and create 3D models of the cadaver bones. Afterwards one cadaver bone is chosen as an template for the prosthesis design and a FE model together with several 3D printed mechanical bone models with a variety of print parameters are created. Experiments with the mechanical bone models are executed and micromotions are evaluated. The resulting micromotions in the FE model and in the experiments are compared in order to give recommendations on the prosthesis design and the mechanical bone models.

The report will start with several introductory paragraphs (chapter 1.2 till chapter 1.6) that will give some background information on the concepts used throughout this thesis report.

1.2. Anatomy of the pelvis

In this part the anatomy of the pelvis will be elucidated to give a general understanding of the concepts used throughout this thesis report.

The hip joint consists of the pelvic girdle, the pelvic spine and the femur. The pelvic girdle consists of the ilium, ischium and the pubis and is shown in figure 1.12. The pelvic spine consists of the sacrum and the coccyx. The pelvic girdle is formed by two hip bones (coxal bone or os coxae). The hip bones

consists of the ilium, the pubis and the ischium. At the point of fusion of the ilium, ischium and pubis there is a deep socket receiving the femur head which is called the acetabulum [38]. Each hip bone unites with the other hip bone anterior (front) and with the sacrum posterior (back). The sacrum is shown in more detail in figure 1.13. The sacrum is of triangular shape. The superior (high) part is weight bearing in contrast to the inferior (low), non-weight bearing apex. The sacrum is formed by the fusion of five sacral vertebrae (S1-S5). The lines of fusion of the vertebrae can be seen as four transverse ridges (figure 1.13). On the posterior surface of the sacrum the median sacral crest shows, which consists of the fusion of the spinous processes of the vertebrae. The articular surface is the place where the sacrum joins the ilium and forms the immobile sacroiliac joint of the pelvis. A bony tunnel is passing through the sacrum called the sacral canal. The anterior and posterior surface of the sacrum contains a series of paired openings called the sacral foramina, which are connected to the sacral canal. These openings are important for the anterior and posterior branches of the sacral spinal nerves to leave the sacrum. The sacral spinal nerves are shown in figure 1.14. The superior articular process of the sacrum articulates with the inferior articular processes from the L5 vertebra [8].

Figure 1.12: The pelvic girdle and pelvic spine [8]

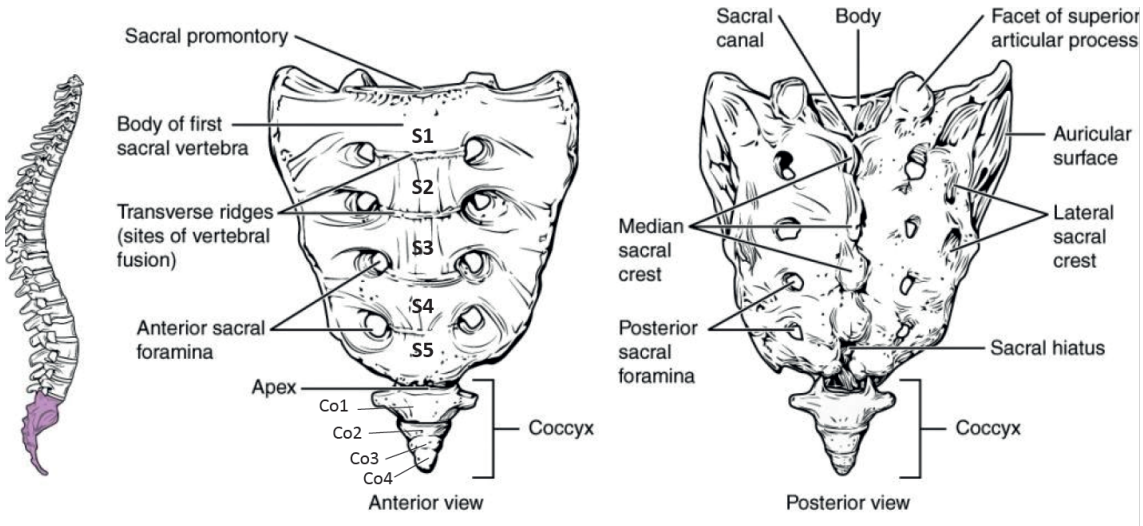

Figure 1.13: The sacrum front and back view [8]

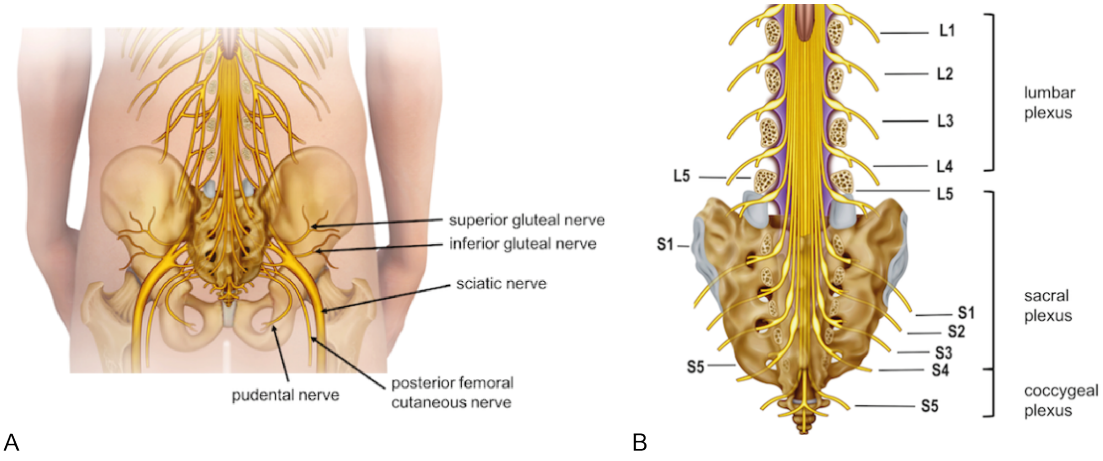

Figure 1.14: A: Nerves of the pelvis anterior view [52]. B: Nerves of the pelvis posterior view [52].

1.3. Structure and material properties of bone and bone models

In this part the strucuture and mechanical properties and bone and mechanical bone models as composite bone models will be elucidated to give a general understanding of the concepts used throughout this thesis report.

1.3.1. Structure and material properties of bone

The bone consists of a dense outer layer of cortex bone. This cortex bone sandwiches spongy bone, also called trabecular bone or cancellous bone. This cancellous bone is composed out of needle like pieces called trabeculae. The cancellous bone give rise to cavities in the inside of the bone. This structure gives bone an optimum mass-to-strength ratio. The inner part of the bone is called the endosteum (or medulla) and contains the bone marrow. The bone marrow lies in between the open spaces of the trabeculae. An overview of the bone structure is shown in figure 1.15.

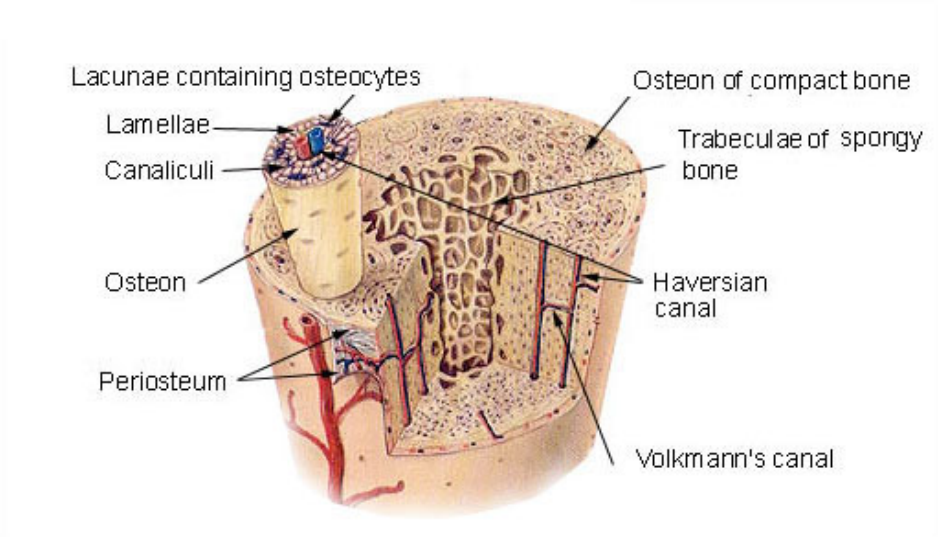

Figure 1.15: sketch of section of bone showing features of the cortical bone of a long bone [38]

The density of cortical bone is determined by the wet weight divided by the specimen volume. It is a measure of both the porosity and mineralization of the bone. Cortical bone has a density of 1.9 g/cm^3. Bone mineral density (BMD) is the bone mineral mass per unit bone volume [13]. On the other hand

bone mineral content (BMC) is the ratio of unit weight of the mineral portion to dry bone unit weight and is mostly given in a percentage.

In general bone is a hierarchically-organized material that is constructed as a fiber-reinforced composite material, which makes bone a highly anisotropic material [39]. For the mechanical properties of bone a distinction at histological level between cortical and cancellous bone should be made. The tissue that forms the cancellous bone can be lamellar, which means sheet-like, or completely disorganized. At microscopic level osteons (the Haversian system as shown in figure 1.15) act as strong fibers in a matrix of lamellae [39]. The mechanical properties of a whole bone in bending tests is shown in table 1.1a. The mechanical properties are compared with other common tissues and biomaterials in figure 1.16. Striking is the much lower elastic modulus and ultimate strength for bone compared to other metals as titanium, stainless steel and CoCr.

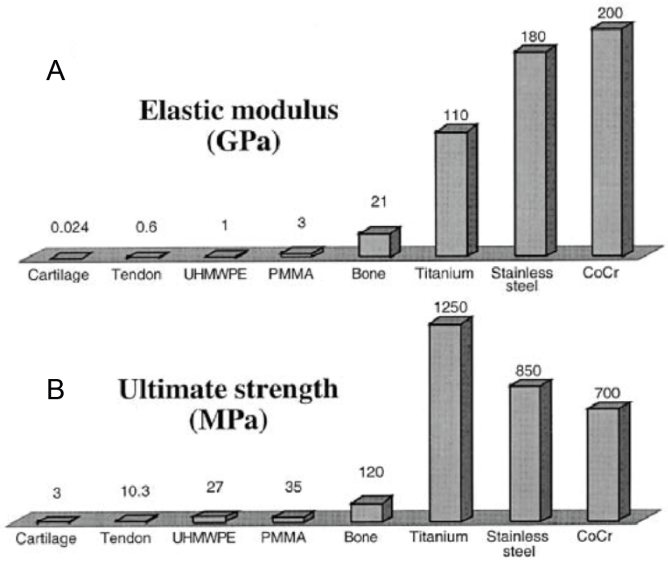

Figure 1.16: Elastic modulus (A) and strength (B) of cortical bone and other common tissues and biomaterials [13]. Striking is the much lower elastic modulus and ultimate strength for bone compared with metals titanium, stainless steel and CoCr.

1.3.2. Mechanical bone models

In orthopaedic biomechanic research often cadaveric bones are used for testing. In this tests a newly designed prosthesis is implanted into cadaver bone and loaded in the loading machine to see if the implant performs well in before implanting into the patient. Cadaver bones are not optimal because of a variety of reasons from high costs, low availability and inconsistency between specimens. Furthermore, cadaver bones are almost always procured from elderly of which bone quality may not be representative for the orthopaedic patient population. To address this problems composite bone models have been developed. Composite bone models are, in comparison with cadaver bone, less expensive, more easily obtained, have minimal variability between specimen and no special storage or preservation is necessary . Composite bone models are manufactured by injection-molding short glass fiber reinforced (SGFR) epoxy around a polyurethane foam core [14]. A example of a mechanical bone model of the sacrum is shown in figure 1.17. The mechanical properties of the composite bone model of the sacrum are shown in table 1.1b. When compared to table 1.1a, the properties are comparable, but that does not mean composite bone models of the sacrum are usable for mechanical tests of the sacrum. Research showed that 4-th generation composite bone models could be used as alternative for cadaver bone for most biomechanical studies of femur, tibia and humerus but are not yet usable to represent mechanical bone properties of short bones, as for example the sacrum, which contain a lot of spongy bone [14]. Because there is no good alternative for composite bone models of the sacrum and cadaver bone of the sacrum also has its limitations this thesis aim is to develop a new mechanical bone model of the sacrum using 3D printing techniques. This will be explained in chapter 2.5.

Table 1.1: Comparison mechanical properties of real bone and composite bone models.

(a) Mechanical properties of whole femur bone [39]

Property	human
Elastic modulus, GPa	
Longtudinal	17.4
Transverse	9.6
Bending	14.8
shear modulus, GPa	3.51
Poisson's ratio	0.39
Tensile yield stress, MPa	
Longitudinal	182
Transverse	121
Shear yield stress, MPa	54
Tensile ultimate stress, MPa	
Longitudinal	133
Transverse	51
Compressive ultimate stress, MPa	
Longtudinal	195
Transverse	133
Shear ultimate stress, MPa	69
Bending ulitmate stress, MPa	208.6
Tensile ultimate strain	
Longtudinal	0.0293
Transverse	0.0324
Compressive ultimate strain	
Longtudinal	0.0220
Transverse	0.0462
Shear ultimate strain	0.33

(b) Mechanical properties of the cancellous bone part of saw bone model of the sacrum [49]

Property	Saw bone
Density (g/cm^3)	1.64
Compression	
Strength (MPa)	157
Modulus (GPa)	17
Poisson ratio	0.26
Tension	
Strength (MPa)	106
Modulus (GPa)	16
Ultimate tensile strain (%)	1.4
Transverse strength (MPa)	93
Transverse modulus (GPa)	10
Transverse ultimate strain (%)	1.2

1.4. Bone response to implants

Some general information about bone response to implants and failure of prosthesis will be given in this part. This information will be used to design an improved LUMiC prosthesis. The final prosthesis design will be showed in chapter 2.2.

Implants are a foreign material for the body. Therefore the body wants to get rid of it. When it is possible to remove the material the body will do so, as is the case for a wooden splinter. If the foreign material consists of small particles or fluid, it will be included by macrophages and removed. A typical tissue response is the forming of leukocytes near the implant followed by forming of macrophages, called foreign body giant cells. If the implants material is chemically and physically inert to the tissue, which means no reaction between implant and tissue will occur, the foreign body giant cells may not form. In this case a thin layer of collageneous tissue will encapsulate the implant. On the other hand, if the implants material is chemically or physically irritant to the surrounding tissue, inflammation will occur [43].

Important requirement for the mechanical stability of implants is the possibility for the bone to grow into the prosthesis. Two terms are used widely in literature on this topic; osseointegration and bone ingrowth. The difference between the two terms is made clear in a review of Kienapfel, Sprey, Wilke, and Griss (1999) [31] in which osseointegration is referred to as the general term for intimate implant surface-to-bone contact. On the other hand, bone ingrowth is referred to as bone formation within a porous surface structure of an implant. The psychiological response to inserted inert porous structured implants resembles the normal healing process of defects of the cancellous bone, but with the newly formed tissue integrating in the void space of the porous material. Repair of holes drilled into the bone is similar to normal fracture healing of the bone. Consequently, the clinical success of fixation with osseointegration and bone ingrowth depends on a immediate stable implant bone interface [31]. For

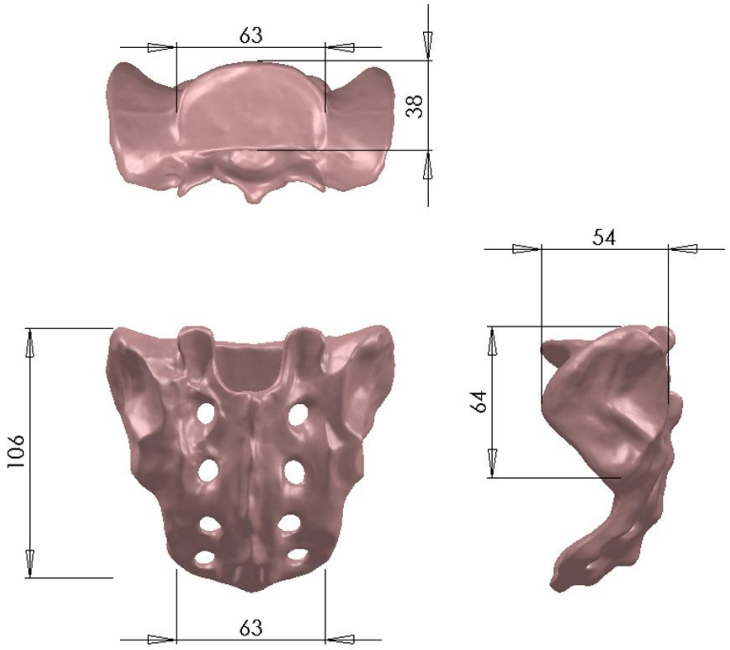

Figure 1.17: Overview of saw bone of the sacrum with dimensions. The saw bone model consists of a PCF cancellous foam core. Cortex bone consists of short fiber filled epxoxy [53].

osseointegration and bone ingrowth new bone formation at implant site is a prerequisite. The new bone formation on the biomaterial depends on the structure of the surface of the biomaterial used. The surface should promote cell proliferation and production of extracellular matrix [31] to ensure osseointegration and bone ingrowth. Wilke et al. (1998) [61] showed that cell proliferation was highest on Hydroxylapatite (HA) surfaces, followed by titanium and chromium-cobalt alloys. In the study of Kienapfel et al. (1999) [31] surface geometry is also mentioned as an important factor for bone ingrowth. Most commonly used surface modifications are metal coatings which are applied by:

- Cast structures
- Sintered structures
- Direct coatings
- Diffusion bonding of preformed structures.

In the research of Kienapfel et al. (1999) [31] there is stated that the optimal range for pore sizes for a porous structure is from 100 to 400 µm. In order to make sure the newly designed improved LUMiC prosthesis has good instant stability, which is stability immediately after implantation, a porous structure will be included in the design. More about the prosthesis design in explained in chapter 2.2.

1.4.1. Failure of Prosthesis

Most common complications leading to failure of a prosthesis are [30]:

- **Infection**: Infection can lead to serious complications after implantation of the prosthesis. Prevention of infection can be accomplished by many strategies including clean operation rooms and the use of antibiotic-containing cement in case of the use of cement to anchor the prosthesis.

- **Dislocation**: Dislocation occurs for example when the ball comes out of the socket in total hip replacements. The risk of dislocation is greater just after surgery when soft tissue structures are not healed yet. There are certain activities and movements the patient should avoid to prevent dislocation. After one dislocation the risk of repeating dislocations increase.

- **Stress-shielding**: Bone loss due to stress shielding is a big problem after implantation of hip prostheses. The bone loss can lead to loosening of the prosthesis. In a poorly designed prosthesis the bone around the prosthesis is not loaded to physiological levels anymore. Consequently, an adverse bone-remodelling phenomenon where bone is resorbed in areas where it is not loaded occur. This unwanted bone remodelling could be the cause of failure due to the weakening and deterioration of bone mass around the prosthesis.

- **Aseptic Loosening**: The major reason for failure of prosthesis is aseptic loosening, which means loosening with absence of infection. A loose hip is a problem because it can cause a lot of pain. There are many factor that can cause loosening, but most common cause is an inflammatory reaction to particles or wear debris. Wear of polyethylene, metal and bone cement produces debris particles. These particles induce bone resorption (osteolysis) and eventually implant loosening. Another common cause for aseptic loosening are micromotions between implant and bone and a lack of initial stability. This will be exemplified in chapter 1.4.2.

Main cause for complications is considered to be poor biomedical design of implants [24]. As mentioned in the introduction the demand on total joint replacements will continue to increase. Moreover, the ongoing trend of younger patients in need for a total joint replacement (TJRs) increases the risk of implant failure as well. Harryson, Robertson, and Nayfeh (2004) [22] state that younger patient have a significantly higher risk of implant failure in TJRs. The presence of micromotion between implant and bone due to uneven stress distribution is the main cause of implant failure in these younger patients [6]. Especially for younger patients, the micromotions are relatively large because of the more active lifestyle of this patient population. Consequently, the success rate for total joint replacement is lower for younger patients when standard implant designs are implanted [23]. The need for a custom made prosthesis is therefore higher in this patient population.

1.4.2. Micromotions

Too much relative motion between implant and bone will cause the tissue to produce fibrous connective tissue instead of bone, which is unfavorable for the implant stability and therefore should be avoided [31]. Several studies have examined the maximum allowed relative motions between implant and bone. Pilliar, Lee, and Maniatopoulos (1985) [45] showed that bone ingrowth occurs when the relative motions are less than 28 µm. Same study stated that motions exceeding 150 µm will prevent bone ingrowth and will only produce fibrous connective tissue instead. In a study of Jasty et al. (1993) [28] bone ingrowth was observed with relative motions of 56 µm. In a different study controlled micromotions of 150 µm in a canine model were imposed. Only fibrous tissue ingrowth was observed in this study [48]. It can be concluded that micromotions should be less than 150 µm in order to allow bone ingrowth and preferable even less than 28 µm.

As mentioned above, micromotions prevent bone ingrowth at the implant bone interface. This is due to uneven stress distribution at the bone surface [22]. In normal joint replacement surgery the bones are reshaped with planar cuts, an oscillating saw and cutting guides to fit the standard implant components. The bone shape that remains is quadratic instead of round as in the original joint shape. Hereby, the forces produced by the patients weight and activities are distributed differently. The new created 'corners' take a disproportional amount of stress while the forces should be evenly distributed over the rounded surface of the joint. This can lead to unsatisfying bone remodeling and eventually loosening of the implant [22]. An advantage of patient specific implant design is that the prosthesis design is already altered to the bone shape of the patient. Therefore, there is minimal need to reshape the bone with planer cuts and the bone shape can remain round as in the original joint shape. Because the bone is minimally altered the stress is more evenly distributed over the rounded surfaces and the chance of loosening of the implant is decreased.

1.5. Bone cancer in the hip

Patients that need a LUMiC prosthesis in general suffer from bone cancer in the hip. In this part some general information about the types of bone cancer in the hip, bone tumour classification and bone tumour resection methods will be explained.

1.5.1. Types of bone cancer in the hip

There are a lot of different types of bone cancer. Bone cancer is defined as cancer that starts in the bone and mostly affects the pelvis or the long bones in the extremities. Bone cancer is very rare and responsible for less than 1% of all cancers. Chordoma, chondrosarcoma and osteosarcoma occurs most often in the hip. In a research of Wang et al. (2015) [58] 50 cases of pelvic tumors from 2003 till 2013 were described. The diagnoses were 21 osteosarcomas, 11 Ewings's saromas, 8 chondrosarcomas, 5 metastatis, 3 fibrosarcomas and 2 giant cell tumours of bone. The patients all received limb salvage surgery and a reconstruction with a modular hemipelvic prosthesis. The recurrence rate in patients with marginal margins for osteotomy was significantly greater than in those with wide margins for osteotomy. For pelvis tumours, limb salvage surgery, combined with chemotherapy and radiotherapy is more favorable than traditional hemipelvectomy, because of more improvement of quality of life and less psychological trauma and physical disability while limb salvage surgery has comparable survival and recurrence rates [58]. We will discuss each type of bone cancer tumours briefly below.

The subtype osteosarcoma is a sarcoma that is initiated in bone tissue. Osteosarcoma is a malignant form of cancer that starts in the bones leading to tumours. The cancer cells in osteosarcoma tumours show resemblance with osteoblasts, that normally form new bone. However in an osteosarcoma the formed bone tissue is not as strong as for normal bone tissue. Although in the past the survival rate for patients with a osteosarcoma was around 10-15%, nowadays a multidisciplinary approach to treat osteosarcomas has led to an increase in survival rate to 60%. The multidisciplinary treatment consists of neoadjuvant, meaning prior to surgery, chemotherapy and en bloc resection of the primary tumor. The gold standard in treatment of an osteosarcoma is limb-salvage surgery for patients with an osteosarcoma in the extremities and carbon-ion radiotherapy for patients with unresectable osteosarcomas [50]. Research showed that the cause of an osteosarcoma can be found in a mutation in the two tumor suppressor genes RB1 and p53 [50].

Furthermore, the subtype chondrosarcoma is also very common. The defining characteristic of chondrosarcoma is that the cells of the chondrosarcoma produce cartilage. Golden standard is surgical removal of the tumour [16].

Lastly, chordomas are rare bu can also make an appearance in the pelvis area. Chordomas arise form transformed remnants of notochord, which is a cartilous skeletal rod supporting the body in all embryonic animals and derived from the mesoderm. The notochord serves as a basis for the axial skeleton. Chordomas prefere the axial skeleton with most common site the sacrum, the skull and the spine. The gold standard is en bloc resection with wide margins and postoperative beam radiation therapy. Chordomas are very rare and account for 1-4 % of all bone malignancies. Unfortunately, chordomas are very recurrent [57]. The different sub types of sarcomas are showed in figure 1.3.

1.5.2. Tumour classification in the hip

In the research of Enneking and Dunham (1993) [15] a tumour classification system associated with four types of pelvic resections or reconstruction is proposed: type I; the ilium, type II; the periacetabulum, type III; the pubis and type IV; the sacrum (see picture 1.18.B). After resection of a type I tumour the lumbosacral junction is still intact an lumbopelvic stabilization is achieved using pedicle-iliac screw and rod fixation with possibly bone grafting [64] as in figure 1.18.A.

After a type II resection a hemipelvic allograft and prosthesis can restore the acetabulum and hip function [19] [20]. However for type IV resections biomechanical changes occur when both the lumbosacral joint and sacroiliac joint (SI joint) are destroyed. Using an allograft could be a good solution in this case. Solely, a major drawback the use allografts is the long period of time necessary before

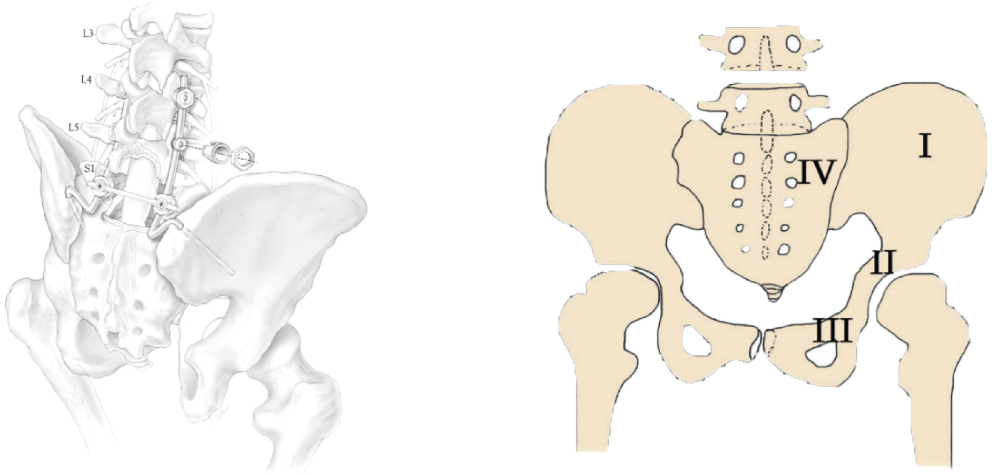

A B

Figure 1.18: A: pedicle iliac screw and rod fixation [26] B: Tumour classification in the pelvis of Enneking [64]

the allograft is incorporated into the bone and full weight-bearing of the joint is possible [64]. Nonunion is the most common allograft related complication [5] [11]. In nonunion there is permanent failure of healing of the bone. Reasons for nonunion can be to much movement after surgery, poor blood supply or an infection. With new additive manufacturing techniques prosthetic reconstruction with a patient specific 3D printed implant can be considered to be a good option a a reconstruction technique after the resection of a type IV tumour [63], [55]. Isolated resection of ilium, ischium or pubis do not require reconstructive procedures [2] [46].

In the research of Zhang, Guo, Yang, et al. (2016) [64] four subtypes for a type IV tumour resection involving the sacrum are proposed. Subtype IVa; invading the ipsilateral sacral wing, subtype IVb; invading the ipsilateral sacral foramina, subtype IVc; invading the contralateral sacral foramina and subtype IVd; invading the whole sacrum (see picture 1.19). For subtype IVa, the tumour is invading the sacral wing therfore, osteotomy plane should be lateral of the sacral foramina. In subtype IVb, the pelvic tumour is invading the ipsilateral sacral foramina and the osteotomy plane lies within the sacral midline. In subtype IVc, the contralateral sacral foramina are envolved and the osteotomy plane should be within the contralateral sacral wing. Finally, for subtype IVd, the entire sacrum is affected. Osteotomy plane should be through the contralateral sacroiliac joint (see picture 1.19, osteotomy planes are indicated with a red line).

En bloc resection is often necessary for patients with sacral osteosarcomas. Total sacrectomy is the most common type of sacral reconstruction till now. Total sacrectomy will induce neurogenic bladder dysfunction and fecal incontinence, gait disturbance, and sexual dysfunction. Hemisacrectomy in combination with reconstruction techniques for the sacrum can preserve the contralateral sacral nerves and may prevent or lessen the complications [32]. Conventional reconstruction methods after en bloc resections in the sacrum can be categorized in three types: spinal pelvic fixation (SPF), posterior pelvic ring fixation (PPRF) and anterior spinal column fixation (ASCF) [60]. These reconstruction methods often do not achieve satisfactory long-term outcomes so there is still a demand for a durable reconstruction [65]. As mentioned before Usage of bone grafts is also described in literature [17] [40] [41] [59], but results often in high complication rates and poor limb function [21] [36]. After sacrectomy dead space is unavoidable, therefore the use of plastic reconstructions is also used in literature [32]. Standard reconstructuion methods for each type of resection is showed in table 1.2. Not for all patients with sarcomas reconstruction surgery is possible. In the research of Guo, Li, Tang, Yang, and Ji (2007) [19] patients with a type IV tumor, tumors that extensively invaded soft tissue or tumors that involved the sciatic nerve were excluded.

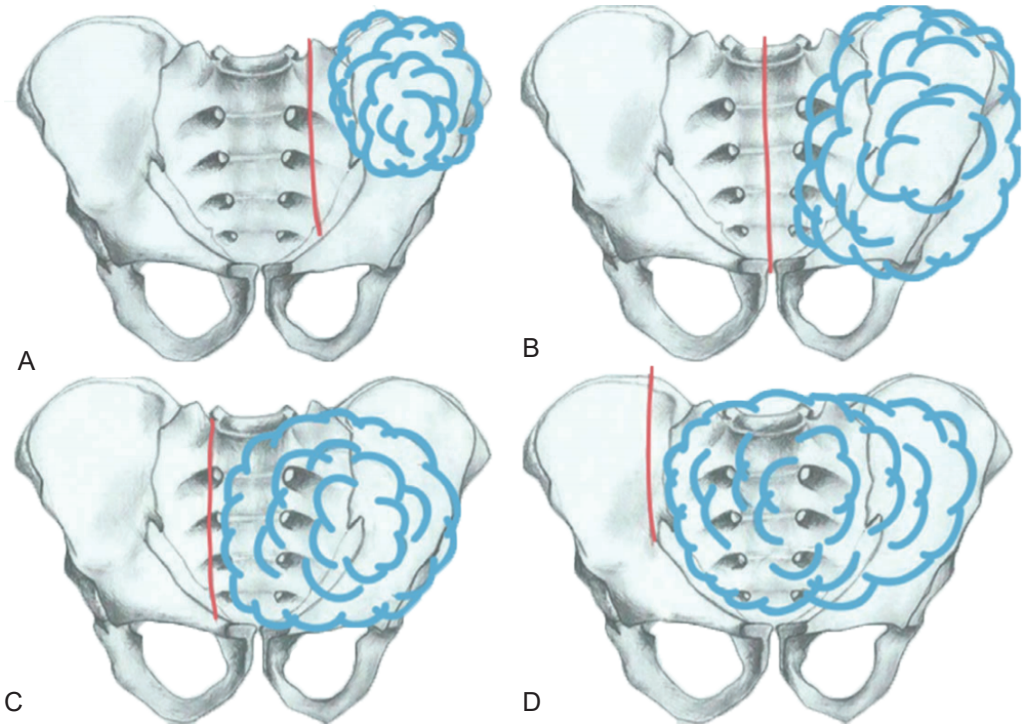

Figure 1.19: tumor classification of subtypes of zhang et al. 2016 [64] the straight lines indicate the osteotomy planes. A: subtype Iva, the pelvic tumor is concentrated to the sacral wing, osteotomy plane should be lateral of the sacral foramina. B: subtype IVb, pelvic tumour is invading ipsilateral sacral foramina. Osteotomy plane should be at sacral midline. C: subtype IVc, the pelvic tumour invades the contralateral sacral foramina. The osteotomy plane should be within the contralateral sacral wing. D: subtype IVd, the entire sacrum is invaded by the pelvic tumour. The osteotomy plane should be through the contralateral sacroiliac joint.

Table 1.2: Standard reconstruction method for each type of resection [64]

Resection involved	**IVa**	**IVb**	**IVc**	**IVd**
I	Unilateral S&R	Bilateral S&R	Bilateral S&R	Bilateral S&R
I+II+III	1) Unilateral or bilateral S&R + MHP* 2) Bone graft + MHP	Bilateral S&R + MHP*	Bilateral S&R + MHP*	Bilateral S&R + MHP*
MHP = modular hemipelvic prosthesis, S&R = Screw and rod fixation * bone graft is optional depending on the surgeon's preference.				

1.6. Introduction to FEM and Abaqus

The basis of the finite element method is to discretize the geometry of a structure by using finite elements. In order words the geometry of a structure is subdivided in smaller simpler parts called finite elements. Each finite element represents a small part of the structure. The elements are joined together by shared nodes. All nodes and elements together form the mesh of the model. After applying load onto the model the Finite element model software, in our case Abaqus 6.14 will calculate the displacements of the loads. Hereafter, stresses and strains can be determined easy by the model.

The total FEM analysis consists of three stages: preprocessing, simulation and postprocessing. In the first stage (preprocessing) the model should be defined and an Abaqus input file (.inp file) is created. In our case the input file is created with 3-matic Medical and Mimics medical software. More on this

topic in section 2.4.2. The simulation is the phase in which the numerical problem difined in the model will be calculated by Abaqus/Standard. In our project a output file with stresses and displacements will be created ready for postprocessing. In the final phase, postprocessing, the output file can be evaluated. This evaluation is generally done in the visualization module of Abaqus to give an visual representation of the results and create a varity of different plots. In the preprocessing phase the model should be defined. An Abaqus model should at least consist of the following components:

1. **Discretized geometry**: Finite elements and nodes represent the basic geometry of the structure being modeled. all nodes and elements together is the mesh of the model. The element type, shape, location and the overall number of elements used in the mesh affects the results after the simulation phase. In general a greater mesh density, meaning more elements in the mesh, results in a more accurate result but also the time required for analysis increases.
2. **Element section properties**: Abaqus had a wide range of elements that can be used.
3. **Material data**: Material properties for all elements must be specified. Minimal material parameters are young's modulus and Poissons ratio.
4. **Loads and boundary conditions**: Loads are used to distort the physical structure and therefore create stress in this structure. On the other hand Boundary conditions are used to fix portions of the model or to move a predescribed amount. In every static analysis the model must be fixed to some amount otherwise the calculation cannot convergence and stop prematurely.
5. **Analysis type**: Most common types of simulations are static and dynamic stress analysis although there are more options of simulation in Abaqus. In static analysis the long-term response to a load is calculated. The dynamic response is mostly used in the effects of a sudden load on the component for example during an impact analysis.
6. **Output requests**.

2

Methods

2.1. 3D models of cadaver bones

As mentioned in chapter 1.1 and indicated in figure 1.10 first step of the thesis is to scan the procured cadaver bones with the CT-scanner and segment the bones to produce a 3D model of the sacrum. Furthermore, the CT-scans are necessary to ensure the bone quality and the absence of bone pathologies of the sacra. First part of the project is to make sure the CTs were made and to segment the CT-scans in order to create 3D models of the procured cadaver sacra.

The cadaver sacra are procured from the VUmc and transported to the LUMC in Leiden. The Sacra were scanned with the Aquilion one CT scan of the department of radiology at the LUMC. Settings of the CT scanner were: 150mA and 135 kV. Two scans were made with different settings. In scan one, the contrast between cortex and cancellous bone is large, which makes it especially adequate for determining cortex thickness of the sacrum and therefore segmentation of the sacrum. In scan two, the geometry of the cancellous bone is shown in more detail. Scan one is used in this project for segmentation of the cadaver bones.

After CT scanning, the data from the CT-scans are visualised with the Radiant Dicom viewer software to ensure the bone quality and absence of bone pathologies. The raw data from the CT-scan of sacrum 3 is showed in figure 2.1. As shown in figure 2.1 the cadaver still contained parts of the Ilium and the lumbar vertebra L5. In the segmentation process these parts are removed. Furthermore, the gaps in the scans due to poor quality of the scans are filled. Segmentation occurred with the software Mimics Medical 21.0. An example of the segmentation process in mimics is shown in figure 2.2. The segmentation threshold was set to bone and then runned to create a mask that includes all the bone in the CT scans. The split and region growing function of mimics were used to mask only the sacrum. Some of the cancellous bone were not included and had to be added to the mask by hand. Filling the voids was accomplished by using editing techniques as cavity fill and the draw function of the Mimics Medical software. The resulting mask was then converted into a 3D surface model by mimics. Unfortunately, when evaluating the CT-scans there was a defect in 3 of 5 delivered sacra which are elucidated in table 2.1. The results of segmentation for all five cadaveric sacra are shown in figure 2.3. Because all sacra were more or less damaged except for sacrum 3, sacrum 3 is chosen as a template for the next steps in the project.

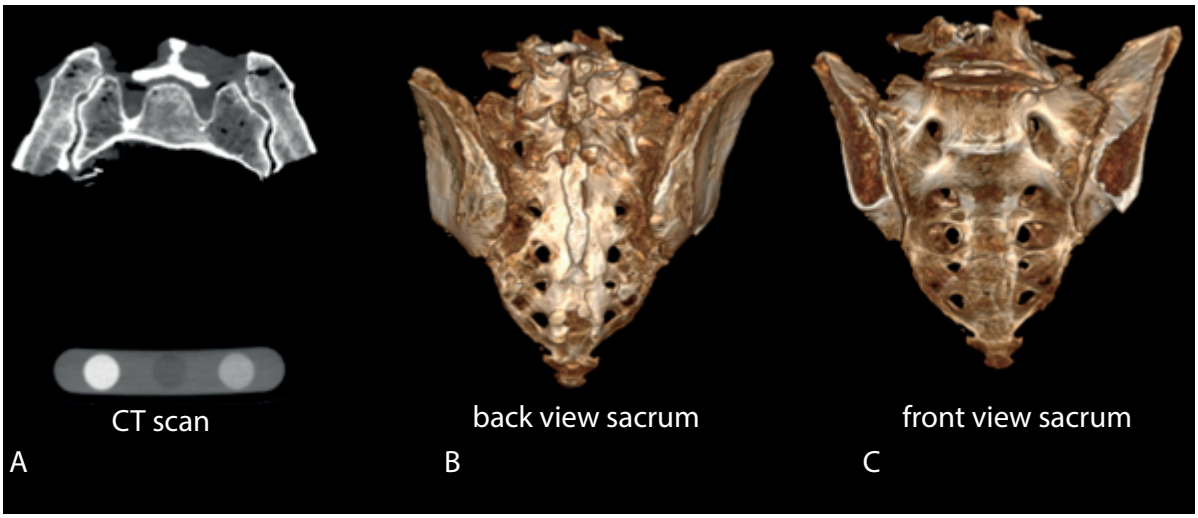

Figure 2.1: A: Raw data of CT-scan of sacrum 3. B and C: CT data visualized with Radiant Dicom viewer, back and front view of sacrum 3. Parts of ilium are still attached and needs to be removed in Mimics Medical.

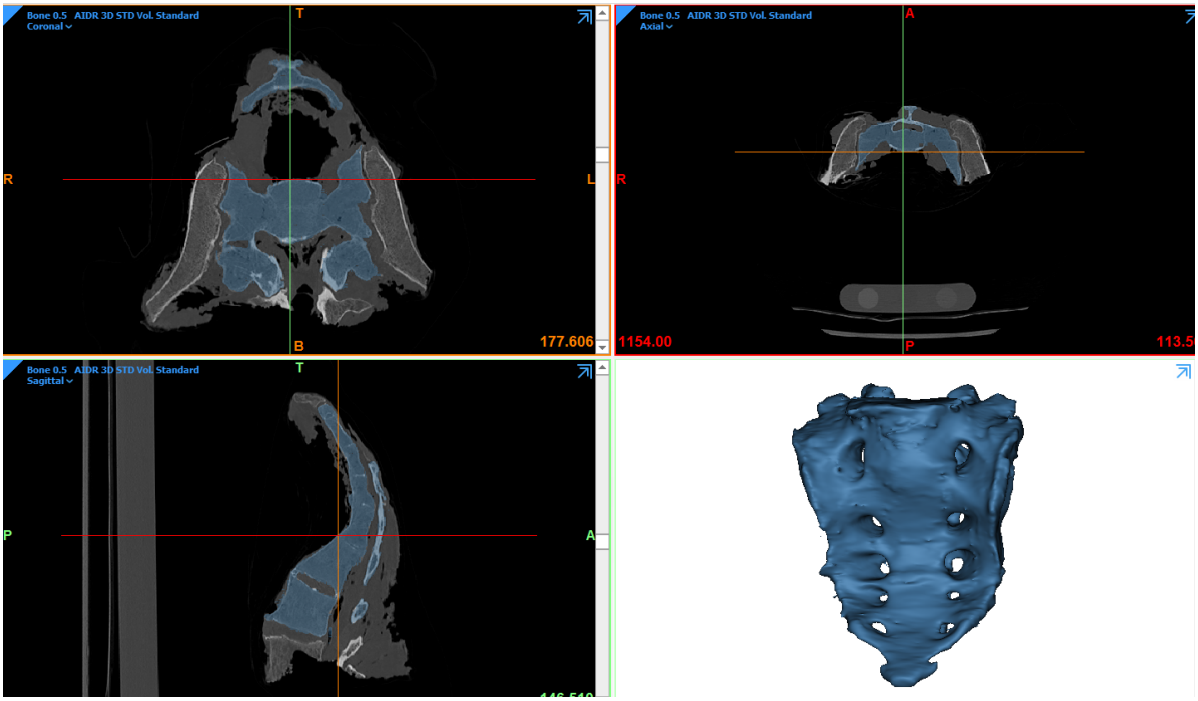

Figure 2.2: Segmentation of the CT-scan in Mimics Medical 21.0 software.

Table 2.1: Overview of the five cadaver sacra and defects for each sacrum.

Sacrum	Damaged or intact
Sacrum 1	- Cortex left part damaged.
Sacrum 2	- Right pars lateralis damaged, not possible to use for testing. - No proc. articularis on both sides.
Sacrum 3	- Intact.
Sacrum 4	- Right part back damaged.
Sacrum 5	- Right side damaged. - Left upper part damaged. - Possibly both sides not usable.

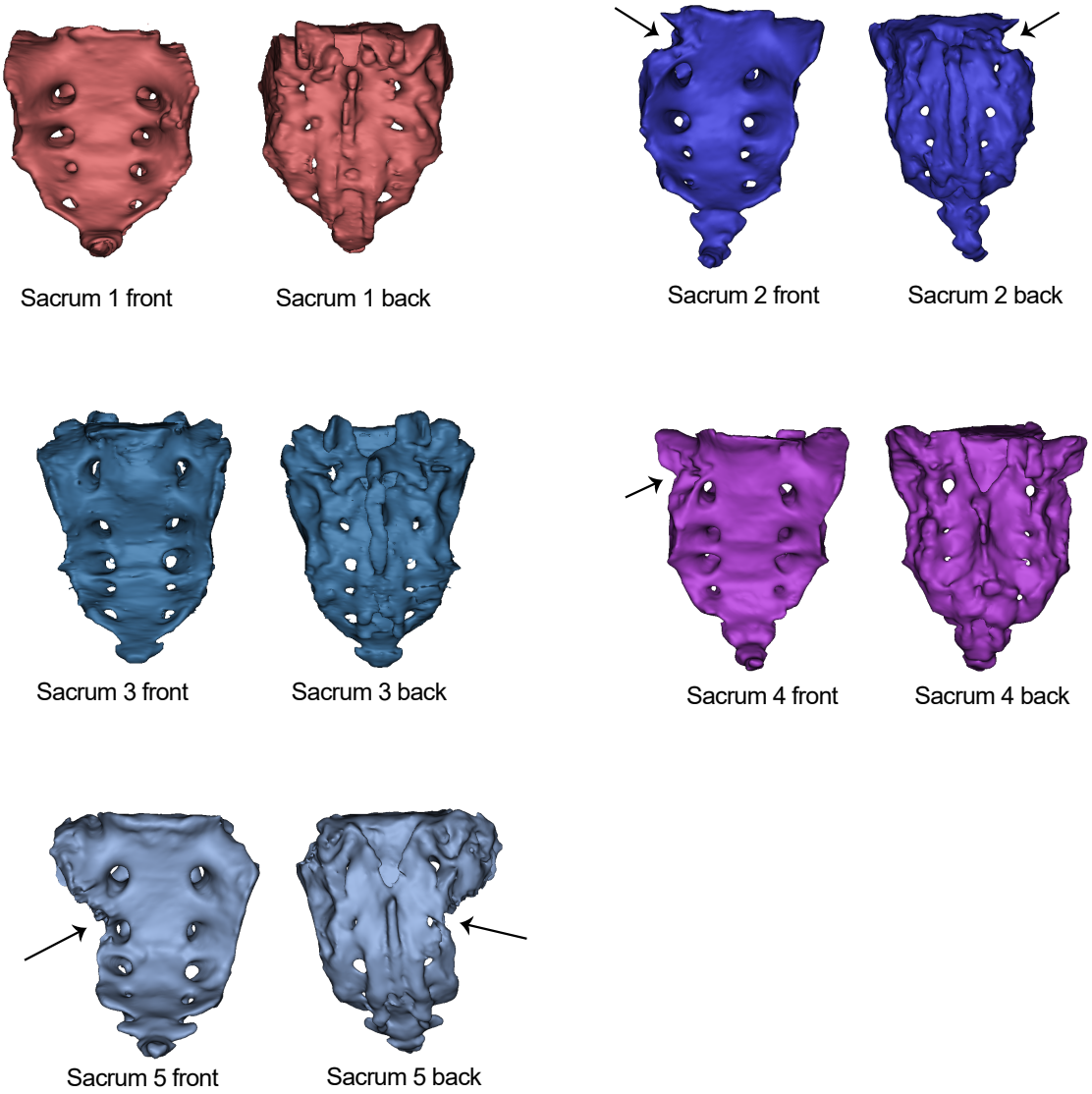

Figure 2.3: Segmentation of all five cadaveric specimen (front and back). Black arrows indicate defects of the sacrum.

2.2. Prosthesis design

2.2.1. Design process

In order to perform the experiments and construct the FE model later, first a prosthesis design had to be made. Implants in the sacrum are mostly necessary for patients with bone tumours who needs Reconstruction of periacetabular defects after pelvic tumor resection. The bone tumour is resected and in many cases the sacroiliac joint and the articulus coxae are removed. Because resection of the tumour and the associated required osteotomy is highly dependent on the size of the tumour, osteotomy and therefore the required implant is very patient specific. First solution for patients with resected sacroiliac joint is the LUMiC 1 ® as shown in figure 2.4. In research prior to this project the anchoring of the LUMiC in the sacrum is retrospectively reviewed in 10 patients. Results were a dislocation in four patients and loosing of the prosthesis in three patients after 28 months. There is concluded that there is a poor clinical result for the LUMiC as sacral fixation [12].

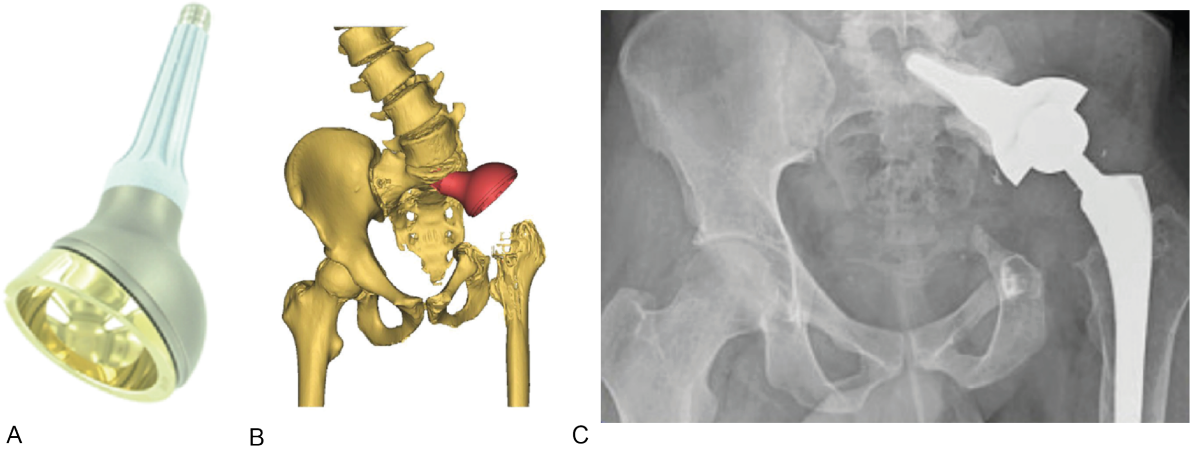

Figure 2.4: The design of the LUMiC 1 ®A: Overview LUMiC 1. B: Model of implantation of LUMiC 1 into the sacrum. C: CT scan of implanted LUMiC 1 into the patient [4].

Dislocation and loosening in patients with the LUMiC 1 led to a re-evaluation of the design. The LUMiC 2 is developed by the LUMC and implantCast (see figure 2.5). The design for the LUMiC2 is only suitable for patients in which the LUMiC 1 loosened and is resected. Because the design of the LUMiC 2 uses the gap that remains after resection of the LUMiC 1. In new patients with bone tumours this gap is not present. Therefore a new design based on the LUMiC 2 but without the part that goes into the gap that is left over from the LUMiC 1 that can function as a connection between the LUMiC cup and the sacrum is necessary. The design for the next LUMiC sacral anchoring part, from now on revered to as the LUMiC 3D, is based on a case study. For this case the patient needed to have an osteotomy in which a large part of the sacrum, because the tumour had infected part IV of the pelvis (see figure 2.6), had to be removed in order to resect the whole bone tumour. Necessary osteotomy is shown in 2.6.

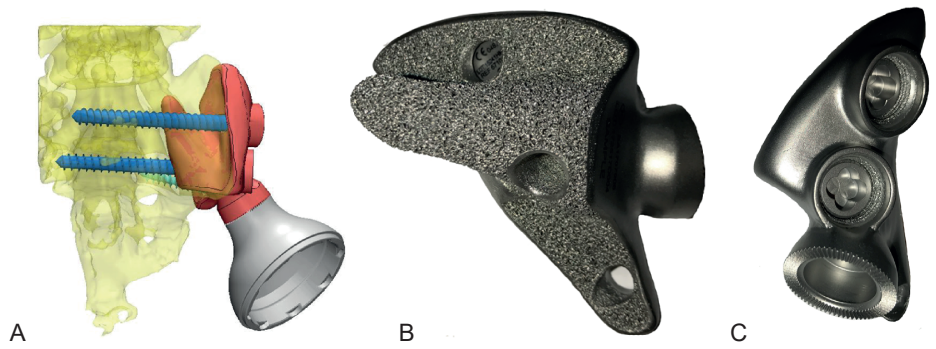

Figure 2.5: Design of the LUMiC 2 ®. In this patient the LUMiC 1 is resected, the created hole after resection is used in the design of the LUMiC 2. A: 3D model of LUMiC 2 implanted in the patient. B: Side view 3D printed LUMiC 2 prosthesis. A porous structure is added at the inner surface of the prosthesis to enable bone ingrowth. C: Front view 3D printed LUMiC 2 prosthesis.

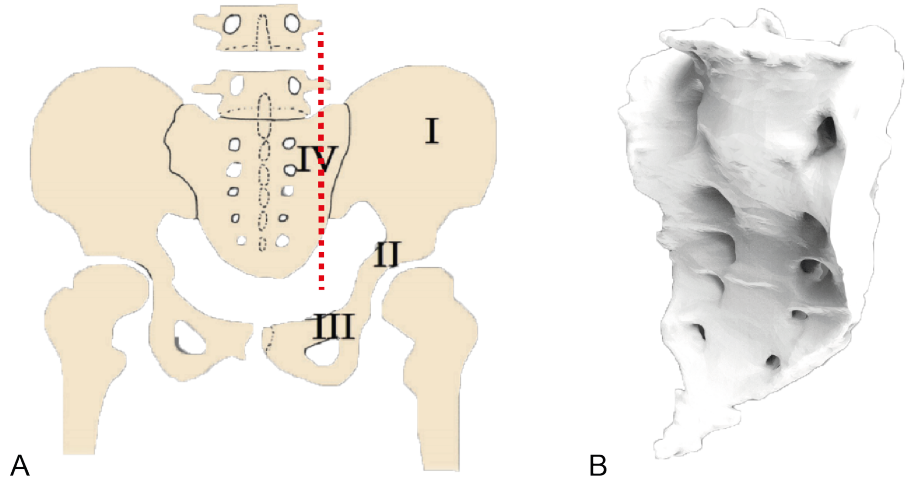

Figure 2.6: A: tumour classification scheme of Enneking et al. (1993) [15]. A subtype IV osteotomy is necessary in this case (indicated by dashed red line). Tumour in case study infiltrated part IV. B: Necessary osteotomy for tumour resection in case study.

The osteotomy as shown in figure 2.6 is taken as a starting point for the prosthesis 3D LUMiC design of this research. The final design had to fulfill following design criteria:

1. Keep foramen of sacrum free because of sacral nerves passing through the foramen.
2. Limit micromotions between prosthesis and bone to ensure primary stability.
3. Limit sharp edges.
4. Counteract the forces while walking as much as possible.
5. Take into account that every surgeon can perform surgery to implant the prosthesis.
6. Place of cup as close as possible to original centre of motion of the hip (COM) without jeopardizing stability of the prosthesis.

Above criteria led to a first mock up model as shown in left part of figure 2.7. ImplantCast used this mock up model to make a first design, with software 3-Matic Medical from Materialize, as shown in figure 2.7.B from now on this design will be referred to as design 1.

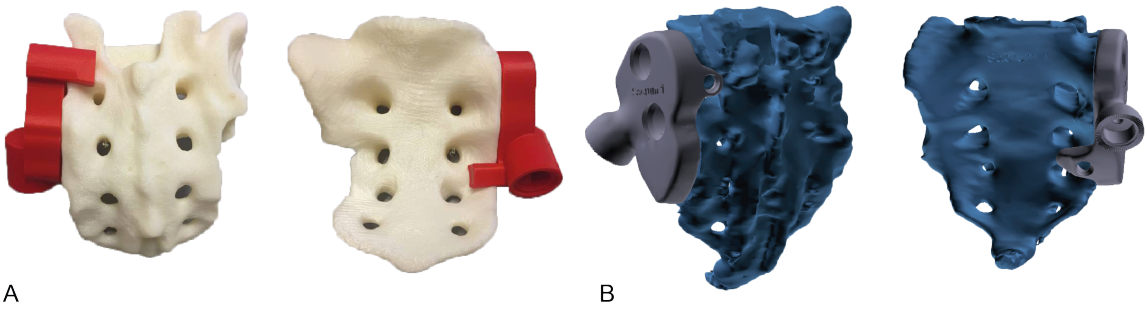

A B

Figure 2.7: A: First mock up model back and front view. B: First design from ImplantCast (design 1) front and back view.

Analysing the forces of the femur on this design will lead to failure of the design, as shown in figure 2.8. The frontal flap acts as a revolute joint leading to rotation of implant as the effect of in plane forces (e.g., F_x). Further development led to design 2 and design 3 as shown in figure 2.9. All design from now on were designed with Solidworks. For design 2 the flanges as shown in figure 2.7 are reversed with the front flange more cranial and the back flanges more caudal compared design 1 of implantCast. Unfortunately, the back flange did not counteract the mechanical force and therefore is useless. Leading to design 3 with two flanges at ventral side. Design 3 is shown in figure 2.9.B. Second adjustment is a bulkier superior ventral flange compared to design 2. Now three different designs were made. The designs are scored for each design criteria systematically by using a Harris profile [54]. The Harris profile for designs 1, 2 and 3 for sacrum 1 are shown in figure 2.10. Design 3 scored best on the Harris profile, therefore design 3 is chosen as the best design strategy.

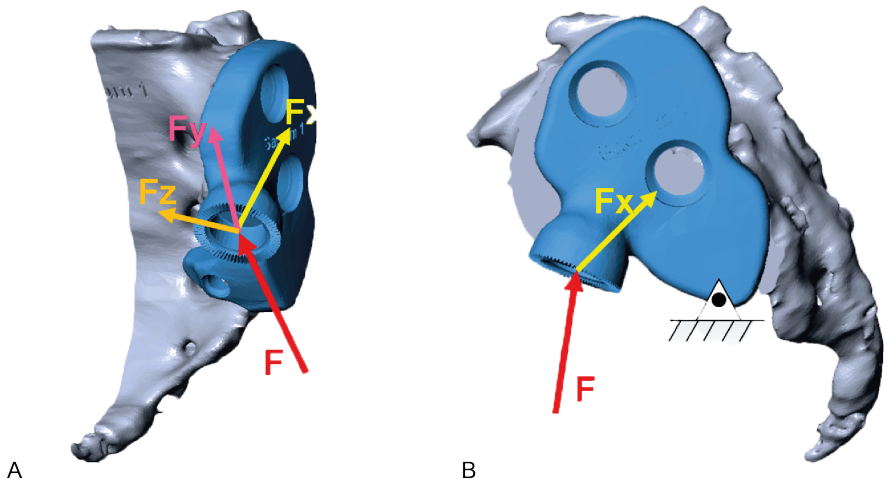

A B

Figure 2.8: Forces on first design of implantCast front view (A) and side view (B). The frontal flap will act as an revolute joint and will lead to rotation of the implant as an effect of Fx.

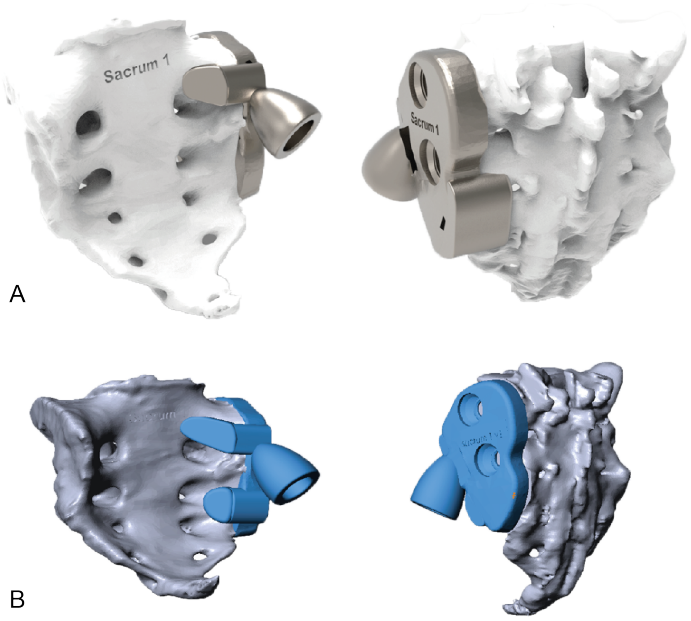

Figure 2.9: A: Design 2. The flanges as shown in figure 2.7 are reversed with the front flange more cranial and the back flanges more caudal compared design 1 of implantCast. B: Design 3. Two flanges at ventral side and bulkier superior ventral flange.

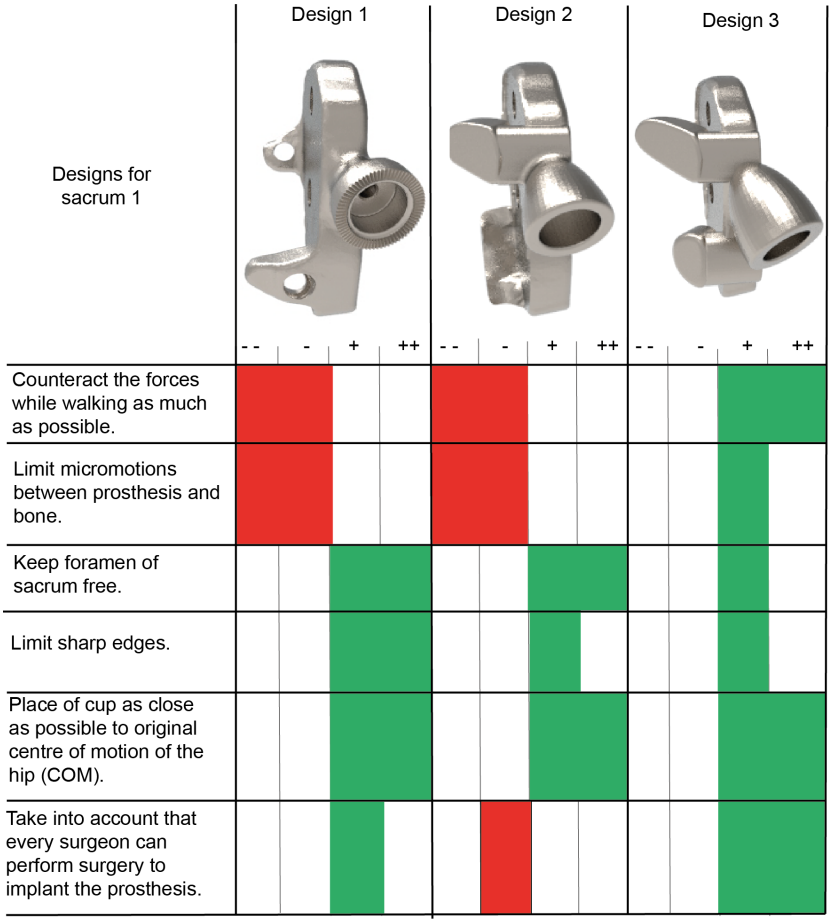

Figure 2.10: Harris profile for design 1, 3 and 3 for sacrum 1. Most important design criteria is listed on top of the list. Design 3 overall scores were the best.

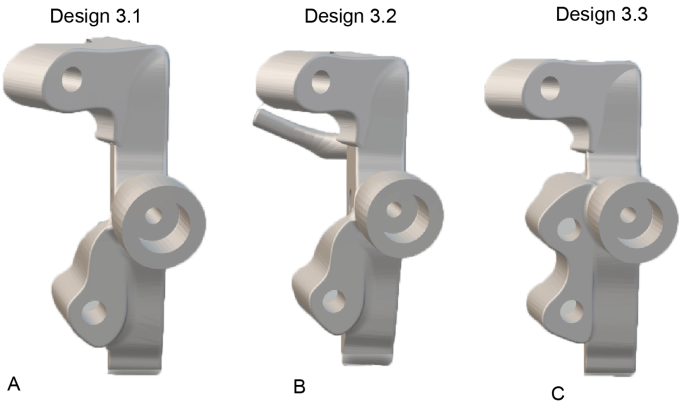

Figure 2.11: Design 3.1 (A) two front flaps in comparison with design 3 of sacrum 1 are created. B: Design 3.2 for sacrum 3. A rod at back side of the sacrum is added in order to enable a screw anchoring at back side of the sacrum. C: Design 3.3 for sacrum 3. Three front flanges give rise to 3 screw anchoring points at frontal side of the sacrum.

Design 1 till 3 are specifically designed for sacrum 1 (as described in chapter 2.1; 3D models of cadaver bone). At the end of chapter 2.1 there was decided to use sacrum 3 as a template because this sacrum is in the best condition. Design 3 as shown in figure 2.9 should be translated to a design specific for sacrum 3. Again three variants of the design were created leading to design 3.1, 3.2 and 3.3. These three variants of designs for sacrum 3 are shown in figure 2.11. Design 3.1 has in accordance with design 3 for sacrum 1 two front flanges. A more extensive overview of design 3.1 including inserted screws and implantation into the sacrum is shown in figure 2.12. In design 3.2 a rod is added at the back side of the sacrum, which makes it possible to insert a screw at the back side of the sacrum. Details of design 3.2 are shown in figure 2.13. Design 3.3 consists out of 3 front flanges, therefore a third place for screw anchoring is possible at frontal side of the sacrum. Design 3.1, 3.2 and 3.3 were again compared in a Harris profile. The Harris profile for design 3.1, 3.2 and 3.3 are shown in figure 2.14. Best scores were achieved for design 3.3.

Figure 2.12: Design 3.1 designed for sacrum 3. A: Overview design 3.1. B: Overview design 3.1 with cup and screws. C: Overview design 3.1 with cup implanted into sacrum 3.

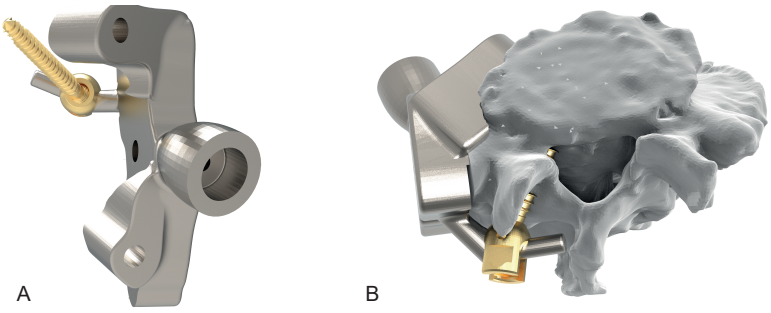

Figure 2.13: Design 3.2 for sacrum 3. At the back side it is possible to insert an pedicle screw into the sacrum. A: Overview design. B: Overview design with implantation into the sacrum.

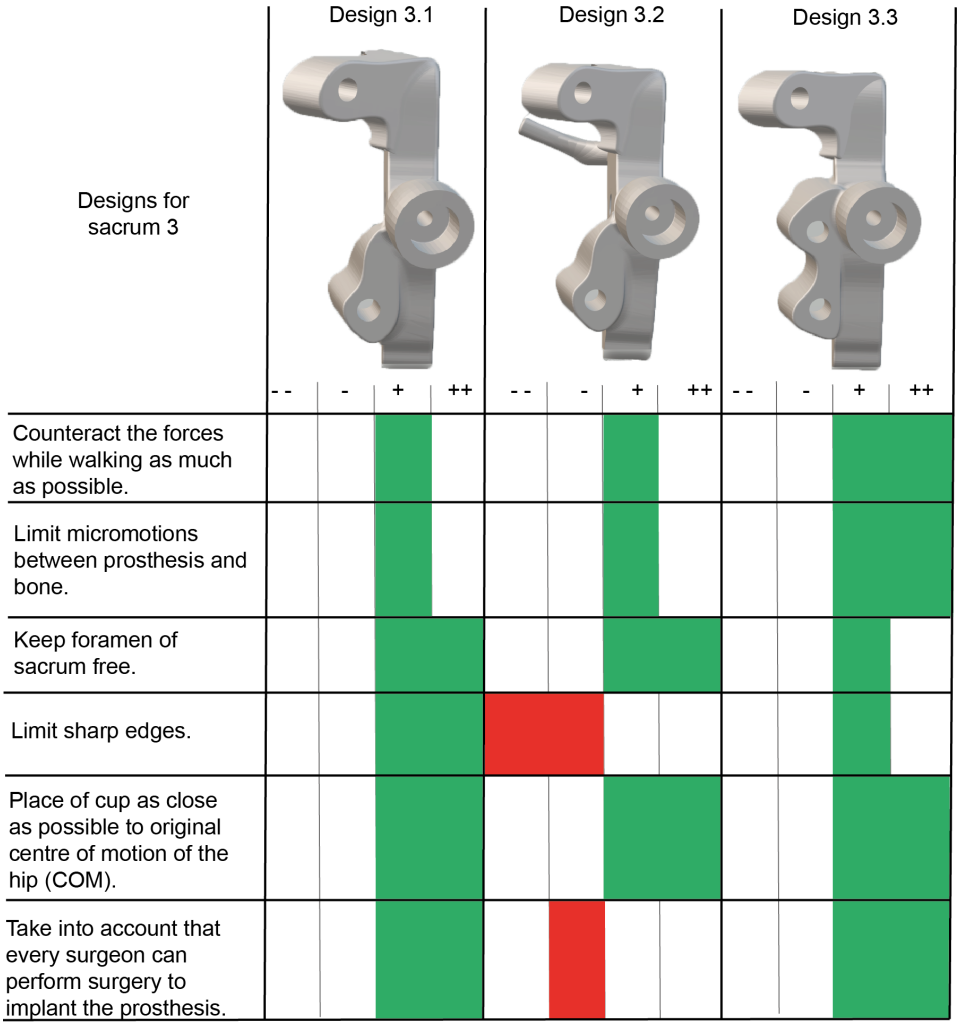

Figure 2.14: Harris profile for design 3.1, 3.2 and 3.3 for sacrum 3. Most important design criteria is listed on top of the list. Design 3 overall scores were the best.

Designs 3.1, 3.2 and 3.3 were all printed with 3D metal printer of TU Delft in order to perform a trial test before the final design is chosen and further developed. The 3D metal printer of the TU Delft is the Realizer SLM-125. In figure 2.15.A the design directly after printing is shown, in figure 2.15.B design

3.1 is shown after detachment of support material. Design 3.3 is used for trial test 1. In trial test 1 the prosthesis was implanted in a 3D printed bone and loaded in an INSTRON E10000 biomechanical testing system until fracture of the prosthesis. Unfortunately in trial test 1 the place were the cup is attached to the prosthesis fractured as shown in figure 2.15.C.

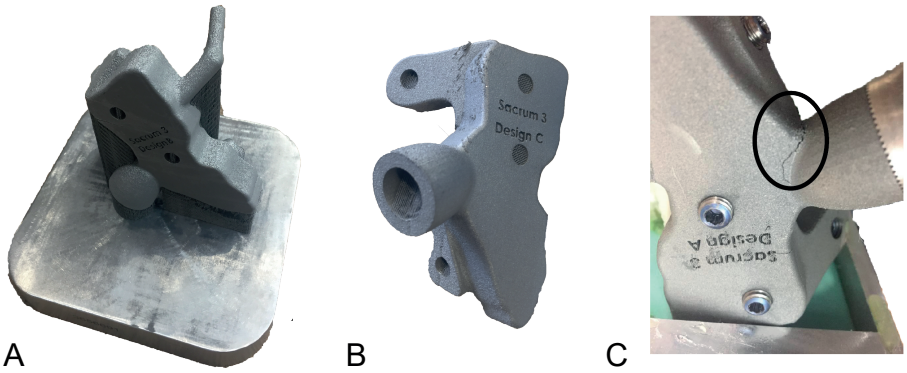

Figure 2.15: A: Design 3.2 directly after printing with TU Delft 3D metal printer. B: Design 3.2 after detachment of support material. C: Fracturing of design 3.3 at place of attachment cup to prosthesis (black circle) during trial test 1.

A simple simulation was used to analyse this fracture. Solidworks is used to do the simulation of design 3.3. The material assigned to the prosthesis is the Titanium alloy Ti-6AL-4V, which is the powder used for 3D printing of the prosthesis at TU Delft. Material properties of Ti-6AL-4V used in Solidworks are:

- Elastic modulus: $1,048 * 10^5\ N/mm^2$
- Poisson's ratio: $0.31\ N/A$
- Shear modulus: $4,1023 * 10^4\ N/mm^2$
- Mass density: $4,428 * 10^3\ kg/m^3$
- Tensile strength: $1050\ N/mm^2$
- Yield strength: $827\ N/mm^2$

The simulation in Solidworks is done by fixating the face of the screws in x,y and z-direction. A force of 500N is applied on the face where cup is attached to prosthesis as shown in figure 2.16.B.

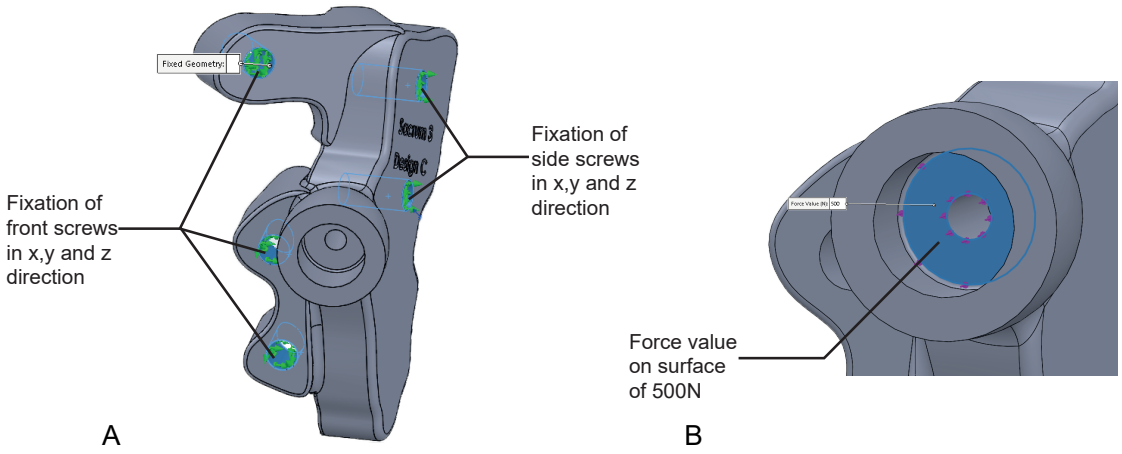

Figure 2.16: A: Representation of the fixation of the screws in the simulation of Solidworks. Surfaces of places of screw insertion are fixed in x,y and z direction. B: Representation of loading condition for the simulation in solidworks. A force value of 500N total is applied at the cup attachement place of the design.

As shown in figure 2.17.B the stress concentrates at the part where the cup is attached to the rest of the prosthesis, but does not exceed the yield strength of the Ti-6Al-4V. It should be noted that the print quality of TU is not yet sufficient. The print was very porous, therefore the real yield strength was probably lower than the strength used in the simulation, because Solidworks assumes a solid prosthesis while the printed material was actually very porous. However, the place of the stress concentration is at the same place as where the prosthesis fractured during the first trial test as shown in figure 2.15.C.

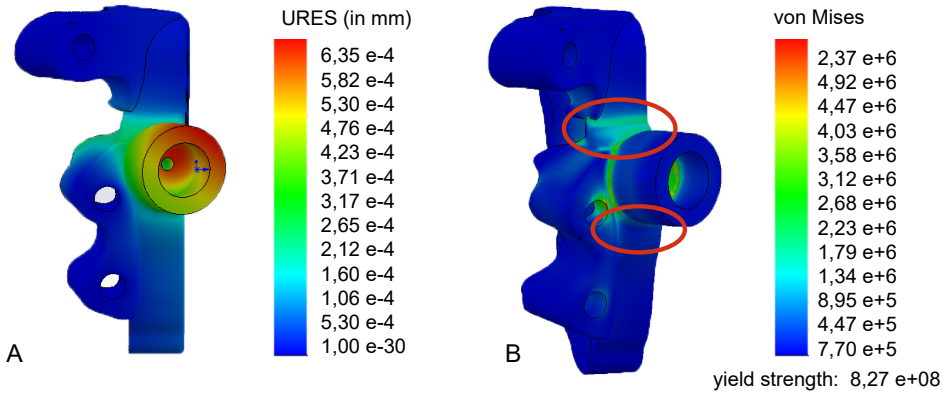

Figure 2.17: Simulation of design 3.3 in Solidworks. Results for deformation (A) and von Mises stresses (B) are shown. There are large stress concentrations at the place where the cup is attached to the prosthesis (red circles).

Therefore, in design B (figure 2.18.A) more material is added at this place to prevent this fracture. Furthermore, the edges are made more smooth to fulfill design criteria 3 better. In figure 2.18.B and 2.18.C the simulation results for design B are showed. It should be noted that although the stress concentration at the bottom place of cup attachment is lower , the overall stress is higher and stress still concentrates at point of attachment of cup.

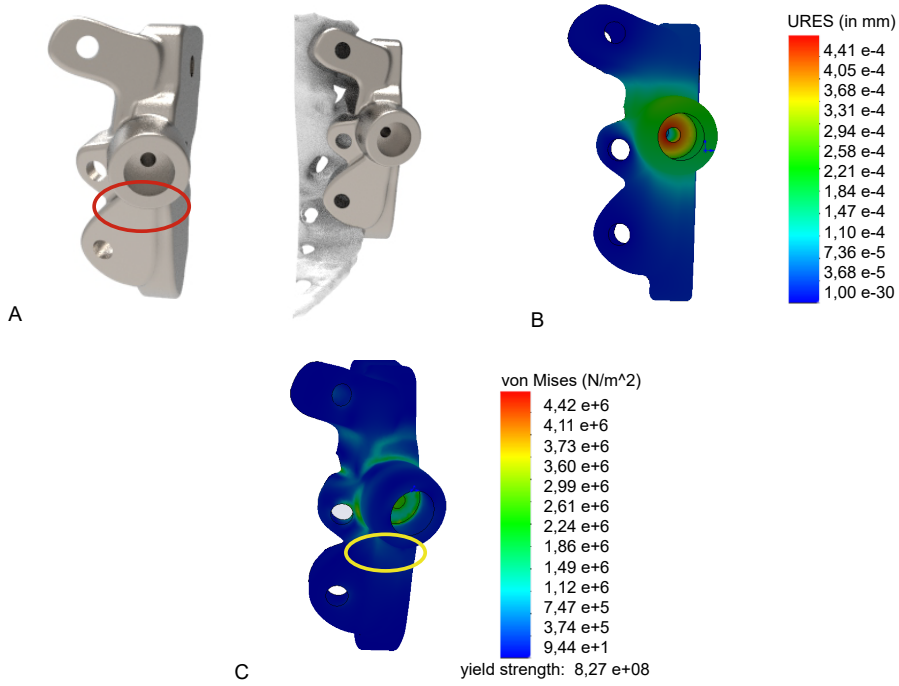

Figure 2.18: Design B for sacrum 3. Edges are made more smooth and more material is added at cup attachment (red circle) especially at place were prosthesis broke in trial test 1 as is shown in figure 2.15.C. In 2.18.B-C simulation of design B is shown. Stress still concentrates at place of cup attachment (yellow circle).

Because stress still concentrated at place of cup attachment in design C (figure 2.19.A) there is even more material added at the point of attachment of the cup. As shown in figure 2.19.C the stress concentrations in this design were lower. Although the stress concentrations in design C were very low another problem with the design arose. The two cranial screws as shown in figure 2.19.A are at the point, that is marked with a yellow circle, to close to each other. Distance between both screws at this point is $0.18\,mm$. When screws are so close to each other potentially there is no bone space between the screws leading to one big corridor which is not beneficial for the strength of the screw anchoring to bone.

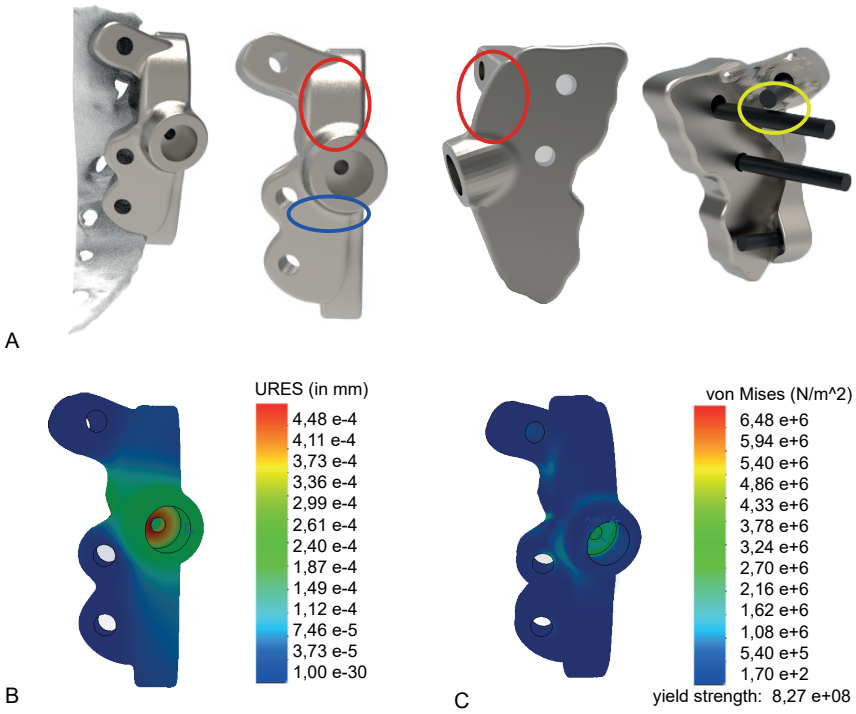

Figure 2.19: Design C. Even more material at places of stress concentration (red circles in 2.19.A) and smoother edges (blue circle in 2.19.A). Problem with this design is the two cranial screws. The distance between this screws at the point of the yellow circle is 0.18mm. C: Stress concentrations are lower then in design B (figure 2.18.C-D).

Above screw problem led to design D. More space between the screws is created. space between cranial screws is now $5,43\,mm$, space between middle screws is $6,94\,mm$. Moreover, the direction of the screws is changed. The cranial and middle front screw are now in the same direction as the force on the cup to maximal counteract the traction forces. The distance between screws is shown in the yellow circles in figure 2.20.A, the direction of the screws is indicated by the blue arrows in the same figure. In figure 2.18.C the stress on design D is shown. It should be noticed that the stress is comparable with the stress measured in design C.

Furthermore, it should be mentioned that the inner surface of the prosthesis design will be porous. As is explained in chapter 1.4 an important requirement for the mechanical stability of implants is the possibility of bone ingrowth into the prosthesis. Adding of microstructures on the surface of the model will be used to create a porous structure during metal printing of the implant. This porous structure will have a pore size between 100 and 400 μm as is described by the research of Kienapfel et al. (1999) [31]. Furthermore, the two side screws will be locking screws, meaning the screw head is screwed entirely into the design. This is done to counteract the shear forces on the design. The concept of locking screws will be explained below in chapter 2.2.2.

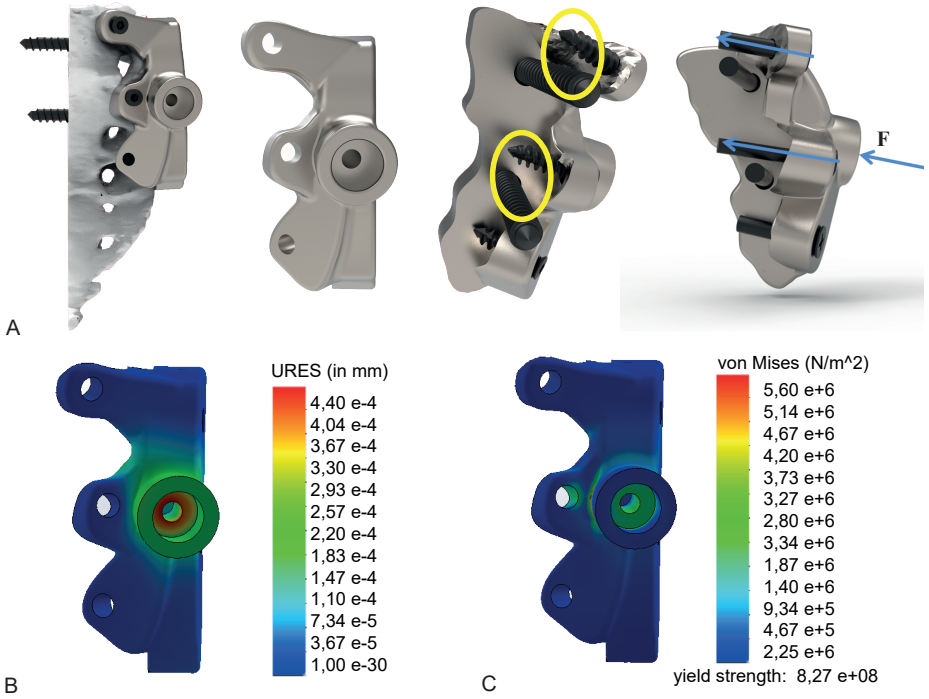

Figure 2.20: Design D. A: overview design D. yellow circles indicated distance between screws, blue arrows indicate direction of the screws. B: Displacement of design D. Displacement is lower than in design C. C: Stress of design D. Stress is lower than in design C.

Eventually the final design is send to implantCast. ImplantCast made some small adjustments by smoothing the edges of the design and made the design suitable for 3D metal printing. The adjustments of implantCast are shown in figure 2.21.A. Finally, the design is 3D metal printed at implantCast by using the material Ti4Al6V, which is the same material as used in the solidWorks simulations above. The printed final design is shown in figure 2.21.B and figure 2.21.C. The design is now available for experiments. The performed experiments are explained in chapter 2.6.

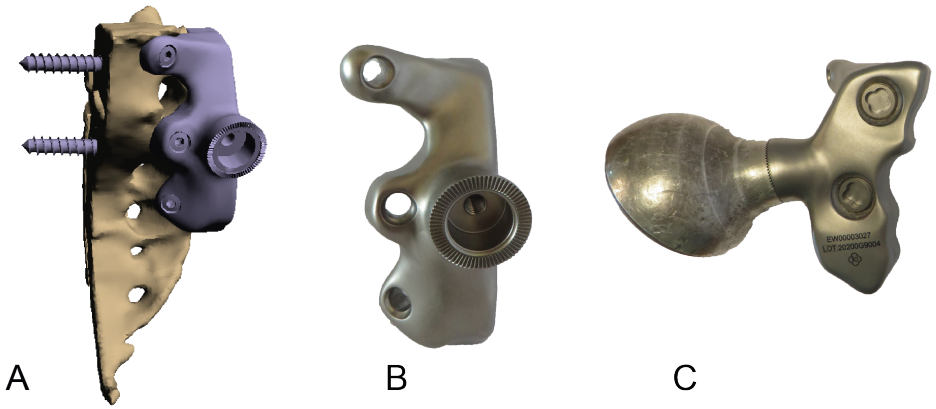

Figure 2.21: Adjustments made to design D by implantCast. A: Overview of adjustments made by implantCast in which the edges are made smoother. B: 3D printed final design. C: 3D printed final design with cup attached to design.

2.2.2. The concept of locking screws

In the design of the prosthesis the used screws are designed as locking screws, meaning that the screw head is locked in the prosthesis by screwing it in a threaded chamber on the prosthesis itself (see figure 2.22). Locking screws are usually used in bone plates, to fix for instance a broken collar bone.

In locking plates two categories are predominant: fixed-angle locking plates and variable-angle locking plates, which the screw can be locked with a clearance enabling the screw direction to vary between 1-15◦. The way of locking the screw into the plate also comes in two types. The screw head can be locked in its chamber by a threaded locknut or the screw head itself is threaded and can be screwed into the plate or a adapted lip. In our design the threaded locknut is used.

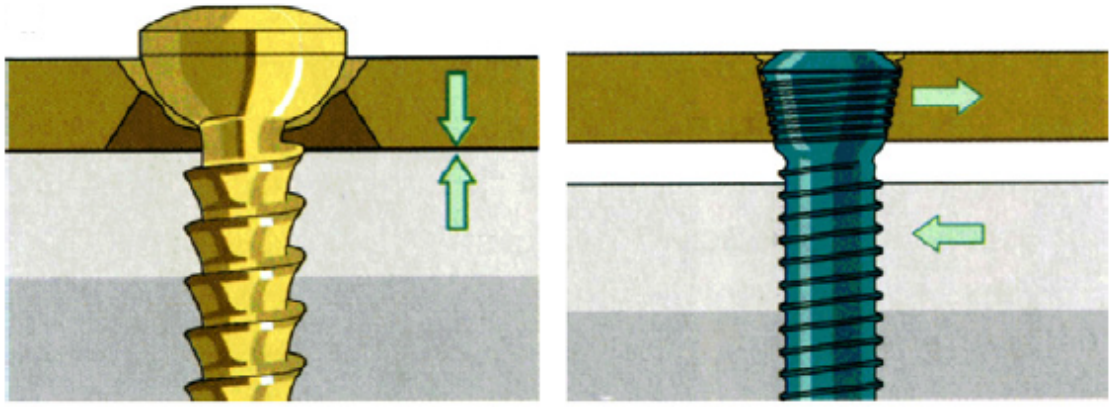

Figure 2.22: Representation of a normal screw (left) and a locking screw (right) [9]

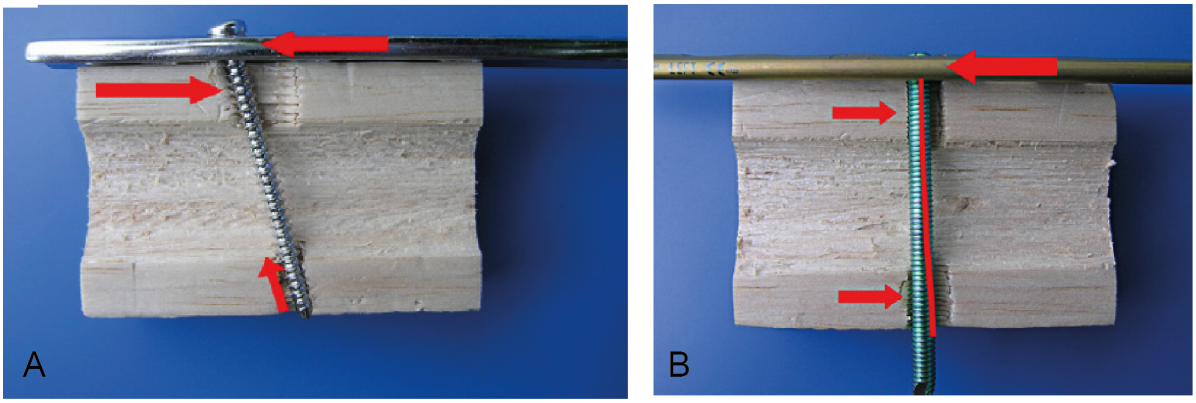

Figure 2.23: Comparison of the effect of shear to a normal screw (A) and a locking screw (B). A locking screw resist shear along its entire length [9]

2.3. Loading scheme

In order to mechanical test the designed prosthesis part of chapter 2.2 a loading strategy is determined. This loading strategy is especially of great importance because it determines the alignment of the bone in the force tensile machine. After the determination of the loading scheme for the experiments, the same loading scheme is copied to the FE model in order to make sure both parts can be compared later on. Therefore, to define the loading of the FE model but also for the loading of mechanical bone models the same strategy is used. This chapter will elaborate on the determination of this loading scheme.

First the standardized loads that act on normal total hip replacements from the study of Bergmann et al. (2016) [3] are evaluated. Preferable the loading condition would be based on loads acting on a LUMiC prosthesis that is inserted into the pelvis. Unfortunately there is no data available yet on this topic. Therefore, standard loads are used and transformed to fit the loading condition of the newly designed prosthesis of chapter 2.2 as much as possible. The strategy used to define the loading condition is clarified in this chapter starting with a description of the research of Bergmann et al. (2016) [3].

2.3.1. Standardized loads acting in hip implants

Although new finite element modelling (FME) techniques are available, still pre-clinical endurance tests are the golden standard in mechanically evaluating new implant designs. Endurance tests for biomechanically evaluating new implant designs are described in the ISO7206-4 standard. For example the loading scheme for the hip stem is determined as a sinusoidal force of 2300 N applied under angles of 10 $\deg$. These load directions and magnitudes were based on historic calculations of contact forces in the hip. New techniques are now possible in which the hip implant is modified to measure forces providing real in-vivo data of contact forces in the hip. In the research of Bergmann et al. (2016) [3] this modified hip was used and therefore the ISO standards were revised and updated. In this study of Bergmann et al. (2016) [3] in 10 subjects that underwent total hip replacement, loads on the hip were measured during the most frequent activities of daily live. Activities were walking, stair climbing and descending, sitting down or standing up and standing on one leg. The implant was modified with six strain gauges to measure the forces during above described activities. The system was able to real-time monitor the 3D forces and moments with an accuracy of 1-2%. Measured forces were contact forces components F_x, F_y and F_z in Newton and the three moment components M_x, M_y and M_z. Resultant force F_{res} and resultant moment M_{res} were calculated by summation of the components. In table 2.2 an overview of the results of the research of Bergmann et al. (2016) for walking are shown. In this thesis all the data measured by Bergmann et al. (2016) is accessed and used in order to define the least favorable load on the implant during one walking cycle. The least favorable load is chosen with the thought that if the new implants holds when loaded with this least favorable load it is strong enough to hold during less burdensome parts of the walking cycle. The details on the precise determination of the least favorable load during one walking cycle are described below in chapter 2.3.3.

Table 2.2: An overview of the data of Bergmann et al. (2016) [3] for a subject of 75 kg.

Forces (N)	Max Fres walking	1853.28 N
	Min Fres walking	231.87 N
	Average Fres walking	1053.36 N
Moments (Nm)	Min Mx	-0.825 Nm
	Max Mx	0.950 Nm
	Min My	-0.242 Nm
	Max My	0.783 Nm
	Min Mz	-0.325
	Min Mz	0.408
Angles force vector F for Fres is max (°)	α_{front} (frontal plane) z –> x	17 °
	α_{sagit} (sagittal plane) z –> y	11 °
	α_{trans} (transverse plane) y –> x	33 °

2.3.2. Angles in the hip

Besides normal loading on the hip during a walking cycle, also a consensus on standardized angles in the hip had to be achieved. In this part the data of vialle et al. (2005) [56] is used to explain the standardized angles on the pelvis region.

On a lateral radiograph of the pelvic girdle three parameters for orientation of the hip bones can be measured. The sacral slope is the angle between a horizontal line and the tangent of the cranial sacral end plate. The pelvic tilt is the angle between the vertical line and a line from the middle of the sacral endplate to the center of the bicoxofemoral axis. The bicoxofemoral axis is a line between the geometric center of both femoral heads.Finally, the pelvic incidence which is the angle between the line perpendicular to the middle of the cranial sacral end plate and the line from the middle of the sacral and plate to the center of the bicoxofemoral axis. The mean angles measured in the research of Vialle et al. (2005) [56] are shown in table 2.3.

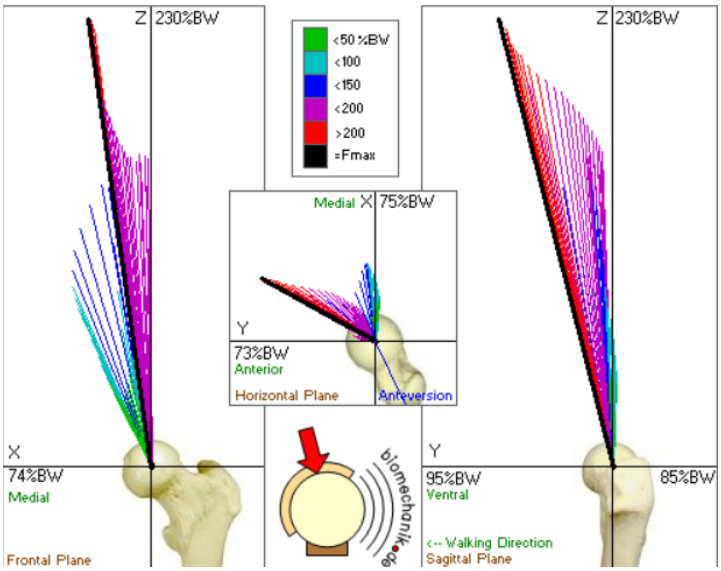

Figure 2.24: Forces on the hip from one patient of the research of Bergmann et al. (2016) [3].

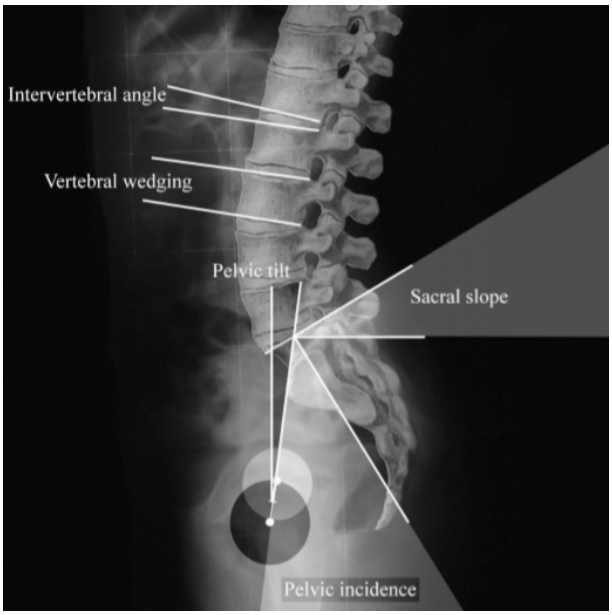

Figure 2.25: Parameters measured in lateral radiographs of the pelvic girdle in the research of Vialle et al. (2005) [56]

Table 2.3: Angles measured in the research of Vialle et al. (2005) [56] in radiographs of patient in standing position.

	mean (deg)	**95% confidence interval (deg)**
sacral slope	41,2	40,91-42,.81
pelvic incidence	54,70	53,46-55,88
pelvic tilt	13,2	12,52-13,90

To align the test setup the angles as described in table 2.3 are used. Few steps were taken to determine the loading scheme used for testing. The orientation of the sacrum and femur in the test set up are determined as following:

2.3.3. Define loading scheme

The described information about standard loads in the hip in chapter 2.3.1 and about standard angles in the hip of chapter 2.3.2 is used to determine a loading scheme for the FE model of part 1 of the thesis and the experiments of part 2 of the thesis. The loading scheme is the same for both parts so that the results of both parts can be compared in future research.

Step 1: make standard model of the hip

A standard 3d model of the hip is made in Materialise 3-matic Medical version 21.0 with angles in the hip as described in table 2.3. The model is shown in figure 2.26 and figure 2.27.

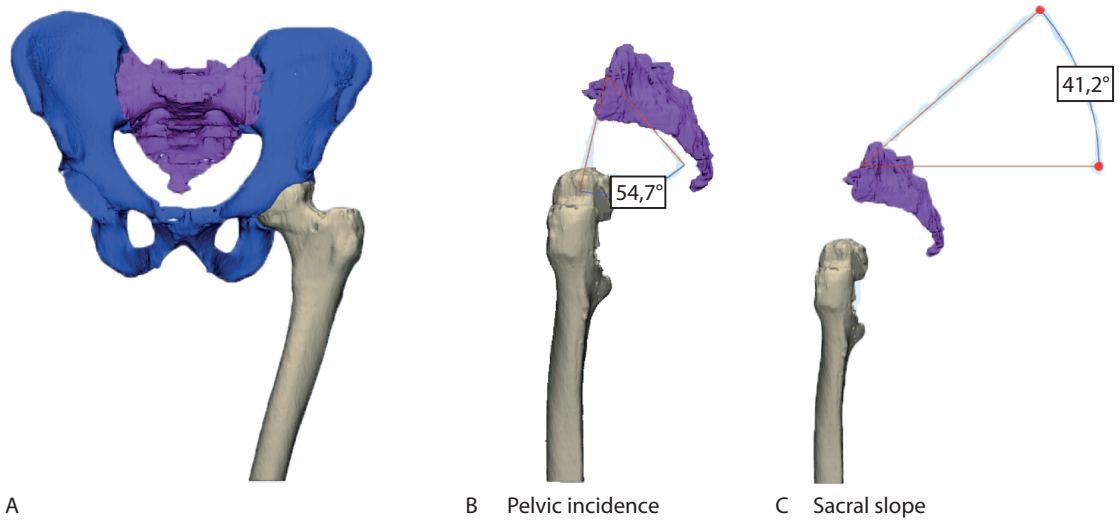

Figure 2.26: Representation of step 1: make standard model of the hip. A: Overview orientation of the hip. B: Pelvic incidence of 54,7°. C: Sacral slope of 41,2°.

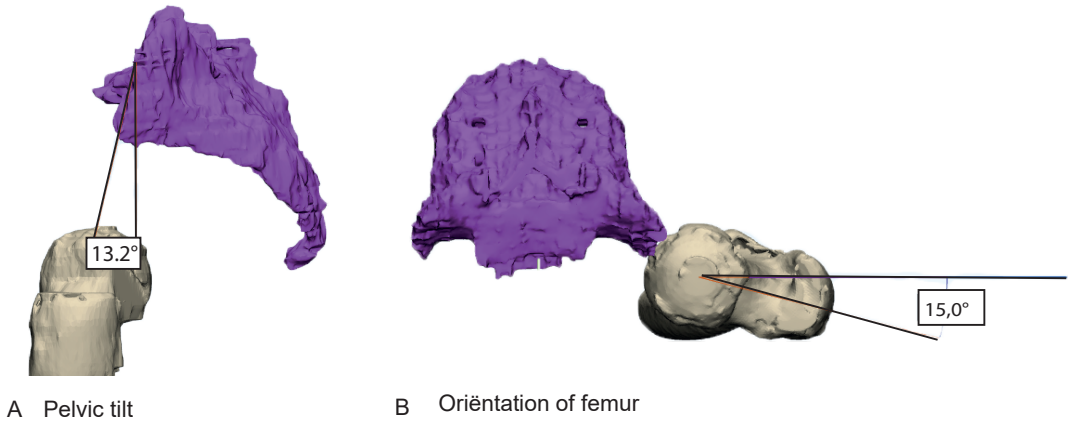

Figure 2.27: Step 1: Standard model of the hip. A: pelvic tilt of 13,2°. B: Orientation of femur (15° of horizontal line).

Step 2:insert sacrum with implanted new LUMiC design in model of step 1

The made 3D model of the cadaver sacra with the designed prosthesis implanted is pasted into the standard model of step 1 with same orientation of sacrum as in the standard model of step 1 (see figure 2.28).

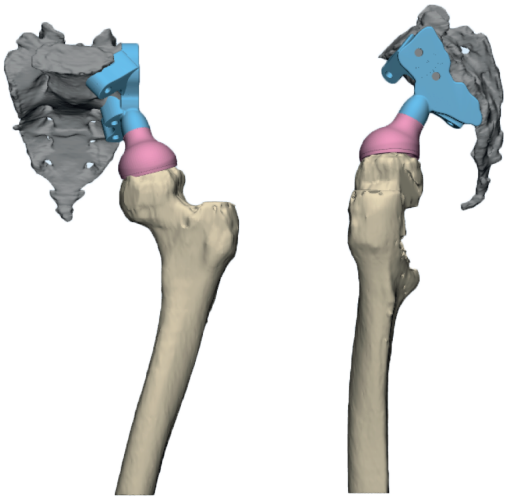

Figure 2.28: Model of hip of step 2 with prosthesis front and side view.

Step 3: determine pivot points

In the model of step 2 three pivot points on the prosthesis are determined. The chosen pivot points are named respectively high-, middle- and low point prosthesis. The pivotpoints are shown in figure 2.29

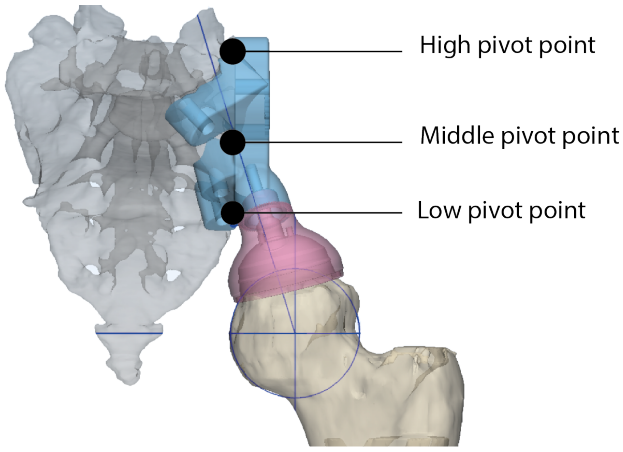

Figure 2.29: Overview of high-, middle- and low pivot point on the prosthesis.

Step 4: Calculate moments

The moments around pivot points high-, middle- and low point prosthesis for all forces in one walking cycle described by Bergmann et al. (2016) [3] are calculated. The calculations are shown in figure 2.30. The moments are calculated by the following equations:

$$Mx = Fz \bullet dx + Fx \bullet dz \tag{2.1}$$

$$Mz = Fy \bullet dx + Fx \bullet dy \tag{2.2}$$

$$Mx = Fz \bullet dy + Fy \bullet dz \tag{2.3}$$

$$M = \sqrt{Mx^2 + My^2 + Mz^2} \tag{2.4}$$

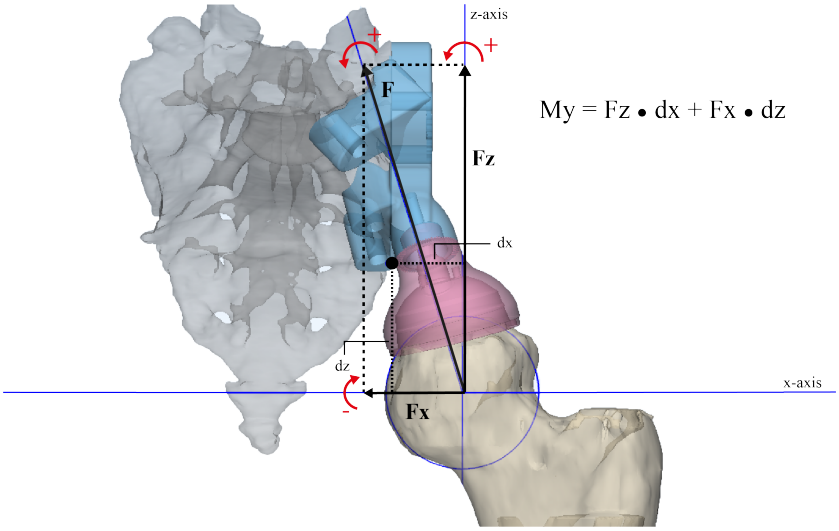

(a) Moment around y-axis.

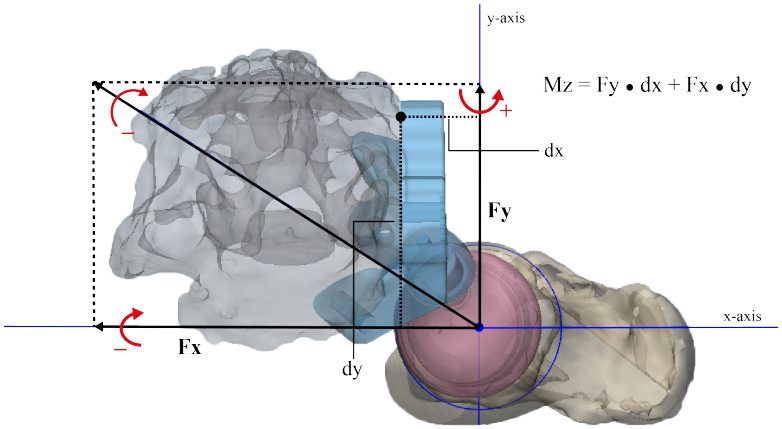

(b) Moment around z-axis.

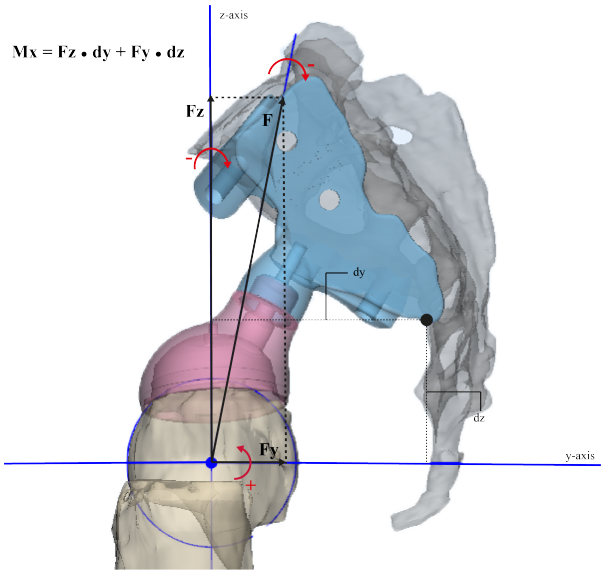

(c) Moment around x-axis.

Figure 2.30: Calculation of moments. A: calculation of moment around y-axis. B: calculation of moment around the z-axis. C: calculation of moment around the x-axis.

Step 5: Determine most unfavorable moment on prosthesis

An overview of the calculated moments of step 4 are shown in tables 2.4, 2.5 and 2.6. The most unfavorable moment was found for calculating the moments for the pivot point at the low point of the prosthesis with $Fx = -730.6$ N, $Fy = 6.92$ N and $Fz = 2706.11$ N. These forces are used in the FE model and for the test set up. For more information about the use of this force in the FE model see chapter 2.4 and for information about the test set up chapter 2.6.

Table 2.4: Calculated moments with pivot point at low point prosthesis. Chosen force vector for test set up is bold.

	index number	Mres (in Nm)		M (in Nm)	Fres (in N)		F (in N)
max M (in Nm)	280	206.0790	Mx	-195.5404	2802.0756	Fx	-773.8100
			My	37.7345		Fy	4.5100
			Mz	-52.9972		Fz	2704.2800
max Mx (in Nm)	**281**	**206.0558**	**Mx**	**195.5567**	**2803.0083**	**Fx**	**-730.6000**
			My	**37.9383**		**Fy**	**6.9200**
			Mz	**-52.6997**		**Fz**	**2706.1100**
max My (in Nm)	300	197.6628	Mx	-188.1638	2728.0096	Fx	-654.5800
			My	40.0079		Fy	72.1500
			Mz	-45.4351		Fz	1647.3300
max Mz (in Nm)	246	193.3708	Mx	-182.2164	2629.5251	Fx	-788.8000
			My	29.7986		Fy	-13.2900
			Mz	-57.4585		Fz	2508.3900
max Fres (in N)	93	179.5654	Mx	-170.4381	2880.8654	Fx	-830.0700
			My	33.1818		Fy	530.6600
			Mz	-45.7553		Fz	2707.1700

Table 2.5: Calculated moments with pivot point at middle point prosthesis.

	index number	Mres (in Nm)		M (in Nm)	Fres (in N)		F (in N)
max M (in Nm)	272	73.2592	Mx	-69.7850	2779.5809	Fx	-755.9400
			My	10.2937		Fy	-13.3000
			Mz	-19.7737		Fz	2674.8000
max Mx (in Nm)	272	73.2592	Mx	-69.7850	2779.5809	Fx	-755.9400
			My	10.2937		Fy	-13.3000
			Mz	-19.7737		Fz	2674.8000
max My (in Nm)	310	59.6657	Mx	-55.2427	2594.0592	Fx	-601.6200
			My	18.8757		Fy	114.5300
			Mz	-12.3271		Fz	2520.7300
max Mz (in Nm)	246	68.7464	Mx	-65.5116	2695.2513	Fx	-788.800
			My	3.0375		Fy	-13.2900
			Mz	-20.6172		Fz	2508.3900
max Fres (in N)	93	179.5654	Mx	-170.4381	2880.8654	Fx	-830.0700
			My	33.1818		Fy	530.6600
			Mz	-45.7553		Fz	2707.1700

Table 2.6: Calculated moments with pivot point at high point prosthesis.

	index number	Mres (in Nm)		M (in Nm)	Fres (in N)		F (in N)
max M (in Nm)	262	62.3009	Mx	-57.7417	2723.0061	Fx	-772.2200
			My	-16.1496		Fy	-24.4000
			Mz	-16.9259		Fz	2611.100
max Mx (in Nm)	266	62.1479	Mx	-57.9969	2750.4643	Fx	-767.1500
			My	-14.7955		Fy	-20.9500
			Mz	-16.7279		Fz	2641.2300
max My (in Nm)	317	17.3782	Mx	-16.9022	2445.7865	Fx	-560.8200
			My	-0.4404		Fy	141.6900
			Mz	-4.0151		Fz	2376.4000
max Mz (in Nm)	246	60.5849	Mx	-54.3520	2629.5251	Fx	-788.8000
			My	-20.6882		Fy	-13.2900
			Mz	-16.9822		Fz	2508.3900
max Fres (in N)	93	179.5654	Mx	-170.4381	2880.8654	Fx	-830.0700
			My	33.1818		Fy	530.6600
			Mz	-45.7553		Fz	2707.1700

2.4. Simulation

To predict the micromotions that appear between implant and bone and the stresses that occur in the prosthesis a Finite element model was made. Goal of the finite element model is that it can be used to evaluate future prosthesis designs. Furthermore, a comparable FE model will be made with the old LUMiC inserted. Micromotions and stresses with the old LUMiC will be compared with micromotions and stresses with the new LUMiC 3D design of chapter 2.2. The placement of the old LUMiC is done in consultation with an orthopaedic surgeon. Furthermore, the three front screw of the prosthesis design will be deleted from the model and micromotions between implant and bone will be evaluated again. More on evaluating the micromotions in chapter 2.4.6. To conclude, 3 FEM models will be made:

1. Model 1: Sacrum and old LUMiC.
2. Model 2: Sacrum and new 3D LUMiC part with 5 inserted screws.
3. Model 3: Sacrum and new 3D LUMiC part with only 2 side screws inserted.

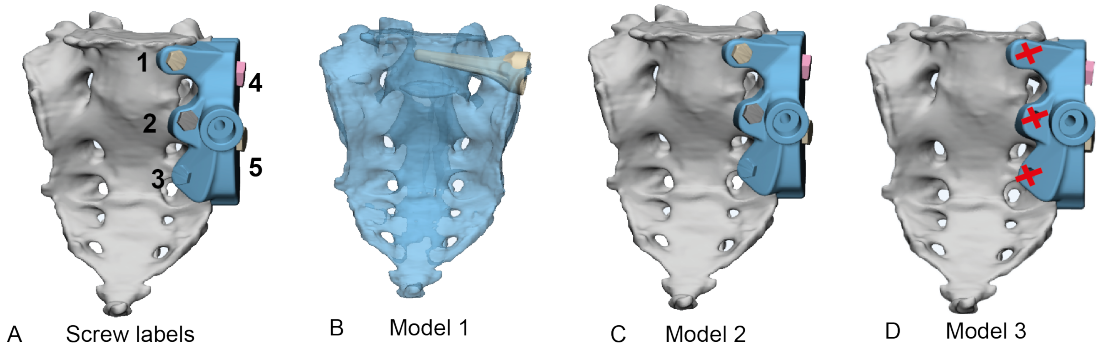

Figure 2.31: Screw numbering and overview of the 3 FE models. Red crosses indicates eliminated screws.

2.4.1. Creating non manifold assembly

A non manifold assembly is used to prepare the input file for abaqus with an orphan mesh of the model. In a non manifold assembly the surface of interaction of all parts are described.

1. Create 3-matic files with imported stl files of sacrum, lumic and pins.
2. Create non-manifold assembly in 3-matic grid based, grid of 0.5.
3. Use uniform mesh.
4. Delete intersection triangles with the fix module of 3-matic.
5. Create volume mesh of non manifold assembly.
6. Split non-manifold assembly by volume.
7. Rename created volumes.
8. Export volumes to Mimics.
9. Assign material to sacrum bone in mimics as in chapter 2.4.2.
10. Export created mesh to Abaqus.

2.4.2. Assigning material properties to the sacrum bone

First step of the FEM model is to assign material properties to different sections of the sacrum bone. First the CT scan DICOM images were transferred to the mimics Medical 21.0 software and segmented to form a 3D model of the sacrum as described in chapter 2.1. This 3D model had to be meshed. To perform meshing the model is exported to 3-matic medical 13.0 software. The 3-matic option autofix was used to fix small defects in the 3D model. Further, a uniform mesh with a target triangle edge length set to 1 and the number of iterations also set to 1 is assigned to the sacrum bone. Hereafter, a volume mesh with element type Tet4 (4 nodes tetrahedral) is created (see figure 2.34). Hereafter, the volume mesh of the sacrum is imported back to the mimics medical 21.0 software. In

mimics the material is assigned based on the gray value of the CT data. The following equations are used in literature to assign the material properties [25]:

$$\rho = 6.9141e^{-4}HU_{real} + 1.026716 \tag{2.5}$$

$$E = 2017.3\rho^{2.46} \tag{2.6}$$

The sacra were scanned together with a phantom which contained three bars of which the hounsfield units were known. The phantom is showed in figure 2.32a and contained known hounsfield units 200 HU, 0 HU and 100 HU. When evaluating the CT scans HU units at this phantom did not correspond, but where respectively 265.93, 6.96 an 139.02 (as shown in figure 2.32b). These points were plotted and a line is fit to the data as shown in figure 2.33 with equation:

$$HU_{measured} = 1.2948HU_{real} + 7.8183 \tag{2.7}$$

Equation 2.7 is substituted in equation 2.8 en rewrited to fit the model. This resulted in the following equations to assign material properties in the model:

$$\rho = 5.33989e^{-4}HU + 1.022585 \tag{2.8}$$

$$E = 2017.3\rho^{2.46} \tag{2.9}$$

(a)

(b)

Figure 2.32: (a) Known HU values of the phantom. (b) Real measured HU values in mimics.

Equations 2.8 and 2.9 are used in mimics to assign the material properties of the bone based on the gray values of the bone. For trabecular bone the Poisson's ratio (μ) were set to 0.2 and for cortical bone to 0.3 in accordance to the paper of Zhao et al. (2016) [66]. A representation of the different material properties assigned to the sacrum bone is shown in figure 2.34. The material properties used are shown in table 2.7.

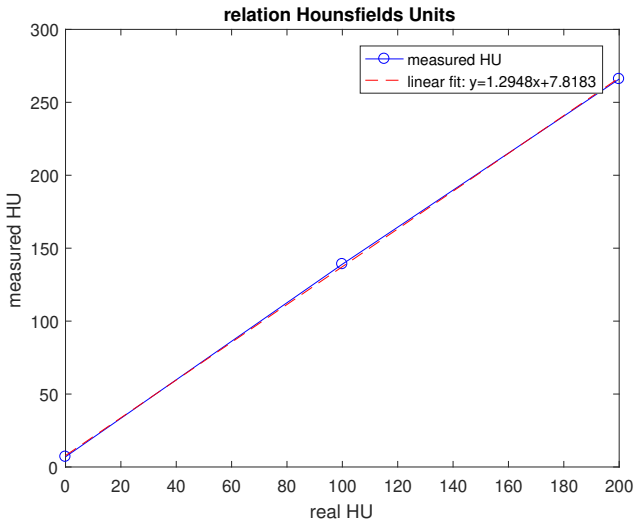

Figure 2.33: Comparison of measured HU and known HU from phantom (real HU). A linear fit is used to determine the define equation 2.9 and 2.8.

Table 2.7: The assigned material properties of the bone by the gray value based method of mimics and the assigned material properties for the Ti6AL4V (LUMiC and screws)[25].

Material	ρ (g/cm^3)	E (MPa)	ν
Bone material 1	0.539637	442.324	0.2
Bone material 2	0.69871	853.104	0.2
Bone material 3	0.857782	1383.18	0.2
Bone material 4	1.01686	2101.98	0.2
Bone material 5	1.17593	3005.43	0.2
Bone material 6	1.335	4106.34	0.3
Bone material 7	1.49407	5416.59	0.3
Bone material 8	1.65315	6947.3	0.3
Bone material 9	1.81222	8709.01	0.3
Bone material 10	1.97129	10711.7	0.3
Ti6AL4V		110000	0.3

2.4.3. Interations and tie constraints

Abaqus/CAE does not recognize mechanical contact between the parts in the assembly without contact specification in the interaction module, therefore a general contact is created between the LUMiC and the bone, pins and bone and pins and lumic in the initial step. Friction between surfaces is set to friction with friction coefficient of 0.3 as is done in papers of ji et al. (2010) [29] and Iqbal et al. (2017) [25]. A second step is created called apply load. In the this second step a tie constraint between all screws and the LUMiC is defined too.

To simulate the interaction between the screws and the bone a undersized pilot hole is used in the bone. This is done by the example of the paper of Macleod et al. (2012) [37]. The undersized pilot hole resulted in a tighter fit for the screws into the bone. A thermal expansion is applied to all screws after insertion. The screws are sectioned in a section that is in contact to the bone and a section that is in contact to the LUMiC. The material of the section that is in contact to the bone is assigned with an anisotropic thermal expansion coefficient. The thermal expansion coefficients that correspond with shear expansion and axial lengthening were set to zero. The thermal expansion coefficients that were corresponding with radial expansion of the screws were set to 0.01. Meaning that when there is an increase in temperature of 1% this corresponds to an expansion of 1 %. Afterwards, the model was set to an increase in temperature of 1 %, resulting in an expansion of all screws to 1 %. The expansion of

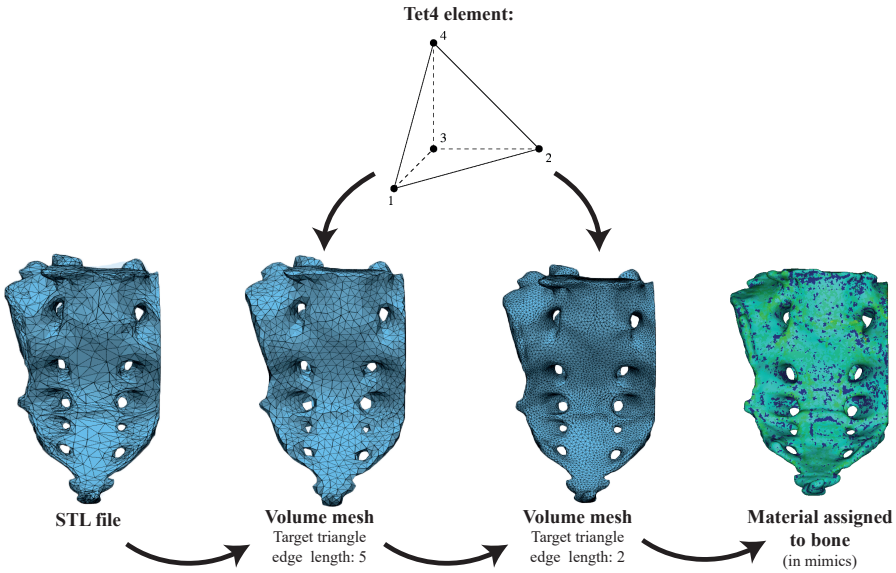

Figure 2.34: Fitting of line through measured HU values and real HU values.

two screws is shown in figure 2.35.

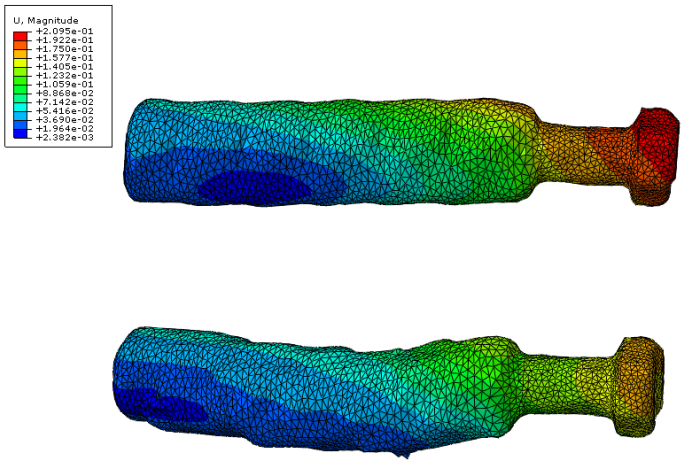

Figure 2.35: Exaggerated representation of the expansions of two screws. The screw is sectioned in a part that is in contact with the bone and allowed to expand and a section that is in contact with the prosthesis and is not allowed to expand.

A boundary condition for the surface of half of the sacrum is set to encastre (U1 = U2 = U3 = UR1 = UR2 = UR3 = 0). The nodes of half of the sacrum are fixed in all direction in this boundary condition. The boundary condition in shown in figure 2.36a

2.4.4. Define loading condition

In the step apply load the model is loaded at the interface of where normally the cup is attached to the lumic. This surface consists of 184 nodes. The total load on this part was determined in chapter 2.3 as $Fx = -730.6$ N, $Fy = 6.9$ N and $Fz = 2706.11$ N, which is the most unfavorable loading condition during one walking cycle. This force was determined on the basis of a coordinate system with origin in the middle of the femur head. In the FE model the force has its origin at the place of where normally the cup is attached to the lumic. The force of chapter 2.3 needs to be transformed in order to mimic the

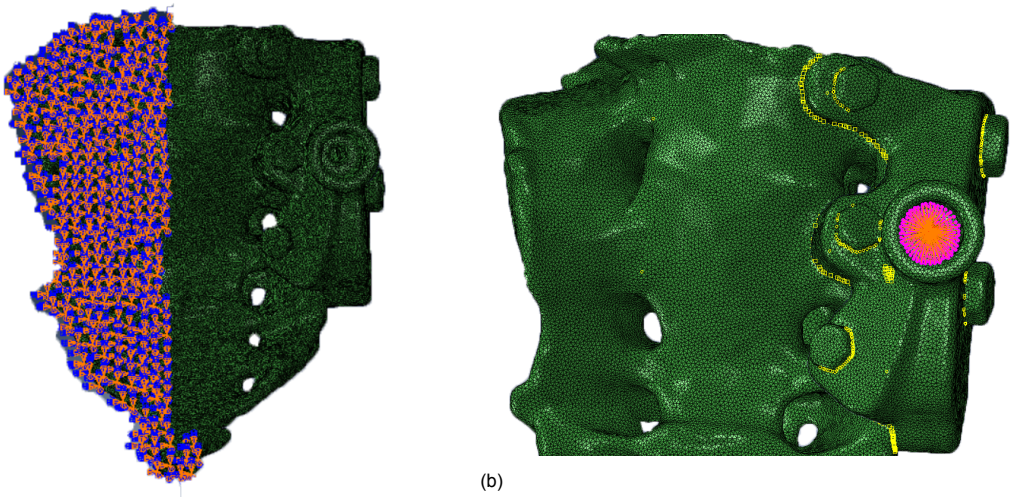

(a) (b)

Figure 2.36: (a) Boundary condition encastre (U1 = U2 = U3 = UR1 = UR2 = UR3) on surface of half of the sacrum. (b) Coupling constraint coupling all the nodes were load and moment is applied to one reference node.

force as determined earlier. This transformation is done by adding a moment to the force. This added moment is calculated by using the distance between the attachment points as leverarm. In figure 2.37 this transformation is explained.

In the model with the old LUMiC the place were the cup is attached is much higher than the place of attachment of the force as determined in chapter 2.3. The force on the old LUMiC should be transformed to mimic the force used in chapter 2.3. This transformation is done by adding again a moment as shown in figure 2.37.

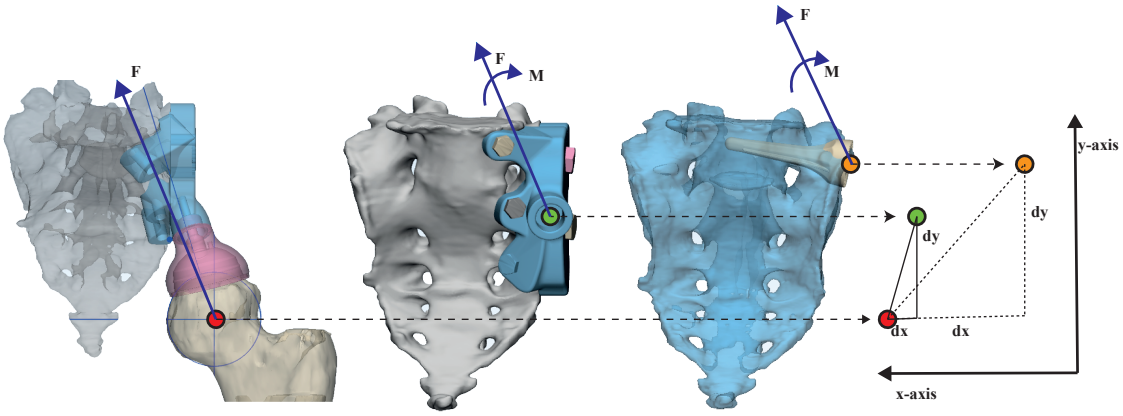

Figure 2.37: The defined load of chapter 2.3 has origin in the head of the femur (left), the load needs to be transformed to different location by adding a moment. The transformation is shown of model 2 (middle; same transformation for model 3 and 4) and model 1 (right).

The Force and moment are added in the model by the use of a coupling constraint that couples all the nodes of at the connection of the cup to the prosthesis to one reference node. The load and moment are than set to this reference nodes. The load and moment are than equally divided onto the nodes of the constraint. A representation of the coupling constraint is shown in figure 2.36b.

2.4.5. Mesh convergence

In finite element modelling a finer mesh in general results in a more accurate solution, but also increases computation time significant. Challenge in finite element modelling is to find a accurate solution but is also satisfactory in terms of computation time. In order to find this solution a mesh convergence study is executed. This is done by first creating a model with the fewest reasonable number of elements to execute the model. Afterwards, the mesh of the model is recreated with denser mesh resulting in more elements. The mesh is then decreased until the results converged, meaning that the mesh in no longer of influence for the result of the model. The model is seen as converged when results are less than 5 % apart. Three models with three different mesh sizes were created and evaluated. The results are shown in table 2.8. The model with 120665 nodes is eventually chosen to execute.

Table 2.8: Number of nodes and max deformation U in mm.

Number of nodes	**5128**	**75330**	**120665**	**502385**
Max deformation (mm)	0.1687	0.2257	0.2581	0.259

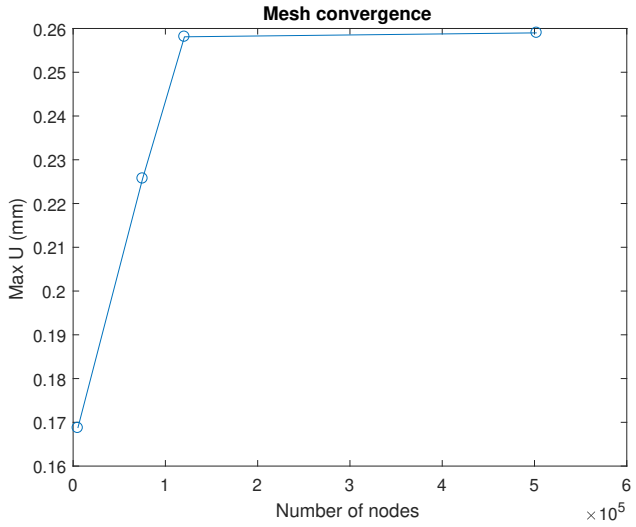

Figure 2.38: Mesh convergence. At 120665 nodes the max deformation is converged.

2.4.6. Postprocessing

In this part the measuring of the micromotions will be elucidated. In each model a group of nodes on the sacrum and the prosthesis will be selected. The total displacement of each group will be measured and averaged. Subtraction of both averaged displacement will lead to relative micromotions between implant and bone. These groups will be selected at the interface between the old LUMiC and the bone for model 1 and at flap 1, 2 and 3 and at the back of the sacrum at a high point, a middle point and a low point for model 2 till 4. The groups for this models are shown in figure 2.40.

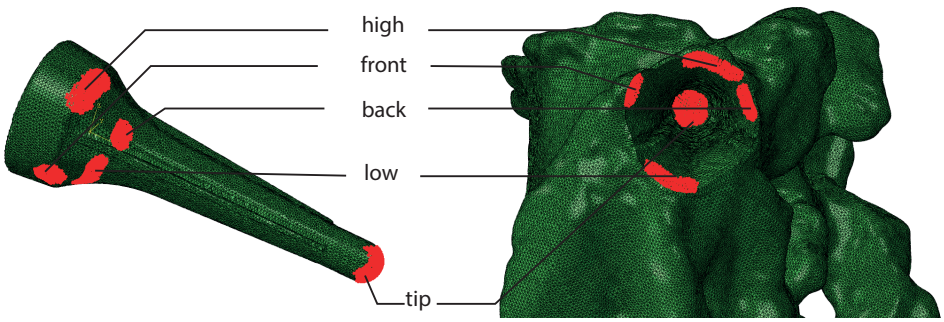

Figure 2.39: Selected groups of nodes for the model with inserted old LUMiC prosthesis. Deformation of each group will be averaged and compared to determine micromotion between implant and bone for each group.

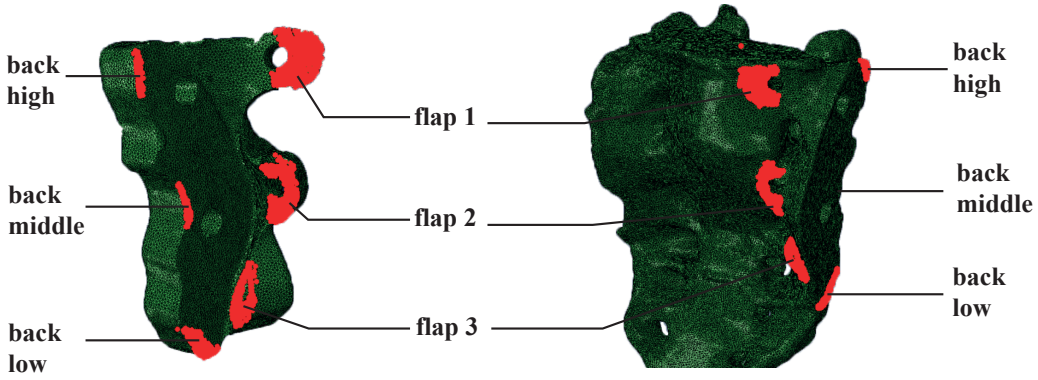

Figure 2.40: Selected group of nodes for the flaps of the prosthesis and the back of the prosthesis for the LUMiC and sacrum. Deformation of each group will be averaged and compared to determine micromotion between implant and bone for each group.

Table 2.9: Overview of number of elements, number of nodes and volume for each part of the FE model.

	Sacrum	Lumic	Screw 25.1	Screw 25.2	Screw 25.3	Screw 80.1	Screw 80.2
Number of elements	304531	78450	2801	2781	2706	10539	10505
Number of nodes	85693	22775	946	945	925	3382	3394
Volume (mm^3)	269592	53624.25	1139.09	1145.37	1143.14	5187.80	5191.07

2.5. 3D printed bone models

After composing of the 3D models of the five cadaver sacra in mimics next step is to develop the 3D printed mechanical bone models. In order to make the mechanical bone models, one cadaveric sacra will be chosen as template for the 3D printed bone model. As described in chapter 2.1 cadaver bone 3 is chosen as a template for the 3D printed bones. The 3D model from mimics of cadaver 3 was exported as a stl to the Ultimaker Cura 4.4 software. In Ultimaker Cura 4.4 the print parameters can be adjusted. Fifteen different bone models will be printed with different print parameters. The parameters that are adjusted for each mechanical bone model are the wall thickness (α) and the infill density (ϕ). The wall thickness mimics the bone cortex of the sacrum. The infill density should mimic the cancellous bone of the sacrum. The Ultimaker 2+ is used for printing. General settings used for printing are shown in table 2.10. The wall thickness α and infill density ϕ (in %) are dependent on table 2.11. The infill pattern should be determined and should have equal qualities as cancellous bone. There are 4 infill categories possible for printing:

1. Strong 2D infills: are used for everyday prints.

2. Quick 2D infills: are used for quick, but weak models.
3. 3D infills: are used to make the object equally strong in all directions.
4. 3D concentric infills: are used for flexible materials.

Possible infill patterns of the Ultimaker 2+ are listed below and shown in figure 2.41.

1. Grid: strong 2D infill.
2. Lines: Quick 2D infill.
3. Triangles: Strong 2D infill.
4. Tri-hexagon: strong 2D infill.
5. Cubic: strong 3D infill
6. Cubic (subdivision): strong 3D infill (saves material compared to cubic)
7. Octet: strong 3D infill.
8. Quarter cubic: strong 3D infill.
9. Concentric: flexible 3D infill.
10. Concentric 3D: flexible 3D infill.
11. Zig-zag: A grid shaped infill, printing continuously in one diagonal direction.
12. Cross: flexible 3d infill.
13. Cross 3D: flexible 3D infill.

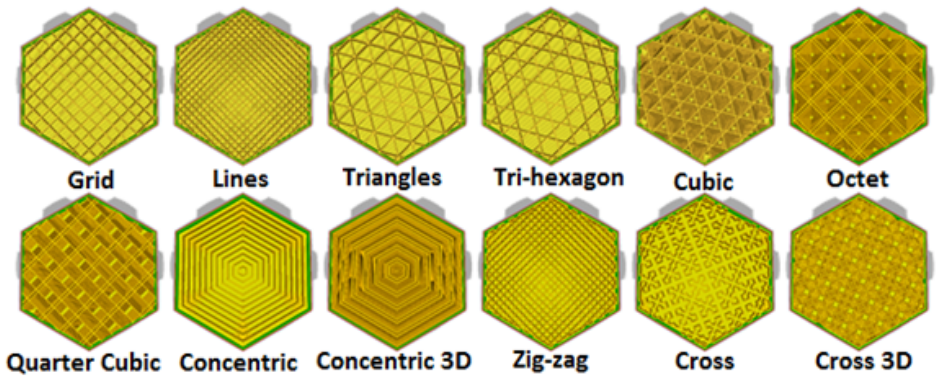

Figure 2.41: Possible infill structures of the Ultimaker 2+ 3D printer.

The choose the final infill pattern of the 3D printed models a few criteria were considered. First criteria was for the model to be strong therefore, the 2D infills were eliminated because these infill patterns are used for quick prints. Quick prints are mostly used to give a quick overview of a design prototype. Because the goal is to perform experiments with the 3D printed bone models a 3D infill pattern is chosen. Furthermore the 3D concentric infills were eliminated as well, because they are suitable for flexible materials. There was no need for the bone model to be flexible during experiments. Consequently, the remaining infill patterns are cubic, cubic (subdivision), octet and quarter cubic. Eventually, the cubic infill pattern is chosen, because this is considered the strongest infill pattern.

Although, the infill pattern was fixed to cubic, the infill density and shell thickness of the models were still variable. An example of wall thickness and infill density are shown in figure 2.42 In order to mimic real sacrum bone the most, four combinations of shell thickness and infill density are chosen for experiments. The combinations are shown in table 2.11.

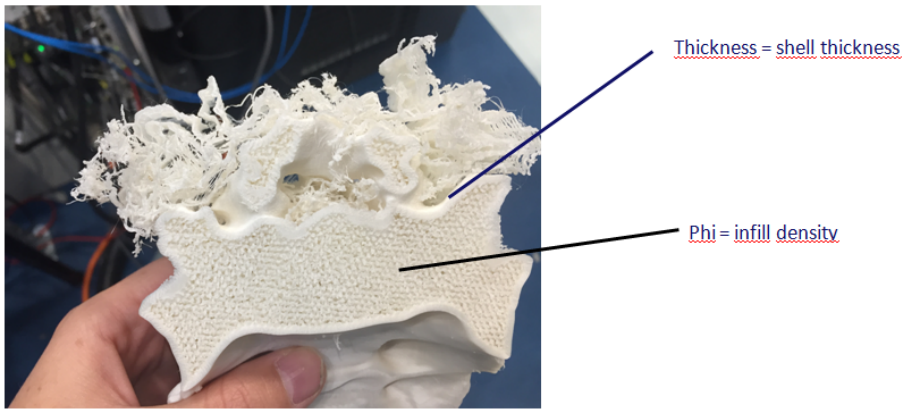

Figure 2.42: Difference between shell thickness and infill density for one printed bone.

Table 2.10: Settings of the Ultimaker 2+ 3D printer used during printing of the mechanical bone models.

Parameters		**Setting**
Standard	Material	PLA
	Nozzle	0.4 mm
Quality	Layer height	0.1 mm
	Initial layer height	0.1 mm
	Line width	0.2 mm
Shell	Wall thickness	α
	Top/Bottom thickness	0.8 mm
Infill	Infill density	ϕ
	Infill pattern	Cubic
Material	Enable retraction	Checked
Speed	Print speed	50 mm/s
	Travel speed	120 mm/s
Support	Generate support	Checked
	Support placement	Everywhere
	Support overhang angle	60
	Support density	15 %
	Support line distance	3 mm
	Support Z distance	0.1 mm
	Support X/Y distance	0.7 mm
Build plate adhesion	Build plate adhesion type	Brim
	Brim width	8.0 mm

Table 2.11: Values of α (wall thickness) and ϕ (infill density) for the different mechanical bone models.

Cadaver bone 3	α = 1.05 mm	ϕ = 20 %
		ϕ = 40 %
	α = 2 mm	ϕ = 20 %
		ϕ = 40 %

2.6. Experiments

In this chapter the design of the test set up is explained. The mechanical bone models with implanted prosthesis aremtested in the INSTRON E10000 biomechanical testing system of faculty Aerospace of TU Delft in the Delft Aerospace Strucutures and Materials Laboratory (DASML). This part will further focus on the technique that is used to measure the micromotions between implant an bone model (bone models of chapter 2.5) and the practical issues of securing the bone models during testing.

In order to give an advise on the improvement of the prosthesis design (subgoal 1 of chapter 1.1) the prosthesis is tested with different alternations of inserted screws. All tested combinations are shown in figure 2.43. Test 1 is with all 5 screws inserted. Test 2 with only the 2 longer side screws inserted. Each test is performed on all selected bone models of chapter 2.5. Which means for example in test 1 the prosthesis design and all inserted screws are implanted into bone model $\alpha = 1,05$ and $\phi = 20\%$, $\alpha = 1,05$ and $\phi = 40\%$, $\alpha = 2$ and $\phi = 20\%$ and $\alpha = 2$ and $\phi = 40\%$. Each bone model with inserted prosthesis and all 5 screws is then continuously loaded in the INSTRON E10000 biomechanical testing system until visible breakage of the bone model. These test are then repeated for each combination of screw alternations as shown in figure 2.43. Consequently, in total 16 tests were performed (4 tests of screw combinations times 4 mechanical bone models).

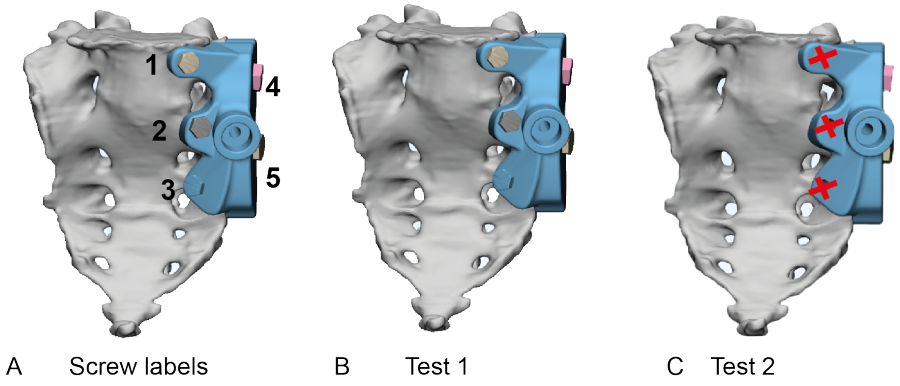

Figure 2.43: Combinations of inserted screws during experiments. Test 1: all screws inserted. (B) Test 2: all front screws are eliminated.(C)

The alignment of the samples in the INSTRON E10000 biomechanical testing system is highly dependent on the defined loading scheme as is explained in chapter 2.3 Important for securing the bones is that all mechanical bone models are aligned in exactly the same way. The design of the test set up is highly dependent on the defined loading of the sacrum as explained in chapter 2.3 because the loading of the sacrum defines the orientation of the sacrum in the loading machine. In chapter 2.3 a force vector is chosen. This force vector is represented as a black line in figure 2.44. This force vector is set to be exactly vertical when the specimen are loaded in the INSTRON machine. The resulting orientation of the sacrum is then show for front, back and side view in figure 2.44.

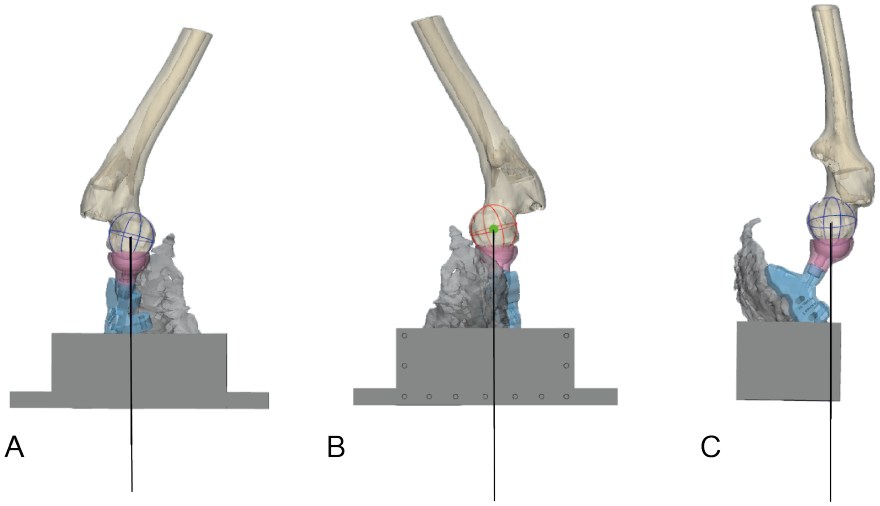

Figure 2.44: Front view (A), back view (B) and side view (C) of the orientation of the sacrum in the test set up. The black line indicates the force vector determined in chapter 2.3 and is held vertical.

In order to align all the 3D printed mechanical bone models exactly as is shown in figure 2.44 the 3D printed bone models are molded using sillicone and resin. Details of molding of the bones are described in chapter 2.6.1.

2.6.1. Molding the bones

All 24 bones should be molded in exactly the same orientation as described in chapter 2.3.1. This section will elaborate on techniques used to mold all the bones. First an aluminium box with dimension 170 mm x 100 mm x 70 mm was made. A Solidworks part that mimics the shape of the bone is made with the cavity function of Solidworks. This part is printed with the 3D printer and shown in figure 2.45.A. Thereafter the bone is positioned and hold at place with a clamp as shown in figure 2.45.B and 3D printed part is removed. A box of plexiglass is made and filled with silicon. After the hardening of the silicon, the bone is removed. As a result a flexible imprint of the bone as in figure 2.45.C shows.

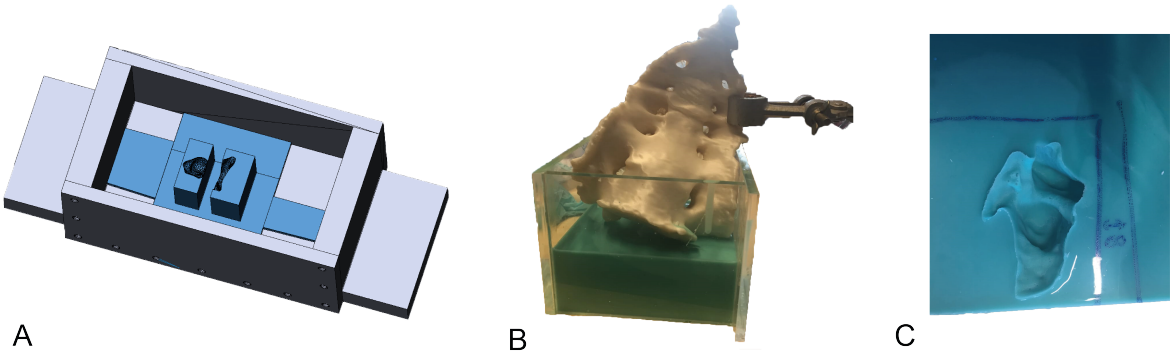

Figure 2.45: A: A solidworks part that mimics the shape of the bone and fits the aluminium box is made. B: The bone is positioned with the Solidworks part. The Solidworks part is removed and the bone is hold into place with a clamp. The box is filled with silicon. C: after hardening of the silicon a flexible mold arises.

Thereafter a reusable box is printed with the 3D printer and used to mimic the created imprint with silicon. This is done by filling the printed box (green box in figure 2.46) with silicon. After hardening of the silicon the result is a reusable mold as shown in figure 2.46.C. Vaseline or silicon spray is used to separate the two silicon parts. The created mold can be used to recreate the mold shown in figure 2.46.A. 16 molds (for each printed bone) are made.

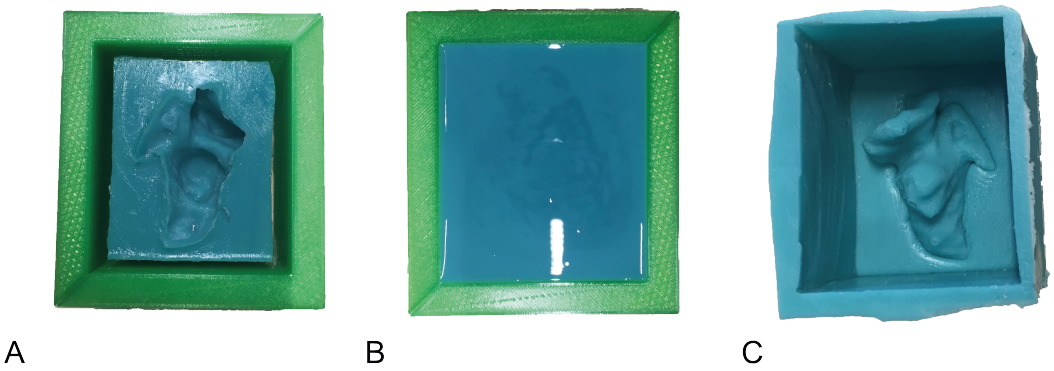

Figure 2.46: The flexible mold of figure 2.45.C is used to create a reusable mold by filling a 3D printed box again with silicon. The created reusable mold is shown in C.

The mold of figure 2.46.C is used to position all 16 printed bone models in the same way in the aluminium box. The mold and the aluminium box are used to fixate the bone with resin. First, the aluminium box is covered by polyvinylalcohol, this is done to easy separate the resin from the box later. After the polyvinylalcohol has dried the silicon mold with bone is positioned into the box and the box is filled with 5 cups of poly-pox UVG 530 resin and 2,5 cups of Poly-pox 155 hardener. The resin and the hardener are stirred thoroughly and thereafter poured into the box. After hardening the bone with resin can be taken out of the aluminium box and later used for testing. The final result is shown in figure 2.47. This process is repeated 16 times for each printed bone model.

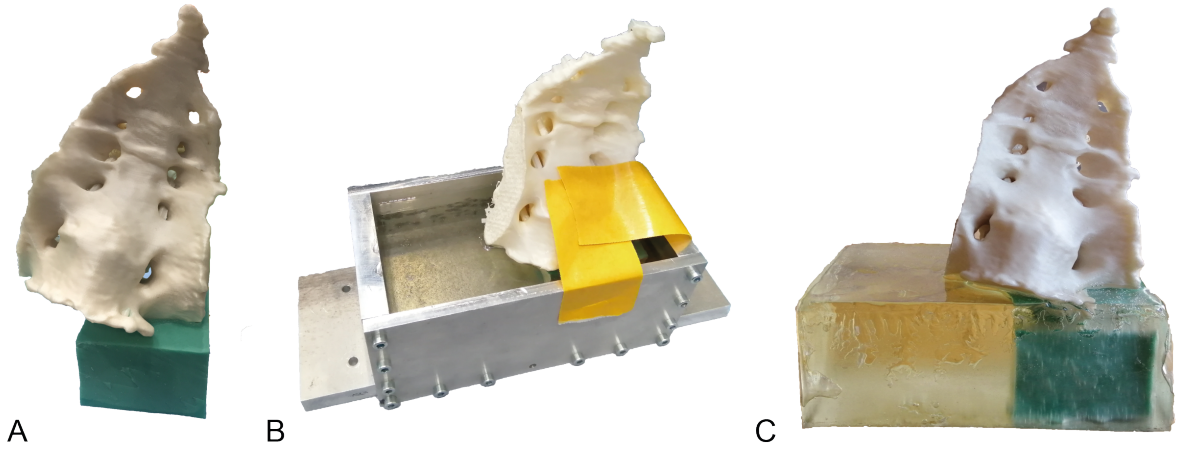

Figure 2.47: A: The flexible silicon mold with bone. B: The aluminium box filled with resin. C: The result after hardening of the resin.

2.6.2. Measuring technique: Digital Image Correlation (DIC)

In this chapter the selection of measurement technique DIC is exemplified.

Digital image correlation is a technique to measure surface deformation of materials and is often used in solid mechanics. It directly gives full-filled displacements and strains of the loaded specimen [42].

In digital image correlation the changes between images of the surface of the specimen in loaded and unloaded phase are evaluated. A cross correlation is done for the pixel intensity in one or more cor-

responding images. This results in the translational shift between two pictures. The cross-correlation is a signal processing technique to evaluate common structures in two different signals.

In short DIC follows the next three steps [42]:

1. Specimen and experimental preparations.
2. Recording images of the planar specimen surface before and after loading.
3. Processing the acquired images using a computer program to obtain the desired displacement and strain information.

Each step will be described shortly below.

1. Specimen and experimental preparation.
In order to perform DIC, the specimen should be prepared. A random pattern should be applied onto the specimen. Often spray paint, a stamp or applying paint with the use of a tooth brush is used to create a speckled pattern (see figure 2.48.A.

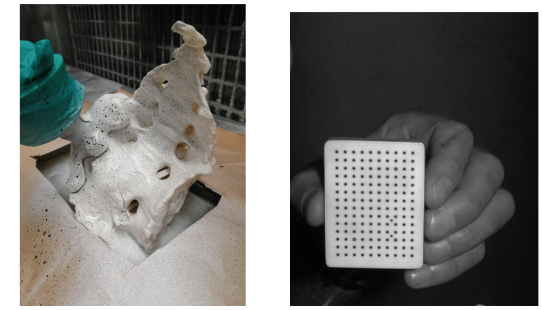

Figure 2.48: A: Apply speckled pattern to sample. B: Calibration image.

2. Recording images of the planar specimen surface before and after loading
In DIC two high resolution cameras are used to make the images. It is important to take into account that the imaging system should not suffer from geometric distortion. Geometric distortion is always more or less present in imaging techniques and there should be reflected for the purpose of the study. if this distortion can be neglected. If not distortion correction techniques can be used [42].

3. Processing the acquired images using a computer program to obtain the desired displacement and strain information
First, the calculation area in the unloaded image should be prescribed and divided into an evenly spaced virtual grid as shown in figure 2.49: left. The displacements are computed at every intersection point of the grid (see figure 2.49: right). In general is DIC the tracking of the same point between two images recorded unloaded and loaded. The basic principle is shown in figure 2.50. To calculate the similarity between the reference subset and the target subset a cross-correlation criterion is used. The peak position of the correlation coefficient is determined. The coordinates of point $(x_i^{'}, y_i^{'})$, which is a point in the deformed image, can be located between two pixels. A certain pixel interpolation scheme should be used, for example the Newton-Raphson method [42].

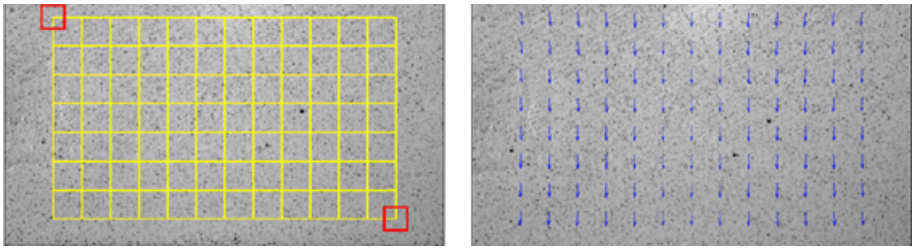

Figure 2.49: left: reference image, the red square is used for tracking the motion of the center point. The intersection point of the yellow grid denote the points to be calculated. Right: the calculated displacement vectors on the deformed image[42].

Although DIC is frequently used in literature it is often presented under a different name, as digital speckle correlation (DSCM), texture correlation, computer aided speckle interferometry (CASI) and electronic speckle photography (ESP) [42].

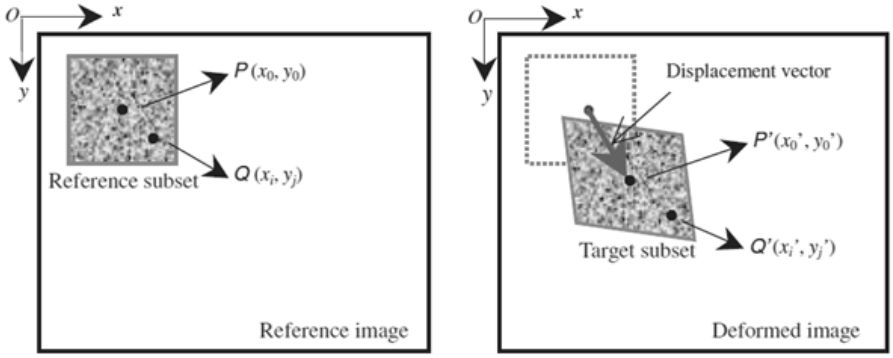

Figure 2.50: schematic representation of a reference square subset before loading (left) and a target subset after loading (right)[42]

During experiments the ViC 3D DIC camera system is used as shown in figure 2.51.A and 2.51.B. Before each test the system will be calibrated using a calibration image, which is shown in figure 2.48.B. The placement of the specimen in the INSTRON machine is shown in figure 2.51.C.

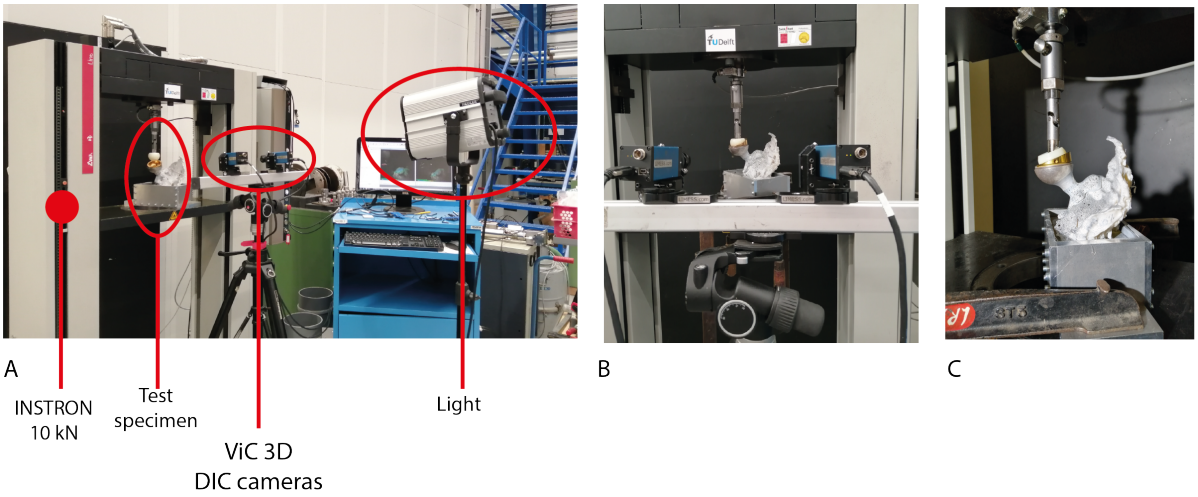

Figure 2.51: A: Overview test set up. B:Test specimen and camera positions. C: Test specimen in INSTRON machine.

3

Results

3.1. Simulation

As mentioned in chapter 2.4 three FE models were developed. First model consists out of the sacrum with the old LUMiC stem inserted. Model 2 consists out of the sacrum and the new prosthesis design inserted while using all screws. Model 3 consists out of the sacrum and the new prosthesis design, but only 2 long side screws are inserted. The post processing was already explained in chapter 2.4.6 and shown in figure 2.40. Five sets of nodes were determined on the surface of the old LUMiC and the sacrum for model 1. These sets were labeled as:

1. Front: 112 nodes on LUMiC, 100 nodes on sacrum.
2. Back: 107 nodes on LUMiC, 121 nodes on sacrum.
3. High: 194 nodes on LUMiC, 210 nodes on sacrum.
4. Low: 236 nodes on LUMiC, 186 nodes on sacrum.
5. Tip: 298 nodes on LUMiC, 206 nodes on sacrum.

As mentioned in chapter 2.4.6 and shown in figure 2.40 6 sets of nodes were determined on the surface of the LUMiC and the sacrum for model 2 and 3. These sets were labeled as:

- Flap 1 (highest flap): 194 nodes on LUMiC, 182 nodes on sacrum.
- Flap 2 (middle flap): 177 nodes on LUMiC, 136 nodes on sacrum.
- Flap 3 (lowest flap): 216 nodes on LUMiC, 144 nodes on sacrum.
- Back high: 40 nodes on LUMiC, 34 nodes on sacrum.
- Back middle: 38 nodes on LUMiC, 26 nodes on sacrum.
- Back low: 93 nodes on LUMiC, 78 nodes on sacrum.

For each set of nodes the average deformation is calculated. Thereafter, the deformation of the set of nodes of the sacrum is subtracted of the average deformation for the group of nodes of the LUMiC. This results in a distance between LUMiC and sacrum which are indicated as the micromotions between implant and bone. For each model the stress and deformation and the micromotions between implant and bone are shown below.

3.1.1. Model 1: old LUMiC

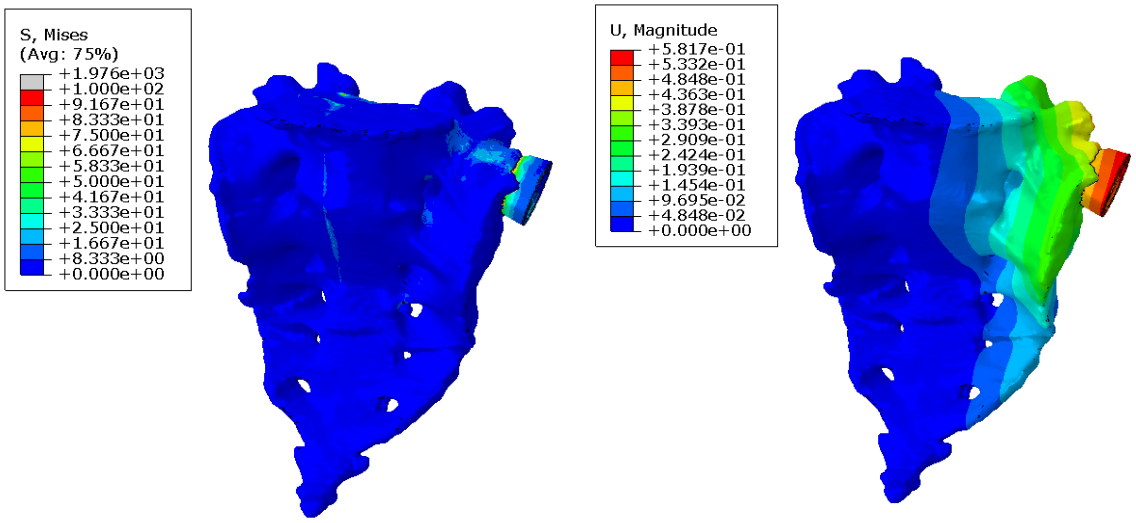

(a) Stress (N/mm^2) (b) Deformation (mm)

Figure 3.1: Stress and deformation of model 1 (sacrum and inserted old LUMiC).

Measured micromotions for model 4 (sacrum and new 3D LUMiC with 3 inserted screws) are shown in table 3.1.

Table 3.1: Micromotions in x (U1), y (U2) and z(U3) direction and total micromotions (U) for model 1 with old LUMiC inserted.

	U (μm)	**U1 (μm)**	**U2 (μm)**	**U3 (in μm)**
Front	109.5523	57.3875	8.2151	92.9563
Back	25.9936	17.3957	17.8917	7.2762
High	25.5496	22.3307	10.1942	7.0851
Low	185.4484	148.1406	3.3283	111.5097
Tip	2.9630	0.8133	1.8737	2.1465

3.1.2. Model 2: All screws inserted

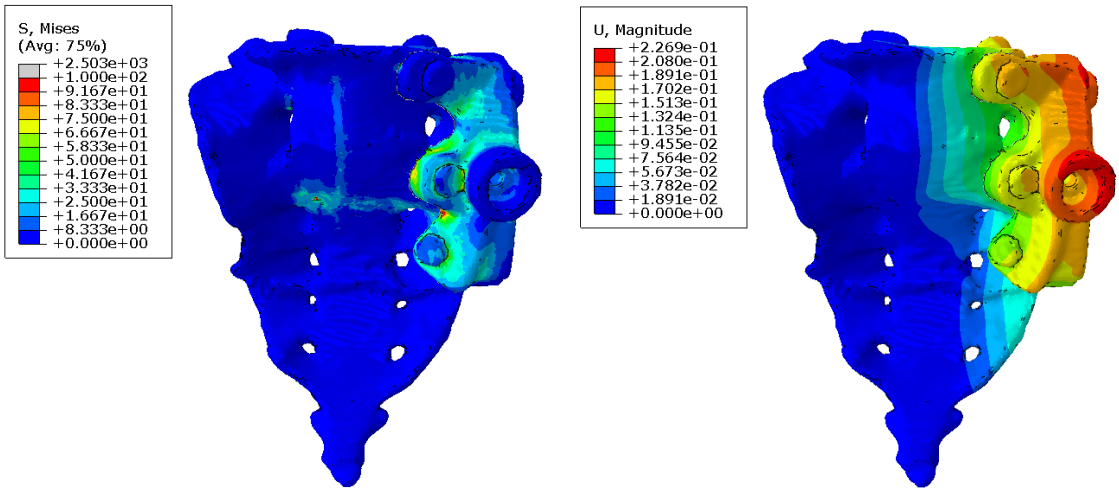

(a) Stress (N/mm^2) (b) Deformation (mm)

Figure 3.2: Stress and deformation of model 2 (all screws inserted). Most stress in the bone at the height of lowest long side screws (screw 5 of 2.31).

Measured micromotions for model 2 (Sacrum and new 3D LUMiC with 5 inserted screws) are shown in table 3.2.

Table 3.2: Micromotions in x (U1), y (U2) and z(U3) direction and total micromotions (U) for model 2 with all screws inserted.

	U (μm)	U1 (μm)	U2 (μm)	U3 (in μm)
Flap 1	27.0697	25.2815	5.4739	24.3057
Flap 2	12.9994	12.3431	8.7119	9.1989
Flap 3	3.3998	3.3254	24.2013	10.0069
Back high	14.4373	6.3673	6.4576	12.4067
Back middle	8.4407	1.7394	14.5524	3.2114
Back low	51.2296	44.6869	19.8904	31.4429

3.1.3. Model 3: 2 screws inserted

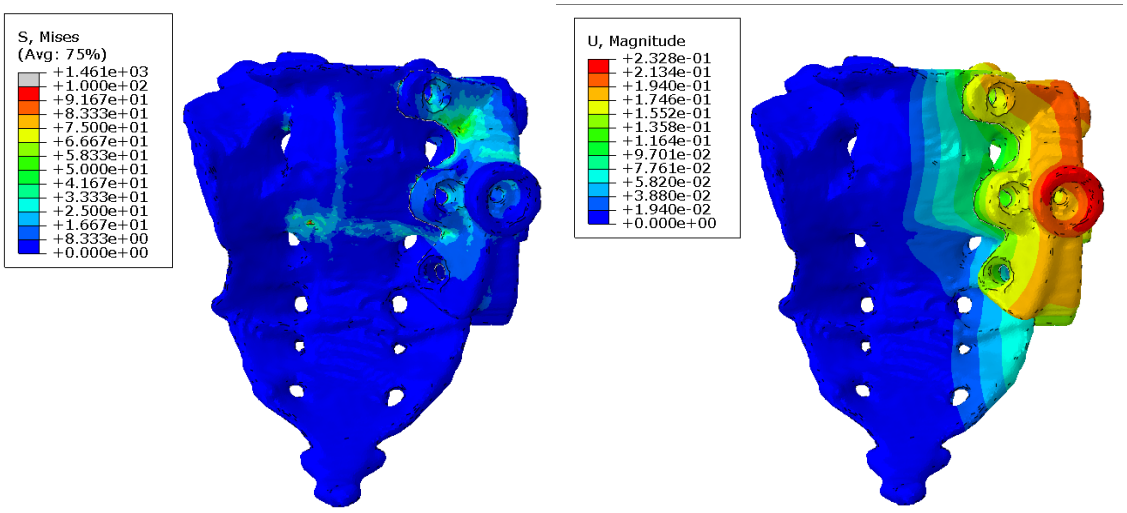

(a) Stress (N/mm^2)

(b) Deformation (mm)

Figure 3.3: Stress and deformation of model 3 (2 screws inserted)

Measured micromotions for model 3 (sacrum and new 3D LUMiC with 2 inserted screws) are shown in table 3.3.

Table 3.3: Micromotions in x (U1), y (U2) and z(U3) direction and total micromotions (U) for model 3 with 2 screws inserted.

	U (μm)	U1 (μm)	U2 (μm)	U3 (in μm)
Flap 1	34.3939	19.1892	10.6479	26.4828
Flap 2	21.6961	8.2058	14.5136	13.8831
Flap 3	60.8612	20.2698	56.3447	10.8855
Back high	13.1425	6.3890	2.2970	11.2531
Back middle	16.8495	1.3630	16.6954	1.8199
Back low	74.2952	48.5144	47.9165	29.4982

3.2. Comparison FE models

When evaluating the micromotions of all models with the new prosthesis implanted it is clear that in all models the micromotions between implant and bone are at its maximum at the place of the back of the prosthesis at the low point (see figure 3.4). The least amount of micromotions were found in model 2, with all screws inserted. As explained in chapter 1.4.2 the micromotions should be less than 150 μm in order to allow bone ingrowth and preferable even less than 28 μm [28]. When Evaluating the micromotions of figure 3.4 this number is exceeded in the old LUMiC model, which indicates this model is more likely to fail compared to the models with the new prosthesis design. Model 2 (all screws) and model 3 (2 screws) both do not exceed this number which indicates the prosthesis design is stable and will less likely fail compared to the old LUMiC stem.

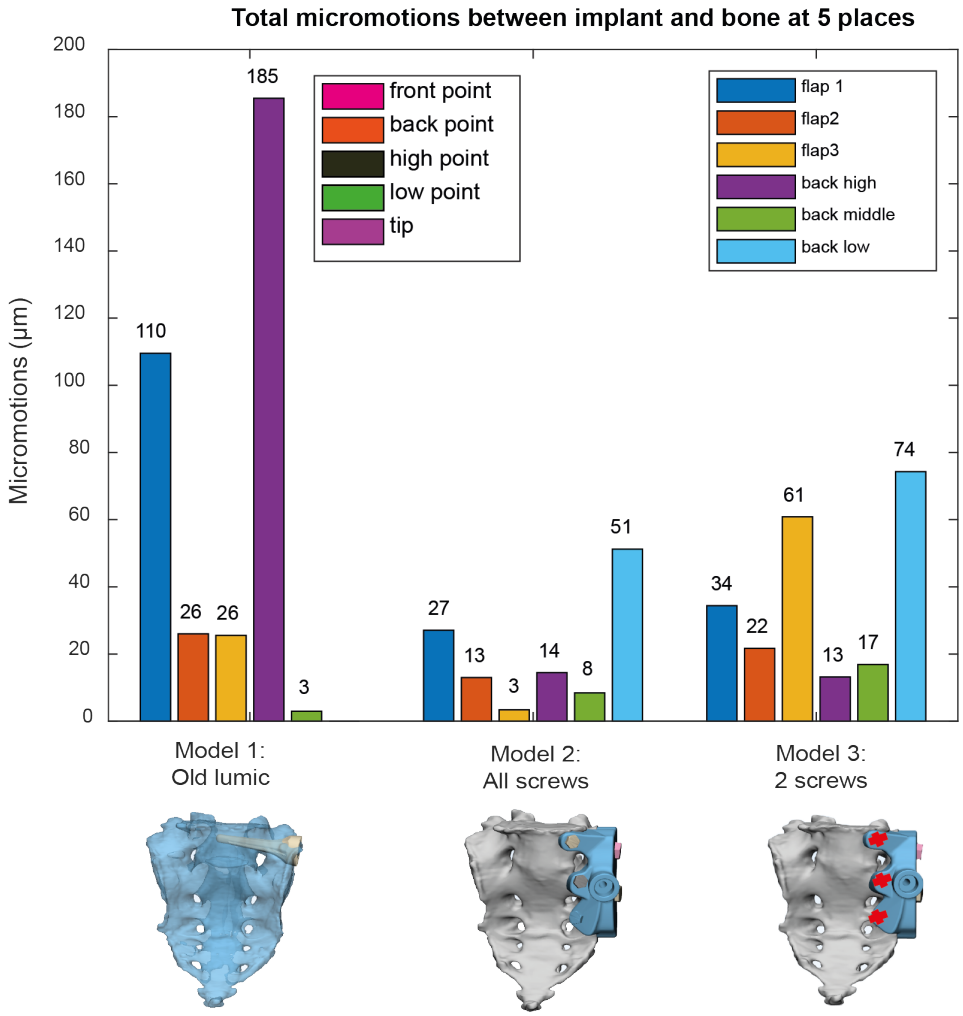

Figure 3.4: Overview of the micromotions at 5 or 6 different places for each model used in simulation (red cross indicates eliminated screws). Most micromotions for models 2 and 3 appear at the back low point , The least overall micromotions occur in model 2; all screws inserted.

The micromotions measured in model 2 and 3 of the FE model will be compared to the micromotions that appeared during experiments in the next chapter.

3.3. Experiments

After performing the experiments of chapter 2.6 the data is analyzed using the Vic 3D 8 post processing software. In chapter 2.5 the different 3D printed bone models are discussed. The developed bone models are 1mm shell thickness and 20% infill density, 2mm shell thickness and 20% infill density, 1mm shell thickness and 40% infill density and 2mm shell thickness and 40% infill density. For each of this 3D printed bone models two tests were executed (see table (3.4)). For each bone model one tests with all screws inserted and one test with only the two long side screws inserted were performed (as is in accordance with chapter 2.6).

1mm 20%	**2mm 20%**	**1mm 40%**	**2mm 40%**
test 1: all screws	test 3: all screws	test 6 all screws	test 7: all screws
test 2: 2 screws	test 4: 2 screws	test 5: 2screws	test 8: 2 screws

Table 3.4: All performed tests (test 1 to 8) during experiments. For each bone 2 tests were executed. One test will all screws inserted and one test with only 2 long side screws inserted

First notable results immediately after testing are shown in figure 3.5. In figure 3.5. A the black line indicates the place of the prosthesis before loading. It is clear that the prosthesis moved in frontal direction during loading especially the bottom part of the prosthesis. All bone models cracked during testing. In figure 3.5.B a crack characteristically for a model with 2 screws inserted is shown. All models with 2 screws inserted cracked the same, at the height of the lowest side screw (screw 5 in figure 2.31). In figure 3.5.C a crack characteristically for the models with all screws inserted is shown. As you can see, for these models, the cracked slopes in the direction of the lowest frontal screw. The printing structure of the mechanical bone models together with the specific geometry of the sacrum bone could influence the crack propagation of the bone. Especially the holes in the bone could result in cracking close the these holes. One sample cracked at the opposite side of the prosthesis as is indicated in figure 3.5.D.

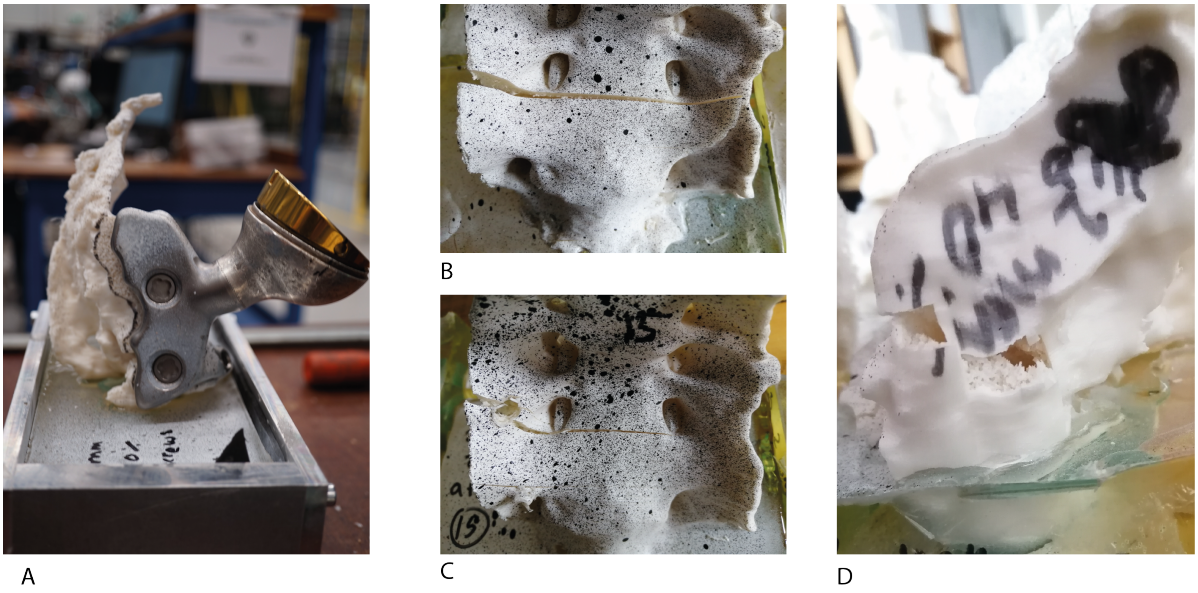

Figure 3.5: Results immediately after loading. A: black line indicates place of prosthesis before loading. It is clear that the prosthesis moved to frontal side, especially the bottom part of the prosthesis. B: Typical crack for a model with 2 screws inserted. C: Typical crack for a model with all screws inserted. Compared to the 2 screws model the crack propagation differs. D: One sample cracked at opposite side of the prosthesis.

Second observation immediately after testing is made clear in figure 3.6. The crack is marked as the dashed black line and the place of screw insertion as a red circle. It is clear that in the model with

all screws inserted the crack initiates behind the place of screw insertion (black arrows in figure 3.6) while in the model with only 2 screws inserted the crack initiates precisely at the height of the lower side screw (screw 5). Furthermore, it seems that the crack is much deeper in the models with all screws inserted compared to the models with only the 2 long screw inserted.

Figure 3.6: Crack propagation for all screws inserted (top) and 2 screws inserted (bottom). Dashed black line indicates crack and red circle indicates place of screw insertion. Initiation of crack in the models with all screws inserted is behind the lower side screw, while for the models with two screws inserted the crack initiates precisely at the height of the lower side screw (screw 5).

The ViC 3D camera system was calibrated before each test using a calibration sample. During tests the cameras recorded a picture each second. For each picture the force and deformation at that moment were saved. All pictures for each test were exported into the ViC 3D 8 processing software and analyzed. All samples were loaded until dislocation of the LUMiC cup, which means loaded until the cup is out of the socket. An example of the data analysis is shown in figure 3.7. Two extensometers were virtually stuck onto the data. Extensometer 1 measured micromotions between implant and bone at flap 3. Extensometer 2 is focused on the crack of the bone model. This is the moment the ΔL of extensometer 1 is greater than 0.01. This point is taken as a measure for the end of the plastic material

region of the bone, which is important for further data processing.

A comparison between all screws inserted and 2 screws inserted for each 3D printed bone model is shown in figure 3.8. It should be mentioned that the 2mm 40% bone model with all screws inserted could withstand the highest overall load during testing. Two long screws inserted could withstand a higher peak load compared to all screws inserted in the 2mm 20% bone model, all screws could withstand a higher peak load in all other models. Furthermore, it should be mentioned that for the models with only 2 long screws inserted a force plateau is reached while for the models with all screws inserted no force plateau is reached.

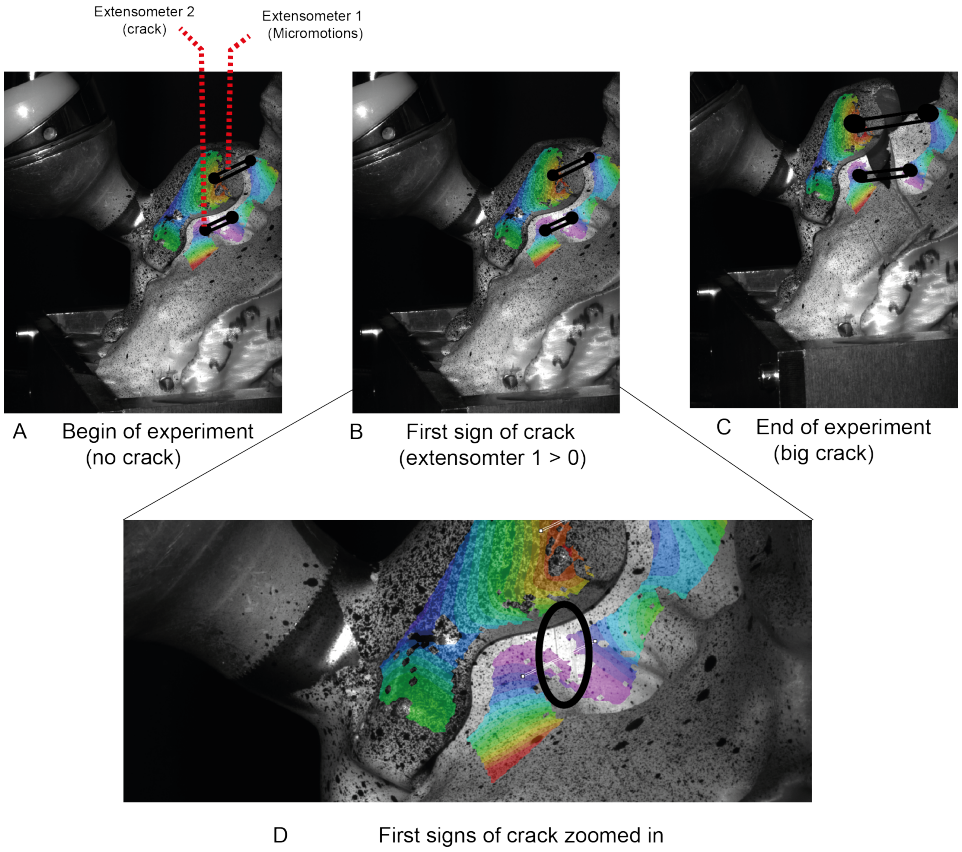

Figure 3.7: Overview of data analysis. The focus of the analysis is on the interface between implant and bone at flap 3 and on the crack propagation. A: begin of experiments. Two extensometers were virtual stuck to the data. Extensometer 1 measured micromotions between implant and bone at flap 3. Extensometer 2 is focused on the crack in the bone model. B: First sign of crack. This is the moment the ΔL of extensometer 2 is greater than 0.01. This point is taken as a measure of the end of the plastic material region of the bone. C: End of experiment. D: First sign of crack zoomed in. A small crack is visible

In figure 3.9 for each sample the force and the ΔL for both extensometers for each moment in time is shown. Figure 3.9 together with figure 3.10 clearly shows that the crack in the models with 2 screws inserted initiates at a higher force compared to all screws. The model 2mm 20% cracks at the highest force when all models are compared. At the moment of dislocation of the LUMiC cup and end of the test the crack (ΔL extensometer 2) is lower for the models with 2 screws inserted compared to all screws, also the micromotions at flap 3 (ΔL extensometer 1) are lower at this moment for all models besides model 1mm 20%. Moreover, in figure 3.10.B the crack (ΔL extensometer 2) for all models at a force of $F = 1100N$ is shown. It is clear that in all models, except for model 1mm 40%, the crack at 1100N is greater for the models with all screws inserted compared to the models with only 2 inserted screws. This indicates that the models with 2 screws inserted are more resistant to cracking of the bone. Also the micromotions between implant and bone at flap 3 for all models are shown in figure 3.11. The micromotions between implant and bone at $F = 1100N$ are higher for the models with only 2 side screws inserted compared to all screws inserted.

The tests of table 3.4 all are repeated one time. The raw results are shown in appendix A.2. In

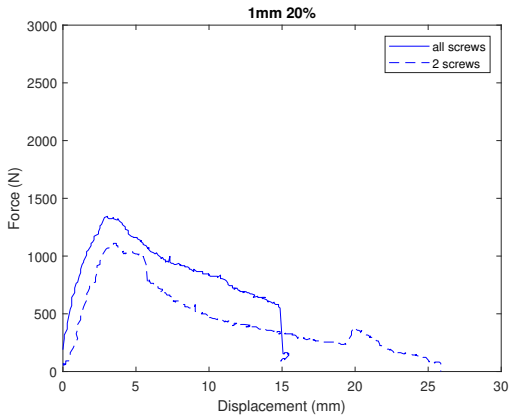

(a) Model 1mm 20%

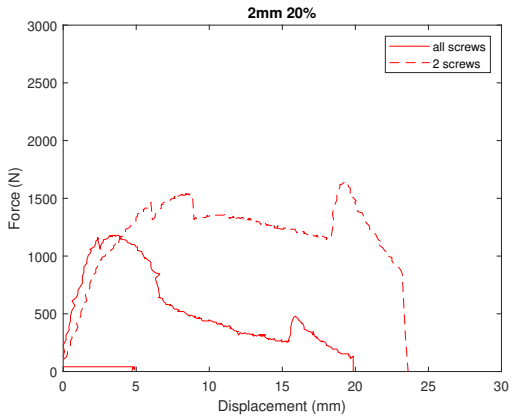

(b) Model 2mm 20%

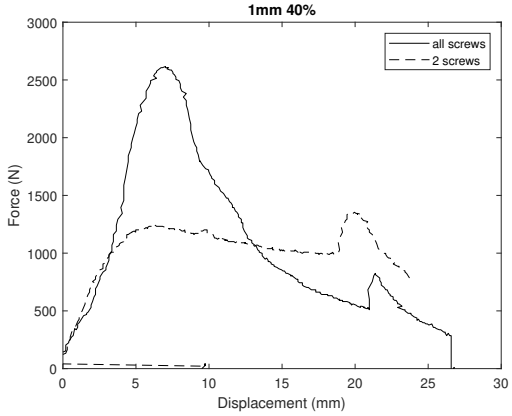

(c) Model 1mm 40%

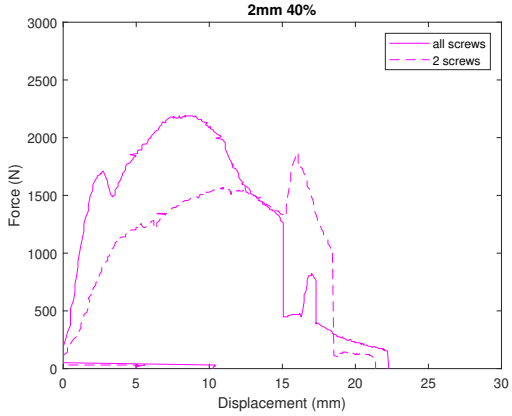

(d) Model 2mm 40%

Figure 3.8: Comparison all screws inserted and 2 screws inserted in all 3D printed bone models. 2 screws inserted performs best in model 2mm 20%. All screws inserted performs best in all other models.

some samples a error occurred. The errors were as follows. For one sample the resin was poorly mixed which resulted in too soft resin that affected the test results a lot. furthermore, for two samples there was a problem with the camera recording which made it impossible to post process the data properly. The problems with the data samples resulted in a large variability between tests. For the tests were no errors occurred the trend of the data between the two tests are comparable. This is shown in appendix A.2.

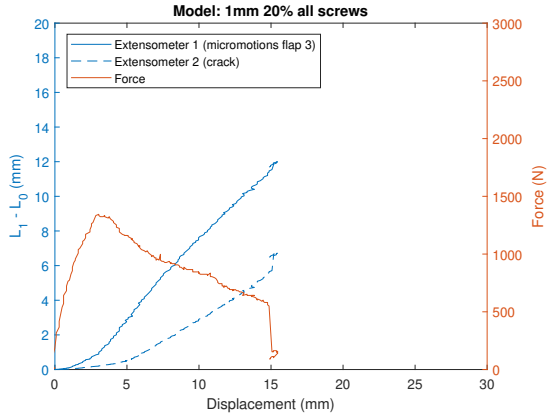

(a) Model 1mm 20% all screws.

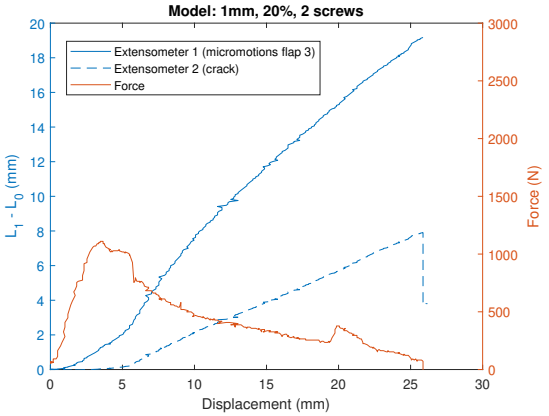

(b) Model 1 mm 20% 2 screws.

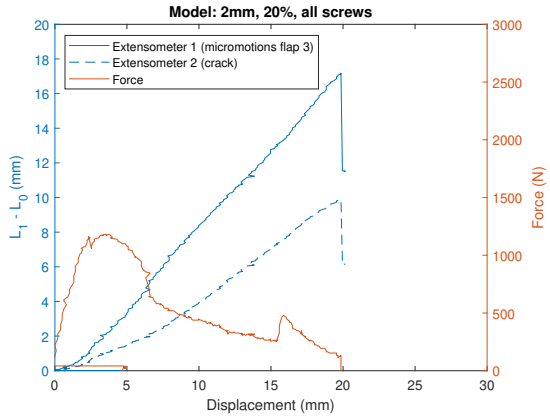

(c) Model 2 mm 20% all screws.

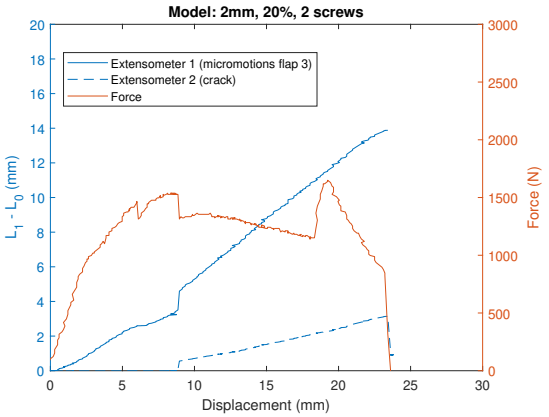

(d) Model 2 mm 20% 2 screws.

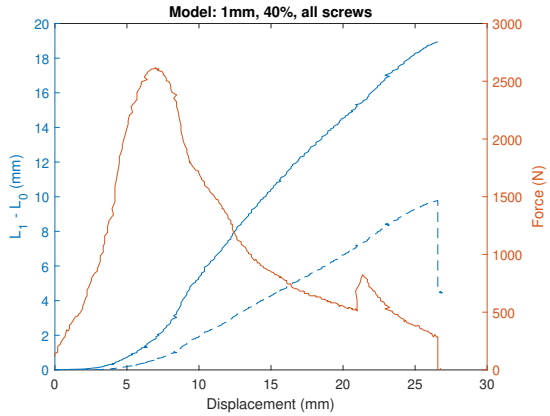

(e) Model 1 mm 40% all screws.

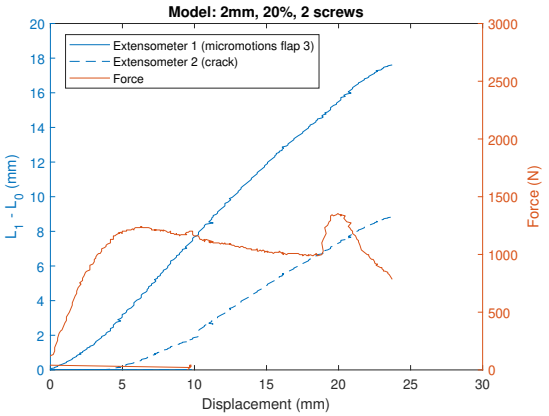

(f) Model 1 mm 40% 2 screws.

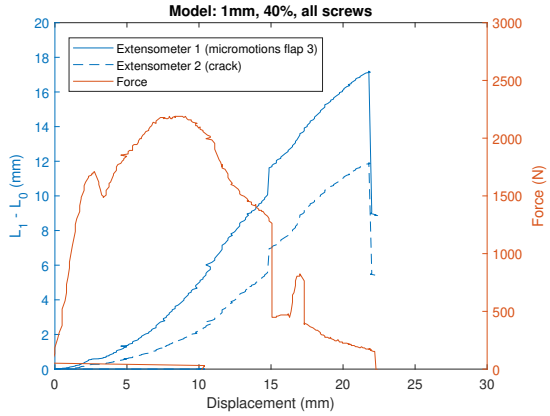

(g) Model 2 mm 40% all screws.

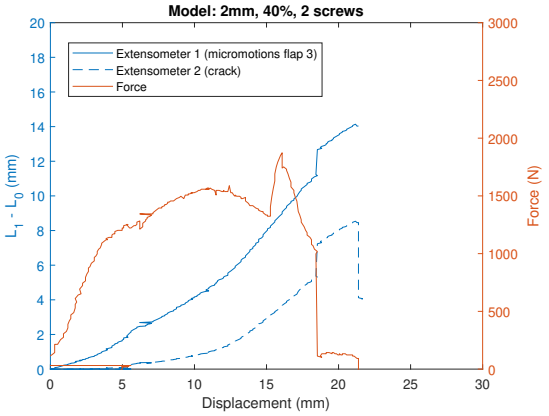

(h) Model 2 mm 40% 2 screws.

Figure 3.9: Overview Force and extensometers for all models.

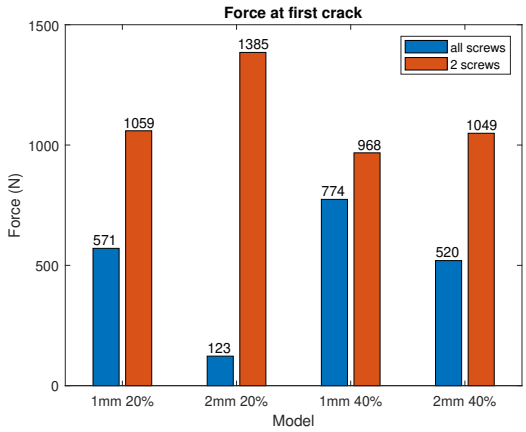

(a) Force at moment of first signs of a crack

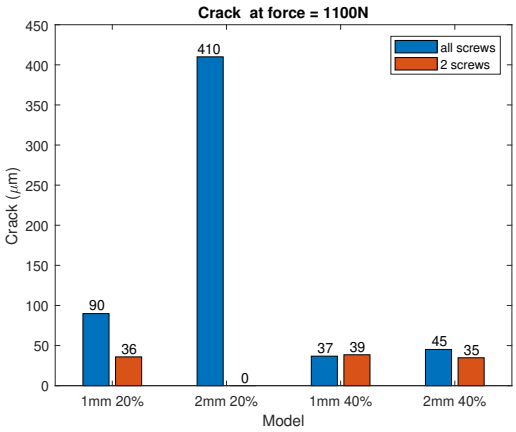

(b) Crack at 1100N for each model

Figure 3.10: A: Force at moment of first signs of a crack (ΔL extensometer 1 > 0.01) in the bone model for each model. In all models the force at first crack is higher when 2 screws were inserted compared to all screws. B: the crack (ΔL extensometer 2) for all models at a force of 1100N.In all models, except for model 1mm 40%, the crack at 1100N is higher for the models with all screws inserted compared to the models with only 2 inserted screws indicating the models with 2 screws inserted are more resistant to cracking of the bone.

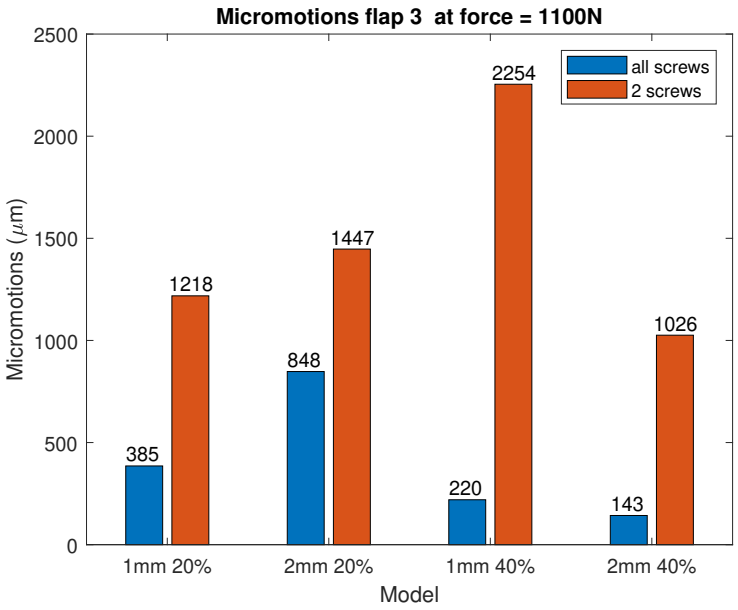

Figure 3.11: Micromotions at flap 3 at $F = 1100$N for all models. The micromotions between implant and bone at $F = 1100$N are higher for the models with only 2 side screws inserted compared to all screws inserted.

3.3.1. Compare test results with FE model

In this part the results of the FE model and the experiments will be discussed. First, it should be mentioned that when looking at the stress in the bone in the FE models the crack propagation of figure 3.5.B and 3.5.C. The stress in the bone for both models is highest at the points were the bone models cracked during experiments. For the models with all screws inserted the propagated in the direction of the lowest frontal screws (screw 3 in figure 2.31.A). In the FE model with all screws inserted the stress is also high at this place.

After post processing it is possible to compare the 3D printed bone models of chapter 2.5 with the FE model of chapter 2.4. First, the data of extensometer 2 is used to determine at which force the bone model cracked. This is done by determine the point the ΔL of extensometer 2 exceeded 0.01. This force for each model is shown in figure 3.10.A. This was necessary because the FE model does not take cracking of the bone into consideration. With other words, the FE model only considers plastic behavior of the bone. To make a could comparison, in the 3D printed bone models also only the region before cracking is considered. Two out of eight models cracked close to 500N (model 1mm 20% all screws and 2mm 40% all screws). For each 3D printed bone model the micromotions at flap 3 of the prosthesis at $F = 300N$ and $F = 500N$ are considered and shown in figure 3.13. Subsequently a load of respectively 100N and 500N are set to the FE model for both FE model 2 (all screws inserted) and FE model 3 (2 screws inserted). Resulting micromotions at flap 3 in these FE models were calculated and added to figure 3.13. It should be mentioned that for model 2mm 20% with all screws inserted at a load of $F = 500N$ the bone was already cracked (ΔL extensometer 1 > 0.01), which explains the large micromotions in this model at 500N in figure 3.13.C and 3.13.D. Model 1mm 20% is in all cases closest to the results of the FE model.

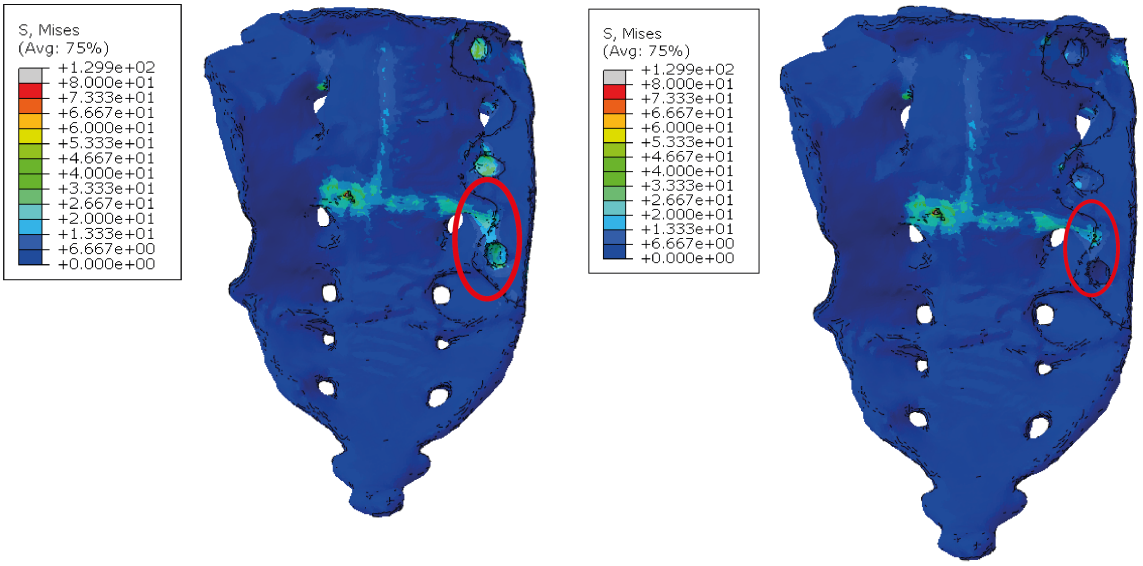

(a) Stress bone (N/mm^2) in Fe model 2; all screws inserted.

(b) Stress bone (N/mm^2) in FE model 3; 2 screws inserted.

Figure 3.12: Stress and deformation of model 2 (all screws inserted) and model 3; 2 screws inserted. The stress is highest at the points were the bone models cracked during experiments.

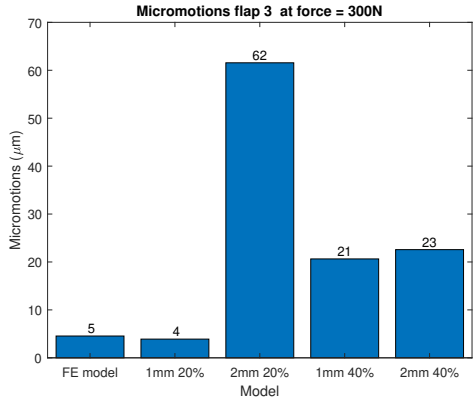

(a) 300N all screws.

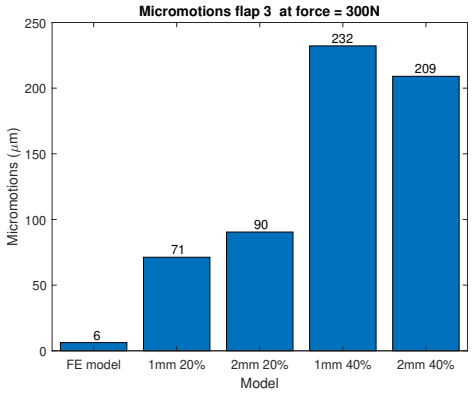

(b) 300N 2 screws

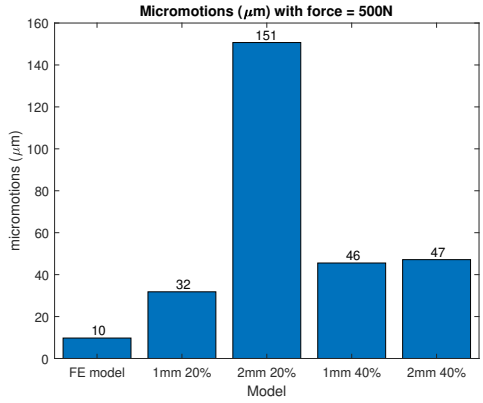

(c) 500N all screws.

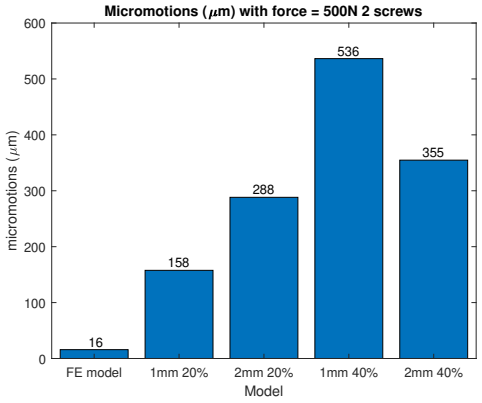

(d) 500N 2 screws

Figure 3.13: Comparison micromotions in FE model and during experiments at a load of 300N and 500N for all bone models. It should be mentioned that for model 2mm 20% with all screws inserted at a load of 500N the bone was already cracked (ΔL extensometer 1 > 0.01), which explains the large micromotions in this model at 500N in C and D. Model 1mm 20% is in all cases closest to the results of the FE model.

4

Discussion and recommendations

4.1. Prosthesis design

In this project a prosthesis for sacral anchoring of the LUMiC cup into the sacrum is developed. In experiments the difference between using only the 2 long side screws compared to using all five screws of the design were compared. Two things stand out. First, when all screws were inserted in general the prosthesis could withstand higher peak load. Also the micromotions at $F = 1100N$ between implant and bone were lower when all screws were inserted compared to both screws. However, cracking of the bone was worse and the first cracking of the bone initiated from a lower force when all screws were inserted compared to only 2 inserted screws. For the models with all screws inserted the crack initiated from frontal screw 3 (the lowest frontal screw). The prosthesis design could be improved by eliminating at least the lowest frontal screw (screw 3 of figure 2.43).

The final prosthesis design of chapter 2.2 is constructed after a iterative process of scoring different designs while taking the design parameters into account. Although the chosen design showed promising results in the simulation and in the experiments still improvements of the design could be considered. The strong points and limitations of the design will be described below.

Two aspects of the design are improved compared to the old LUMiC stem. First the sacral anchoring of the prosthesis. In the old design a stem is inserted at the top of the sacrum. Eight out of 10 patients that were implanted with an old LUMiC stem in the LUMC experienced loosening of the prosthesis. In the new design a porous structure is added at the interface between implant and bone. The porous structure enables bone ingrowth which is beneficial in anchoring of the prosthesis. Furthermore, the surface of contact between implant and bone is maximized while considering the anatomical structure of the sacrum bone by adding flaps at frontal side of the sacrum. In this way the surface of contact between implant and bone is maximized while taken the limitations of surgery into consideration. An example of a limitation during surgery is the position of the patient. The patient lies on his back and turning the patient to his front is challenging and is therefore avoided. Therefore, the flaps that allow screw insertion are placed at the frontal side of the prosthesis.

Second aspect considers the place of the centre of motion of the hip joint. The old LUMiC stem is inserted at the top of the sacrum. Resulting in a lift of centre of motion of 12 cm. This lift results in a leg length difference of approximately 12 cm which is unfavorable for the patient. In the new prosthesis design of the LUMiC this lift is reduced considerable, but is still approximately 5 cm. The lifts of old and new LUMiC prostheses are only evaluated in this studies for the models made in chapter 2.4 and thus considered only one type of sacral anatomy. Recommendations for further research is the evaluation of the lift and leg length difference in more patients and other sacral anatomies. Furthermore, research about the preferable centre of motion for the new LUMiC design could be executed. Altering the centre of motion for the new LUMiC design can be achieved by lowering the attachment of the place of the cup, but this will increase the leverarm of the forces working on the prosthesis and therefore the moments will increase as well. For future research an optimal relation between centre of motion of the hip joint

and maximal moment on the prosthesis should be considered.

Besides improvements of the design compared to using the old LUMiC stem also a few limitations should be discussed. Frist, the frontal flap at the s1 body of the sacral vertebra could be extended more to the midline of the sacrum. Because at the s1 body of the sacral vertebra most space is available for lengthening of the flap without interfering with the sacral nerves. Enlarging of the flap will result in more surface contact between implant and bone. More surface contact is beneficial for the bone ingrowth into the implant which will result into better anchoring of the implant.

Furthermore, in figure 2.11.B design 3.2 is shown which has a rod at back side of the sacrum in order to give rise to a place for screw anchoring at the back of the sacrum. In chapter 2.2 there is shown why design 3.2 is not chosen for the final design. Most important reasons were the sharp edges in this design because of this extra rod and the problems that could arise while implanting this design during surgery. Although this design is not chosen for this thesis adding a back screw could be beneficial for the design. Especially because the use of sacroilliac screws as shown in figure 4.1 is a technique often used in pelvic fixation and considered as one of the best places for anchoring screws into the sacrum [10]. In further research there should be considered if it is possible to add this back screw without the addition of sharp edges in the design. A solution could be to create a design that consists out of two parts that during surgery are pressed or screwed together. To continue about the possibility to add a back screw to the design, during experiments it was clear the prosthesis moved to frontal side of the sacrum at the height of flap 3 of the prosthesis design. To counteract this movement a flap at the height of flap 3 but at backside of the sacrum is an option. In chapter 2.2 this design is already considered but rejected because it is harder to fit this design during surgery. A solution could again be to create a design that consists out of two parts that during surgery are pressed or screwed together.

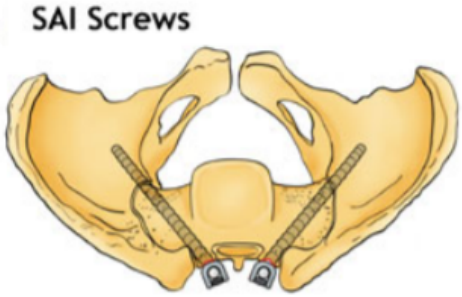

Figure 4.1: Overview of sacroiliac screws in sacrum, a technique often used in pelvic fixation. Screw fixation through the pedicle of the sacrum is considered a good anchoring place [10].

4.2. Simulation

The FE model has several limitations. The interaction between the screws and the bone are modelled as an thermal expansion in which the screw expands with 1 % and has an friction coefficient of 0.3. Although this friction coefficient is often used in literature [25], [29], [37] a research in which the friction coefficient of this type of screws when inserted into sacrum bone should be executed. That will result in better modeling of the screw bone interaction. Furthermore the Poisson's ratio is set to 0.2 for cancellous bone and 0.3 for cortical bone of the sacrum in correspondence to the research of Macleods et al. (2012) [37]. More research focused purely on the cancellous and cortical bone of the sacrum could improve the distribution of Poisson's ratio of the cancellous bone of the sacrum. This would lead to a result more in correspondence with real bone. Moreover, the interaction between the LUMiC prosthesis and the bone is also modelled as a friction with friction coefficient of 0.3. This is done to model the interaction between the porous structure at the inside of the prosthesis and the bone. More research should be done in order to determine the interaction between rough porous structures and bone to improve the model. Furthermore, the model should be validated by performing tests on

cadaver bone of the sacrum. this should be done to ensure the model is in accordance with reality. This would be a good topic for further research.

Moreover, when focusing on the results, the stress in the screws is very high. The maximum value of stress in the screws is exceeding $2000\ N/mm^2$ in all models. This is because the screw is sectioned in a section that expands under the influence of an increase in temperature of 1 degree and a section that is not allowed to expand. This causes very high peak stresses at the transition of sections. The high peak stresses in the screw did not influence the measured micromotions in the model. In future research the modeling of the screws could be improved by added a screw thread instead of using a thermal expansion.

4.3. Experiments

4.3.1. 3D printed Bone models

For the 3D printed bone models the cubic infill pattern is chosen to be fixed in all used bone models. Furthermore, four combinations of wall thickness and infill density were used. Although the cubic infill pattern is chosen on the basis of a few criteria further research could show that a different (weaker) infill pattern is more suitable to mimic real sacrum bone. Particularly, a weaker infill pattern could be more suitable because the selected patient population in need for this kind of sacral anchoring suffer from bone cancer. Bone cancer weakens the bone tremendously. Same arguments could hold for using an even smaller wall thickness and infill structure. More research with cadaver bone from healthy and patients with bone cancer is necessary to select the best infill pattern, infill density and wall thickness for the bone models in future. Furthermore, the infill structure is evenly distributed throughout the whole sacral mechanical bone model. In real bone the density of the cancellous bone differs between parts inside the sacrum form strong parts to porous weaker parts. Research would be necessary to precisely map the distribution of the cancellous bone. Furthermore, tensile tests of the mechanical bone models used to determine the elastic modulus of the bone models would be interesting. The determined elastic modulus could be compared to the elastic modulus of real bone.

4.3.2. Loading scheme

For the loading scheme of chapter 2.3 a few limitations should be addressed. As a starting point for the loading scheme the data from Bergmann et al. (2016) [3] were used. This data was collected by the use of a modified normal hip implant to measure in-vivo data of contact forces in the hip after a total hip replacement. In this thesis a patient specific newly designed prosthesis is implanted. Implantation of this LUMiC prosthesis required removal of very large parts of the hip region including parts of the sacrum. Resulting in probably a very different anatomy and walking cycle for patients that will receive this prosthesis possibly in future and therefore the forces also will differ from the forces measured in the research of Bermann et al. (2016). Preferable the loading condition would be based on loads acting on the new LUMiC prosthesis, but no such data is available yet. In future this data could be collected and used in order to improve the experiments done. Furthermore, not only walking should be considered. Research of Bergmann et al. (2016) [3] showed that the loads during climbing and ascending the stairs exceeds the load during walking. In future research, other activities as climbing and ascending stairs, cycling and jumping could be considered. Moreover, in this study the prosthesis is loaded until dislocation of the cup, however cyclic loading mimicking a large amount of steps should also be considered.

4.3.3. Testing

Limitations of the project during testing will be discussed in this part. First limitation becomes clear when looking at the data of all test samples. This data is shown in appendix A.2. In the appendix test 1 and 2 for each model are shown. It is clear that the results only in few models are comparable but most samples show a difference between test 1 and 2. This indicates a variability between tests. Although the variability can be explained partly by errors in the data sample as for example bad curing of the resin in order to have a more solid result in future more samples should be tested.

Furthermore, the test set up was designed with the test sample exactly aligned with the load direction. As is mentioned in chapter 2.3 the force vector is held vertical during testing. Unfortunately, during testing the micromotions between the implant and bone resulted in movement of the cup and correspondingly movement of the ball joint used to load the specimen. This movement is shown in figure 4.2. As a result of this movement an additional moment should be considered. Therefore, the maximum forces resisted by each model before dislocation as shown in figure 3.8 is lower as expected. This because this additional moment is not taken into consideration. It would be interesting to change the test set up in a way the direction of force stays vertical throughout the whole experiment, or take this additional moment into consideration in further research.

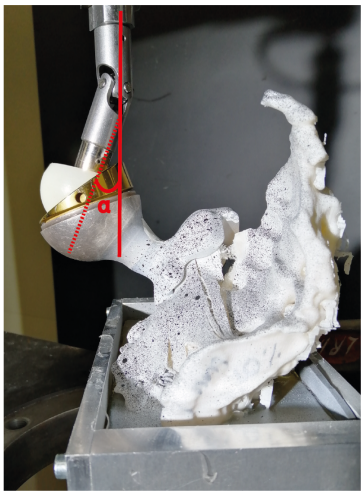

Figure 4.2: Red line: original load direction. Red dashed line: loading direction as a result of micromotions between implant and bone resulting in angle α and an additional moment.

5

Conclusion

Scope of this study was to enable sacrum anchoring of the LUMiC cup by designing a prosthesis and to develop a protocol to *in vitro* evaluate newly designed 3D printed patient specific prosthesis for the sacrum after tumour resection. This main goal was divided into three sub goals. Conclusions for each sub goal will be given below.

5.1. Subgoal 1: Prosthesis design

When the results of the FE model and the experiments are considered. It should be concluded that the prosthesis design is probably better than implantation of the old LUMiC stem into the sacrum but for now is not sufficient yet to be a good anchoring alternative for the LUMiC cup to the bone. This because during experiments the bone could not withstand the most unfavourable load of walking as was determined in chapter 2.3, not even in the bone model that could withstand the highest force (model 2mm 40%). This applies to both models; all screws inserted and two screws inserted. This means that when implanting this prosthesis design in a patient there is a high probability of cracking of the bone during walking, which enlarges the chances of failure of the prosthesis. The prosthesis design should be improved in further research. Fruthermore, a second goal was to give recommendations on improvement of the design. In this project the difference between using the 3 small frontal screws and using only the two side screws is evaluated. Overall, the models with all screws inserted could withstand more load and micromotions between implant and bone were less in three out of four mechanical bone models. However, the cracking of the bone when using the front screws was worse especially at the height of the lowest frontal screw. Therefore in future elimination of only the low frontal screw should considered.

5.2. Subgoal 2: FE model

Second aim of the project is to develop a protocol to *in vitro* evaluate newly designed 3D printed patient specific prosthesis for the sacrum after tumour resection. Two strategies to achieve this goal are elaborated on in this thesis report. First strategy is the development of a FE model of the sacrum that can be used to evaluate the micromotions between the sacrum bone and a newly designed patient specific prosthesis. The newly designed LUMiC of chapter 2.2 is used as a case in order to be able to develop this FE model. Multiple FE models were made. First model consisted out of the sacrum bone and an inserted old LUMiC stem. Other models contained the implanted new prosthesis design with all 5 screws and only the 2 long side screws implanted. When evaluating the maximum micromotions, the model with the old LUMiC scored the worst followed by the model with 2 screws inserted. The model with all screws inserted scored the best, meaning the micromotions between implant and bone were the least. Therefore, the conclusion can be made that the new LUMiC design is a better solution for patients who need limb salvage surgery after bone tumour resection of the sacrum. The FE model has a few limitations as discussed in chapter 4.2. However, because all models were build and evaluated the same way the conclusions about the performance of the different LUMiC designs is legit. The FE model

presented in this research is a good starting point for FE modelling of the sacrum and new designs in future, although parts of the models can be improved as discussed in chapter 4.2. Furthermore, tests with cadaver bone should be done to validate the FE model.

5.3. Subgoal 3: Mechanical bone models

Second strategy was the development of mechanical bone models of the sacrum that can be used during mechanical testing of newly designed prosthesis. New mechanical bone models using 3D printing techniques are developed as mentioned in chapter 2.5. Four mechanical bone models with different wall thickness representing cortical bone and infill densities representing cancellous bone were printed. The model with 1mm shell thickness and 20% infill density showed most similar results with the FE model and has therefore most chance to have same mechanical properties as real bone, but variability between tests was very large. Therefore, more research with an increased number of test samples together with cadaver tests should be done to validate the 3D printed mechanical bone models.

5.4. Final conclusion

For this project there can be concluded that the FE model and the development of 3D printed mechanical bone models together with the experiments are good starting points in the development of a protocol to *in vitro* evaluate newly designed 3D printed patient specific prosthesis for the sacrum after tumour resection but more research with cadaver bone and an increased number of test samples should be done. Furthermore, the newly designed prosthesis could be considered as an improved alternative for the old LUMiC stem although the design could by altered in further research.

Bibliography

[1] M.E. Anderson, R.L. Randall, D.S. Springfield, and M.C. Gebhart. *Sarcomas of Bone*. Elsevier, Philadephia, 2014.

[2] G. P. Beadel, C. E. M. Laughlin, F. Aljassir, P. Ferguson, A. M. Griffin, R. S. Bell, and J. S. Wunder. Iliosacral resection for primary bone tumors: Is pelvic reconstruction necessary? *Clin Orthop Relat Res*, 438:22–29, 2005.

[3] Georg Bergmann, Alwina Bender, Jörn Dymke, Georg Duda, and Philipp Damm. Standardized loads acting in hip implants. *PloS one*, 11(5):e0155612, 2016.

[4] Michaël PA Bus, Andrzej Szafranski, Simen Sellevold, Tomasz Goryn, Paul C Jutte, Jos AM Bramer, M Fiocco, Arne Streitbürger, Daniel Kotrych, Michiel AJ van de Sande, et al. Lumic® endoprosthetic reconstruction after periacetabular tumor resection: short-term results. *Clinical Orthopaedics and Related Research®*, 475(3):686–695, 2017.

[5] D. Campanacci, S. Chacon, N. Mondanelli, G. Beltrami, G. Scoccianti, G. Caff, F. Frenos, and R. Capanna. Pelvic massive allograft reconstruction after bone tumour resection. *Int Orthop*, 36 (12):2529–36, 2012. ISSN 0341-2695. doi: 10.1007/s00264-012-1677-4.

[6] D. B. Chaffin, G. B. J. Andersson, and B. J. Martin. *Occupational Biomechanics*. John Wiley Sons, New York, 1999.

[7] M. Cidamon. *Customized Joint Implants Popular Among Orthopedic Surgeons: Clinical Efficacy Important Internationally*. 2015. URL http://www.prweb.com/releases/2015/02/prweb12509081.htm.

[8] OpenStax CNX. 2016.

[9] P Cronier, G Pietu, C Dujardin, N Bigorre, F Ducellier, and R Gerard. The concept of locking plates. *Orthopaedics & traumatology: surgery & research*, 96(4):S17–S36, 2010.

[10] Romain Dayer, Jean Albert Ouellet, and Neil Saran. Pelvic fixation for neuromuscular scoliosis deformity correction. *Current reviews in musculoskeletal medicine*, 5(2):91–101, 2012.

[11] C. Delloye, X. Banse, B. Brichard, P. L. Docquier, and O. Cornu. Pelvic reconstruction with a structural pelvic allograft after resection of a malignant bone tumor. *J Bone Joint Surg Am*, 89(3): 579–87, 2007. ISSN 0021-9355 (Print) 0021-9355. doi: 10.2106/jbjs.E.00943.

[12] S. Dijkstra. Experience with the lumic partial pelvic replacement, Jun 2016. URL https://www.youtube.com/watch?v=N6h3WtY50XY&t=2036s.

[13] Robert A. Draughn and Yuehuei H. An. *Mechanical Testing of Bone and the Bone-Implant Interface.* CRC Press, 2000. ISBN 9780849302664. URL http://search.ebscohost.com.tudelft.idm.oclc.org/login.aspx?direct=true&db=nlebk&AN=207832&site=ehost-live.

[14] John Elfar, Spencer Stanbury, Ron Martin Garcia Menorca, and Jeffrey Douglas Reed. Composite bone models in orthopaedic surgery research and education. *The Journal of the American Academy of Orthopaedic Surgeons*, 22(2):111, 2014.

[15] W. F. Enneking and W. K. Dunham. Resection and reconstruction for primary neoplasms involving the innominate bone. *Clin Orthop Relat Res*, 60:731–746, 1993.

[16] H. Gelderblom, P. C. W. Hogendoorn, S. D. Dijkstra, C. S. v. Rijswijk, A. D. Krol, A. H. M. Taminiau, and J. V. M. G. Bov□e. The clinical approach towards chondrosarcoma. *The Oncologist*, 13:320–329, 2008.

[17] C. C. Gillis, J. T. Street, and C. G. (2014) Boyd, M. C. and fisher. Pelvic reconstruction after subtotal sacrectomy for sacral chondrosarcoma using cadaveric and vascularized fibula autograft: technical note. *J Neurosurg Spine*, 21:623–627, 2014.

[18] T.G. Grünewald, F Cidra-Aranaz, D. surdez, E.M. Tomazou, E. de Alava, H. kovar, P.H. Sorensen, O. Delattre, and U. Dirksen. Ewing sarcoma. *Nature reviews: Disease primers*, 4(1), 2018.

[19] W. Guo, D. Li, X. Tang, Y. Yang, and T. Ji. Reconstruction with modular hemipelvic prostheses for periacetabular tumor. *Clin Orthop Relat Res*, 461:180–188, 2007.

[20] W. Guo, D. Li, X. Tang, and T. Ji. Surgical treatment of pelvic chondrosarcoma involving periacetabulum. *J Surg Oncol*, 101(2):160–5, 2010. ISSN 0022-4790. doi: 10.1002/jso.21442.

[21] K. D. Harrington. The use of himpelvic allografts or autoclaved grafts for reconstruction after wide resections of malignant tumors of the pelvis. *The journal of bone and joint surgery american volume*, 74(3):331–341, 1992.

[22] O. L. Harryson, Y. A. Hosni, and J. F. Nayfeh. Custom designed orthopedic implants evaluated using finite element analysis of patient-specific cumputedtomography dat: femoral-component case study. *BMC Musculoskelet Disord*, 8:91–100, 2007.

[23] O. L. Harrysson, O. Robertsson, and J. F. Nayfeh. Higher cumulative revision rate of knee arthroplasties in younger patients with osteoarthritis. *Clin Orthop Relat Res*, (421):162–8, 2004. ISSN 0009-921X (Print) 0009-921x.

[24] Uwe Holzwarth and Giulio Cotogno. Total hip arthroplasty : State of the art, prospects and challenges. 06 2012. doi: 10.2788/31286.

[25] Taimoor Iqbal, Lei Shi, Ling Wang, Yaxiong Liu, Dichen Li, Mian Qin, and Zhongmin Jin. Development of finite element model for customized prostheses design for patient with pelvic bone tumor. *Proceedings of the Institution of Mechanical Engineers, Part H: Journal of Engineering in Medicine*, 231(6):525–533, 2017.

[26] R.J. Jackson and Z.L. Gokaslan. Spinal–pelvic fixation in patients with lumbosacral neoplasms. *J. Neurosurg*, 92:61–70, 2000.

[27] W. Jamróz, J. Szafraniec, M. Kurek, and R. Jachowicz. 3d printing in pharmaceutical and medical applications - recent achievements and challenges. *Pharm Res.*, 35(9), 2018.

[28] M. Jasty, R. Krushell, E. Zalenski, D. O'Connor, R. Sedlacek, and W. Harris. The contribution of the nonporous distal stem to the stability of proximally porous-coated canine femoral components. *J Arthroplasty*, 8(1):33–41, 1993. ISSN 0883-5403 (Print) 0883-5403.

[29] Tao Ji, Wei Guo, Xiao-Dong Tang, and Yi Yang. Reconstruction of type ii+ iii pelvic resection with a modular hemipelvic endoprosthesis: a finite element analysis study. *Orthopaedic surgery*, 2(4): 272–277, 2010.

[30] M. R. A. Kadir. *Computational Biomechanics of the Hip Joint*. SpringerBriefs in Applied Sciences and Technology. Springer, Heidelberg New York Dordrecht London, 2014. ISBN 978-3-642-38777-7. doi: 10.1007/978-3-642-38777-7.

[31] H. Kienapfel, C. Sprey, A. Wilke, and P. Griss. Implant fixation by bone ingrowth. *The Journal of Arthroplasty*, 14(3):355–368, 1999.

[32] Lim J.-Y. Shim K.-W. Han J. W. Yi S. Yoon D. H. . . . Shin D. A. kim, D. Sacral reconstruction with a 3d-printed implant after hemisacretomy in a patient with sacral osteosarcoma: 1-year follow up. *Yonsei Med J*, 58(2):453–457, 2017.

[33] Augustinus D Krol, Antonie HM Taminiau, and Judith VMG Bovée. The clinical approach towards chondrosarcoma. *The oncologist*, 13:320–329, 2008.

[34] S. Kurtz, K. Ong, E. Lau, F. Mowat, and M. Halpern. Projections of primary and revision hip and knee arthroplasty in the united states from 2005 to 2030. *J. Bone Joint Surg Am*, 89:780–785, 2007.

[35] S. M. Kurtz, E. Lau, K. Ong, K. Zhao, M. Kelly, and K. J. Bozic. Future young patient demand for primary and revision joint replacement: national projections from 2010 to 2030. *Clin Orthop Relat Res*, 467:2606–2612, 2009.

[36] F. Langlais, J. C. Lambotte, and H. Thomazeau. Long-term results of hemipelvicv reconstruction with allografts. *Clin Orthop Relat Res*, 388:178–186, 2001.

[37] Alisdair R MacLeod, Pankaj Pankaj, and A Hamish RW Simpson. Does screw–bone interface modelling matter in finite element analyses? *Journal of biomechanics*, 45(9):1712–1716, 2012.

[38] E. N. Marieb and K. Hoehn. *Human anatomy physiology*, volume 9. Pearson, 2013.

[39] R.B. Martin, D.B. Burr, N.A. Sharkey, and D.P. Fyhrie. *Skeletal tissue mechanics*. Springer, New York, 2015.

[40] A. J. McKnight, V. O. Lewis, L. D. Rhines, and M. M. Hanasono. Femur-fibula-fillet of leg chmeric free flap for sacral-pelvic reconstruction. *J Plast Reconstr Aesthet Surg*, 66:1784–1787, 2013.

[41] E. Mendel, J. L. Mayerson, N. Nathoo, R. L. Edgar, C. Schmidt, and m. J. (2011) Miller. Reconstruction of the pelvis and lumbar-pelvic junction using 2 vascularized autologous bone grafts after en bloc resection for an iliosacral chondrosarcoma. *J Neurosurg Spine,*, 15:168–173, 2011.

[42] B. Pan, H. Xie, B. Xu, and F. dai. Performance of sub-pixel registration algorithms in digital image correlation. *measurement science and technology*, 17:1615–1621, 2006.

[43] J. B. Park and R. S. Lakes. *Biomaterials: an introduction*. Plenum Press, New York, 1992.

[44] R. M. Pilliar, J. M. Lee, and C. Maniatopoulos. Observations on the effect of movement on bone ingrowth into porous-surfaced implants. *Clinical Orthopeadics and Related Research*, 208:108–113, 1985.

[45] R. M. Pilliar, J. M. Lee, and C. Maniatopoulos. Observations on the effect of movement on bone ingrowth into porous-surfaced implants. *Clinical Orthopeadics and Related Research*, 208:108–113, 1985.

[46] E. Schwameis, M. Dominkus, P. Krepler, R. Dorotka, S. Lang, R. Windhager, and R. Kotz. Reconstruction of the pelvis after tumor resection in children and adolescents. *Cinical orthopaedics and related research*, 402:220–235, 2002.

[47] R. Schwarzkopf, M. Brodsky, G. A. Garcia, and A. H. Gomoll. Surgical and functional outcomes in patients undergoing total knee replacement with patient-specific implants compared with ”off-the-shelf” implants. *Orthop J sports Med*, 3, 2015.

[48] K. Soballe, E. S. Hansen, B. Rasmussen H, P. H. Jorgensen, and C. Bunger. Tissue ingrowth into titanium and hydroxyapatite-coated implants during stable and unstable mechanical conditions. *J Orthop Res*, 10(2):285–99, 1992. ISSN 0736-0266 (Print) 0736-0266. doi: 10.1002/jor.1100100216.

[49] M. S. Thompson, I. D. McCarthy, L. Lidgren, and L. Ryd. Compressive and shear properties of commercially available polyurethane foams. *J Biomech Eng*, 125(5):732–4, 2003. ISSN 0148-0731 (Print) 0148-0731.

[50] T. Ueda and A. Kawai. *Osteosarcoma : A multidisciplinary approach to treatment*. Springer, Tokyo, 2016.

[51] Takafumi Ueda and Akira Kawai. *Osteosarcoma*. Springer, 2016.

[52] Unknown. Pelvis hip anatomy. URL `https://anatomy.lexmedicus.com.au/collection/pelvis-hip`.

[53] unknown. Sacrum, 4th gen., composite, 17 pcf solid foam core, large. URL https://www.sawbones.com/sacrum-4th-generation-composite-matches-3405-3409-3405-2.html.

[54] Annemiek Van Boeijen, Jaap Daalhuizen, Roos van der Schoor, and Jelle Zijlstra. *Delft design guide: Design strategies and methods*. 2014.

[55] P.P. Varga, Z. Szorverfi, and A. Lazary. Surgical resection and reconstruction after resection of tumors involving the sacropelvic region. *Neurological Research*, 36(6):588–596, 2014.

[56] Raphaël Vialle, Nicolas Levassor, Ludovic Rillardon, Alexandre Templier, Wafa Skalli, and Pierre Guigui. Radiographic analysis of the sagittal alignment and balance of the spine in asymptomatic subjects. *JBJS*, 87(2):260–267, 2005.

[57] B. P. Walcott, B. V. Nahed, A. Mohyeldin, J. V. Coumans, K. T. Kahle, and M. J. Ferreira. Chordoma: current concepts, management, and future directions. *Lancet Oncol*, 13(2):e69–76, 2012. ISSN 1470-2045. doi: 10.1016/s1470-2045(11)70337-0.

[58] B. Wang, X. Xie, J. Yin, C. Zou, J. Wang, and J. Huang, G. Shen. Reconstruction with modular hemipelvic endoprosthesis after pelvic tumor resection: a report of 50 consecutive cases. *PLoS ONE*, 10:5, 2015. doi: 10.1371/journal.pone.0127263.

[59] J. Wang, Q. Tang, X. Xie, J. Yin, Z. Zhao, and Z. Li. Iliosacral resections of pevic malignant tunors and reconstruction with nonvascular bilateral fibular autografts. *Ann Surg Oncol*, 19:4043–4051, 2012.

[60] R. Wei, W. Guo, T. Ji, Y. Zhang, and H. Liang. One-step reconstruction with a 3d-printed, custom-made prosthesis after total en bloc sacrectomy: a technical note. *Eur Spine J*, 26:1902–1909, 2017.

[61] A. Wilke, J. Orth, M. Lomb, R. Fuhrmann, H. Kienapfel, P. Griss, and R. P. Franke. Biocompatibility analysis of different biomaterials in human bone marrow cell cultures. *J Biomed Mater Res*, 40 (2):301–6, 1998. ISSN 0021-9304 (Print) 0021-9304.

[62] P. Wuisman, O. Lieshout, M. v. Dijk, and P. v. Diest. Reconstruction after total en bloc sacretomy for osteosarcoma using a custom-made prosthesis. *SPINE*, 26(4):431–439, 2001.

[63] J. Zang, W. Guo, Y. Yang, and L. Xie. Reconstruction of the hemipelvis with a modular prosthesis after resection of a primary malignant peri-acetabular tumour involving the sacroiliac joint. *Bone Joint J*, 96-b(3):399–405, 2014. ISSN 2049-4394. doi: 10.1302/0301-620x.96b3.32387.

[64] Y. Zhang, W. Guo, R. Yang, X. Tang, T. Yan, and T. Ji. Malignant pelvic tumors involving the sacrum: surgical approaches and procedure based on a new classification. *Orthopaedic Surgery*, 8:150–161, 2016.

[65] X. Zhao, J. Xiao, Y. Sun, Z. Zhu, M. Xu, and J. Wang, X. Wang. Novel 3d printed modular hemipelvic prosthesis for successful hemipelvic arthroplasty: a case study. *J Bionic Eng*, 15: 1067–1074, 2018.

[66] Y Zhao, S Zhang, T Sun, D Wang, W Lian, J Tan, and D Zou. Mechanical comparison between lengthened and short sacroiliac screws in sacral fracture fixation: a finite element analysis. *Orthopaedics & Traumatology: Surgery & Research*, 99(5):601–606, 2013.

A

Appendix

A.1. Appendix 1: Results additional FE models

A.1.1. Model 4: screw 1 and 5 inserted

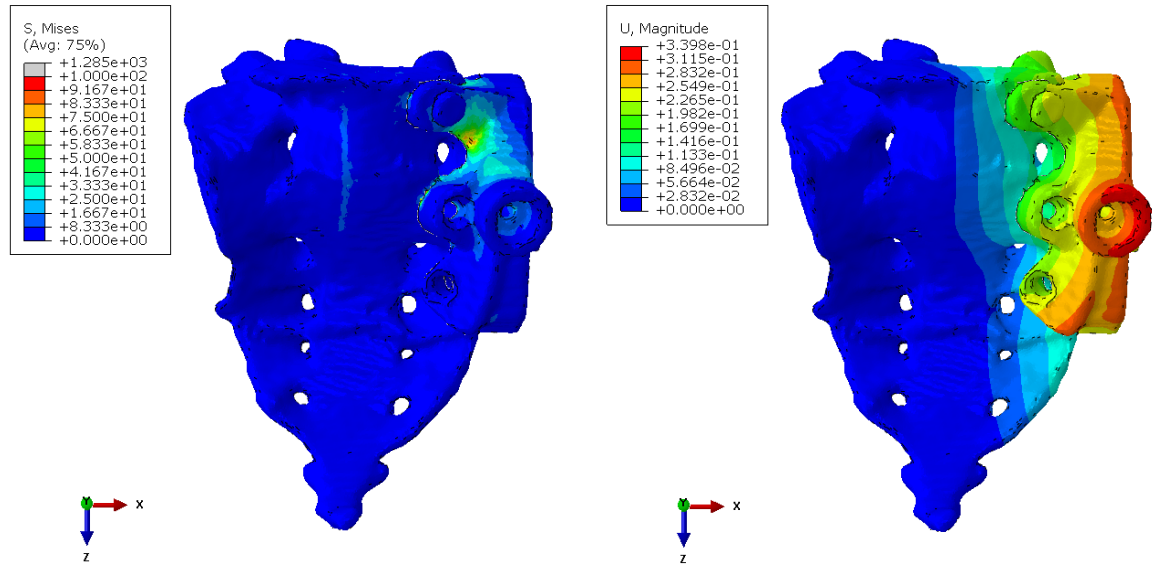

(a) Stress (N/mm^2)

(b) Deformation (mm)

Figure A.1: Stress and deformation of model 4 (screw 1 and 5 inserted).

Table A.1: Micromotions in x (U1), y (U2) and z(U3) direction and total micromotions (U) for model 5 with screw 1 and 5 inserted.

	U (μm)	**U1 (μm)**	**U2 (μm)**	**U3 (in μm)**
Flap 1	18.8674	8.7574	17.6172	23.6660
Flap 2	53.3845	29.1277	55.5259	36.6992
Flap 3	77.9494	54.6423	84.4530	6.6119
Back high	12.7133	1.9278	11.9626	10.4973
Back middle	20.6708	13.6653	31.8828	23.9967
Back low	138.2092	111.5134	92.7225	45.5299

A.1.2. Model 5: screw 3 and 4 inserted

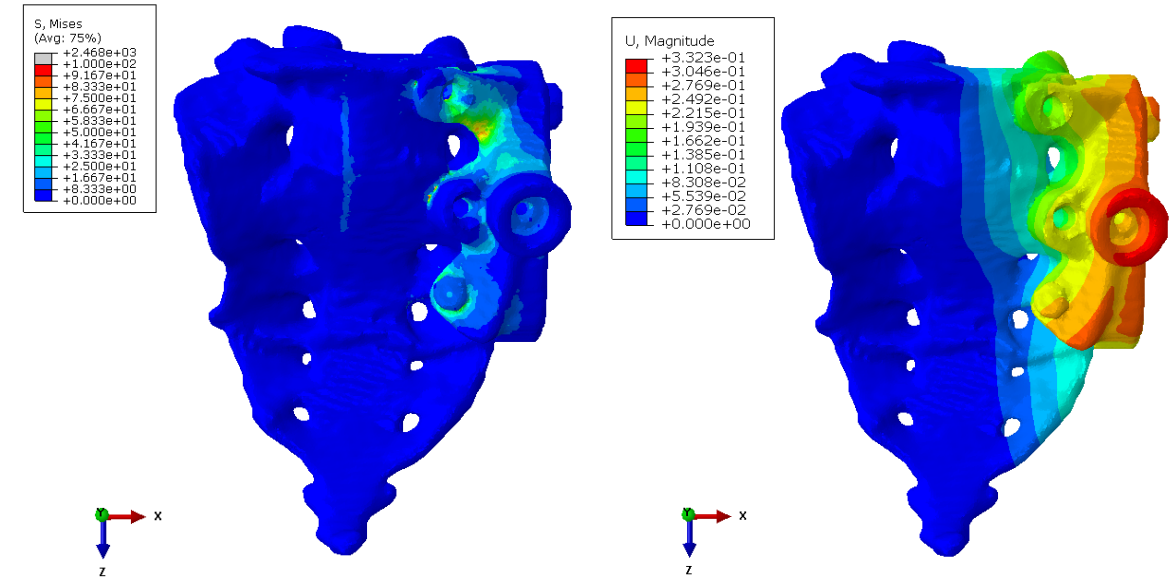

(a) Stress (N/mm^2)

(b) Deformation (mm)

Figure A.2: Stress and deformation of model 5 (screw 3 and 4 inserted)

Table A.2: Micromotions in x (U1), y (U2) and z(U3) direction and total micromotions (U) for model 5 with screw 3 and 4 inserted.

	U (μm)	**U1 (μm)**	**U2 (μm)**	**U3 (in μm)**
Flap 1	24.0076	12.9623	19.8284	28.9346
Flap 2	57.4745	27.8311	56.6429	42.8128
Flap 3	79.7177	56.2695	83.1656	6.0393
Back high	17.7128	2.7201	16.2831	13.7840
Back middle	23.3518	16.5520	42.4769	28.1728
Back low	131.2378	101.7557	87.6144	49.3889

A.2. Appendix 2: raw data experiments

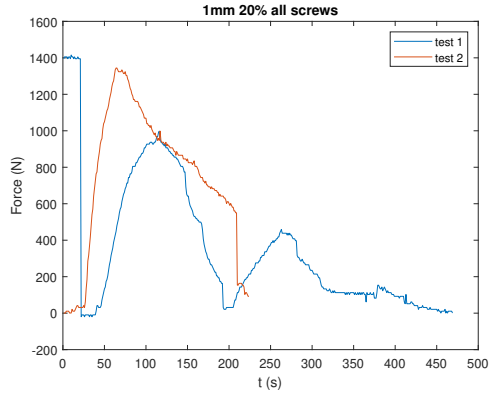

(a) Model 1mm 20% all screws.

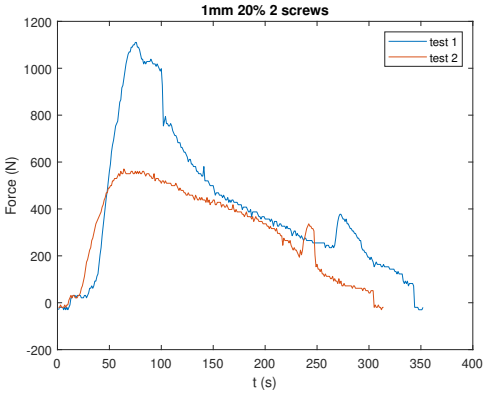

(b) Model 1 mm 20% 2 screws.

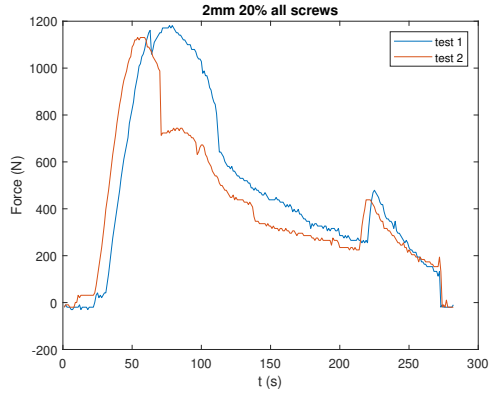

(c) Model 2 mm 20% all screws.

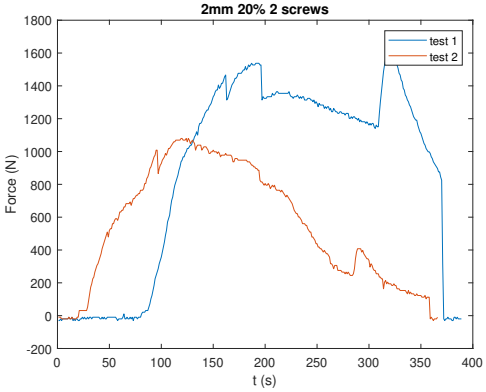

(d) Model 2 mm 20% 2 screws.

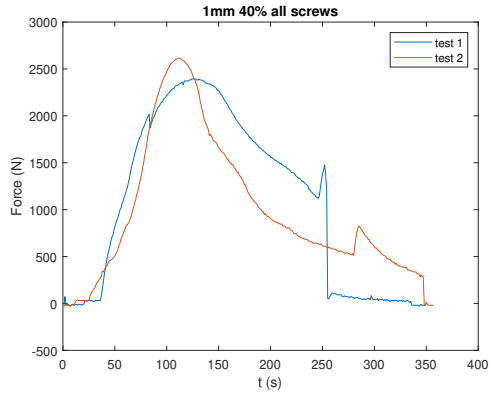

(e) Model 1 mm 40% all screws.

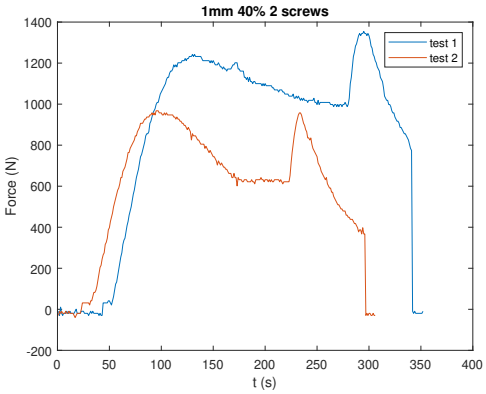

(f) Model 1 mm 40% 2 screws.

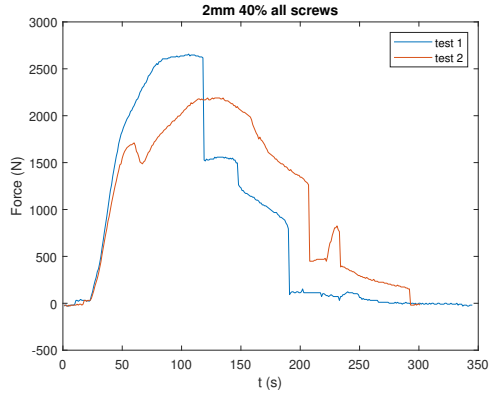

(g) Model 2 mm 40% all screws.

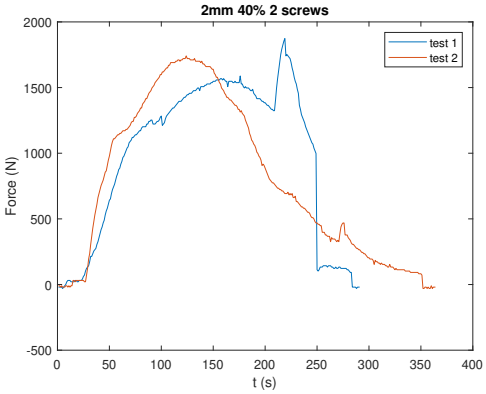

(h) Model 2 mm 40% 2 screws.

Figure A.3: Overview raw data all tests. For each model two samples were tested. This indicates a large variability between samples. Only in few models the results are similar. Further research with more samples is necessary.

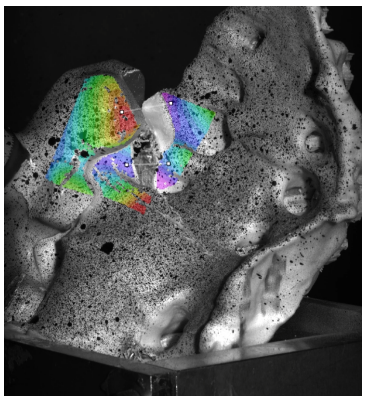

(a) Model 1mm 20% all screws camera 1.

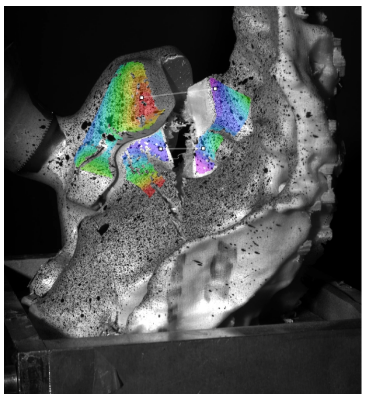

(b) Model 1 mm 20% all screws camera 2.

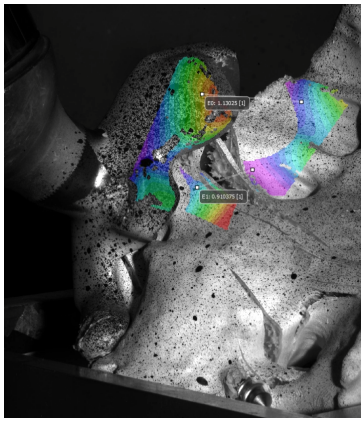

(c) Model 1 mm 20% 2 screws camera 1.

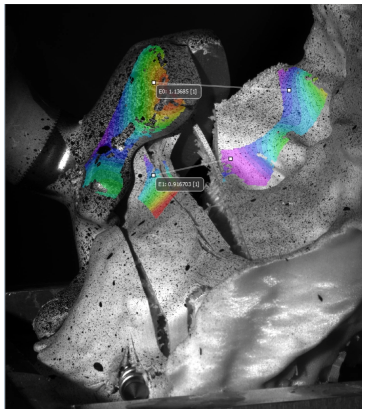

(d) Model 1 mm 20% 2 screws camera 2.

(e) Model 2 mm 20% all screws camera 1.

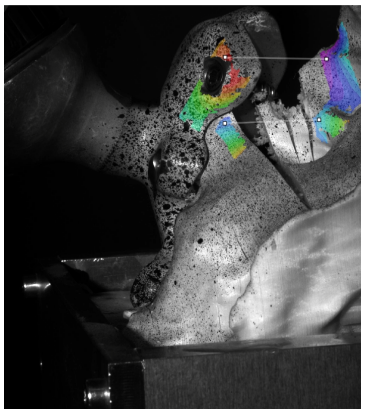

(f) Model 2 mm 20% all screws camera 2.

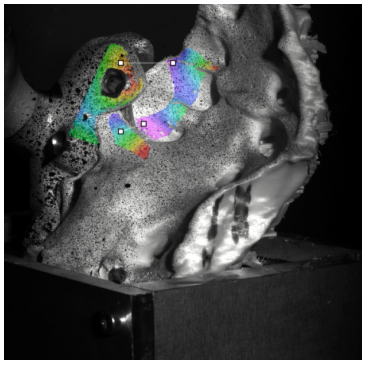

(g) Model 2 mm 20% 2 screws camera 1.

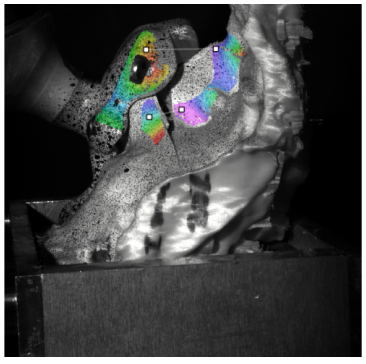

(h) Model 2 mm 40% 2 screws camera 2.

Figure A.4: Overview raw data all tests with models 1mm 20% and 2mm 20%.

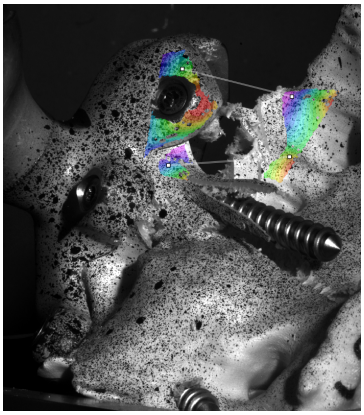

(a) Model 1mm 40% all screws camera 1.

(b) Model 1 mm 40% all screws camera 2.

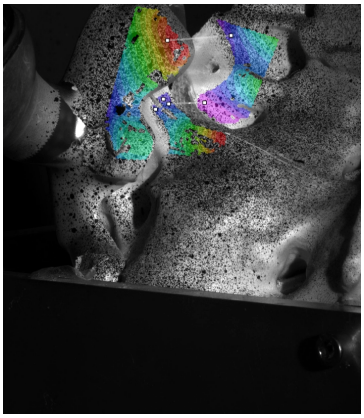

(c) Model 1 mm 40% 2 screws camera 1.

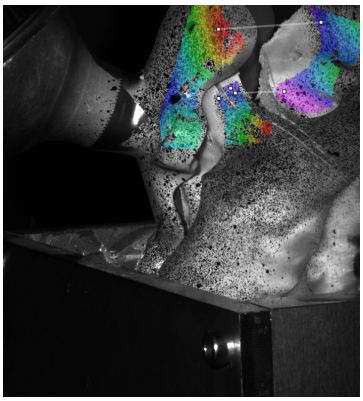

(d) Model 1 mm 40% 2 screws camera 2.

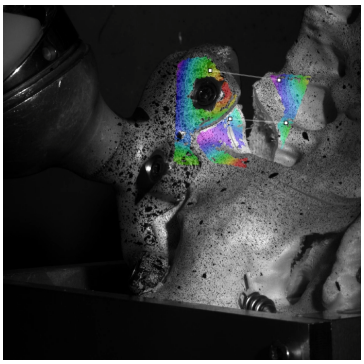

(e) Model 2 mm 40% all screws camera 1.

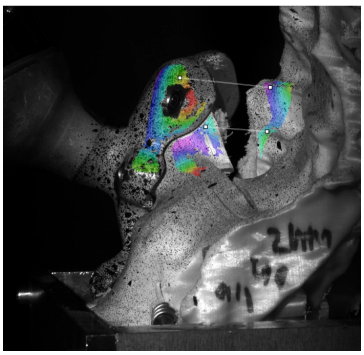

(f) Model 2 mm 40% all screws camera 2.

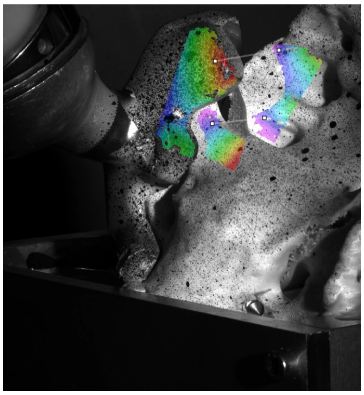

(g) Model 2 mm 40% 2 screws camera 1.

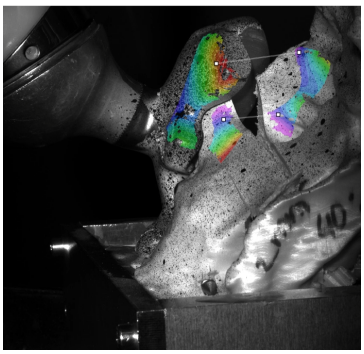

(h) Model 2 mm 40% 2 screws camera 2.

Figure A.5: Overview raw data all tests with models 1mm 40% and 2mm 40%.